

Rochester Institute of Technology

RIT Digital Institutional Repository

Theses

5-31-2010

Geometric Effects on the Wear of Microfabricated Silicon Journal Bearings

Shpend Demiri

Follow this and additional works at: <https://repository.rit.edu/theses>

Recommended Citation

Demiri, Shpend, "Geometric Effects on the Wear of Microfabricated Silicon Journal Bearings" (2010). Thesis. Rochester Institute of Technology. Accessed from

This Dissertation is brought to you for free and open access by the RIT Libraries. For more information, please contact repository@rit.edu.

**GEOMETRIC EFFECTS ON THE WEAR OF
MICROFABRICATED SILICON JOURNAL BEARINGS**

by

SHPEND DEMIRI

A DISSERTATION

Submitted in partial fulfillment of the requirements for the degree of

Doctor of Philosophy
in

Microsystems Engineering
at the

Rochester Institute of Technology

May 2010

Author _____
Microsystems Engineering

Certified by _____
Stephen Boedo, Ph.D.
Advisor

Approved by _____
Bruce W. Smith, Ph.D.
Director, Microsystems Engineering Program

Certified by _____
Harvey J. Palmer, Ph.D.
Dean, Kate Gleason College of Engineering

PËRKUSHTIM (DEDICATION)

Ju Dua!



**SHKENCA
DEMIRI**



**ENDON
DEMIRI**

Geometric Effects on the Wear of Microfabricated Silicon Journal Bearings

by

Shpend Demiri

Submitted by Shpend Demiri in partial fulfillment of the requirements for the degree of Doctor of Philosophy in Microsystems Engineering and accepted on behalf of the Rochester Institute of Technology by the dissertation committee.

We, the undersigned members of the Faculty of the Rochester Institute of Technology, certify that we have advised and/or supervised the candidate on the work described in this dissertation. We further certify that we have reviewed the dissertation manuscript and approve it in partial fulfillment of the requirements of the degree of Doctor of Philosophy in Microsystems Engineering.

Approved by:

Dr. Stephen Boedo
(Advisor)

_____ Date

Dr. Mustafa A.G. Abushagur

Dr. Hany Ghoneim

Dr. William J. Grande

Dr. Sean L. Rommel

Dr. Seth Hubbard

MICROSYSTEMS ENGINEERING
ROCHESTER INSTITUTE OF TECHNOLOGY
MAY 2010

ABSTRACT

Kate Gleason College of Engineering
Rochester Institute of Technology

Degree: Doctor of Philosophy **Program:** Microsystems Engineering

Candidate: Shpend Demiri

Title: Geometric Effects on the Wear of Microfabricated Silicon Journal Bearings

This dissertation presents an investigation of geometric effects on the wear of large aspect ratio silicon journal microbearings. The consideration of geometric conformality of rotor and hub as a critical design parameter manifests from the inherent properties of deep reactive ion etching as part of the current MEMS fabrication process employed in this dissertation. The investigation is conducted in two phases, each characterized by novel microbearing designs, fabrication processes, experimental test methodologies, and characterization techniques. The intent of Phase 1 is to focus on the effects of conformality of wear, while the intent of Phase 2 is to focus on the effects of clearance on wear. Manual assembly of rotors and hubs allows a broader range of custom bearing clearances than would otherwise be available from lithographic, pattern transfer, and etching capabilities of current in situ MEMS fabrication technologies. Novel wear indicators, intended to facilitate the rapid quantitative and qualitative determination of wear, are incorporated in the Phase 2 rotor designs. Two particular enabling features of the novel fabrication processes, namely the sprue and float etching methods, are developed in this dissertation. The sprues, patterned using the DRIE mask, hold the rotors in place during the KOH etching process. The float etching technique entails floating the device wafer on top of the KOH etchant bath. The results obtained from using the first apparatus indicate that microbearing performance, as measured by rotor rotational speed and rotor cumulative wear, is strongly dependent on conformality. The results obtained using the second apparatus indicate that microbearing rotor rotational velocity is strongly dependent on radial clearance parameter C_0 . A dynamic impact model of the bearing system based on classical impulse-momentum relations is formulated in order to assess the effect of clearance on rotor rotational speed. A coefficient of restitution is obtained for silicon-on-silicon surfaces over the range of kinematically allowable radial clearance specifications.

Advisor: Dr. Stephen Boedo

ACKNOWLEDGMENTS

Taking my first look back since embarking on this journey, I am fortunate to have made it without a contingency plan to speak of. WOW! I am grateful to all the people that made this achievement possible.

I would like to thank Dr. Stephen Boedo for his expertise, funding, and for help in arranging for fabrication to be performed at Cornell.

I thank Dr. William Grande and Dr. Sean Rommel for their fabrication insights and memorable conversations.

I am grateful to Professors Mustafa Abushagur and Hany Ghoneim for their academic, financial, and emotional support. Thank you for always keeping your doors open for me.

Last, but certainly not least, I am grateful to my wife Donika, daughter Shkenca, and son Endon for their love and patience.

This work was performed in part at the Cornell NanoScale Science and Technology Facility, a member of the National Nanotechnology Infrastructure Network, which is supported by the National Science Foundation (Grant ECS-0335765). This work was supported by grants through the Department of Energy, Office of Biological and Environmental Research (DE-FG02-02ER63393) and the National Science Foundation, Materials Design and Surface Engineering Program (CMMI-0409557).

CONTENTS

LIST OF FIGURES	8
LIST OF TABLES	15
NOMENCLATURE	16
1 INTRODUCTION	19
1.1 Motivation.....	20
1.2 Overview of Common Bearing Technologies	23
1.3 Review of Previous Research	27
1.4 Dissertation Goals and Objectives	33
1.5 Dissertation Outline	34
2 MICROBEARING SYSTEM DESIGN AND FABRICATION.....	35
2.1 Overview of MEMS-Based Fabrication Technologies.....	35
2.1.1 Thermal Oxidation	36
2.1.2 Photolithography.....	37
2.1.3 Deep Reactive Ion Etching	38
2.1.4 Potassium Hydroxide Etching.....	39
2.1.5 LIGA.....	40
2.2 Phase 1 Microbearing System.....	41
2.2.1 Phase 1 Rotor Fabrication.....	43
2.2.2 Phase 1 Hub Fabrication	53
2.3 Phase 2 Microbearing System.....	56
2.3.1 Phase 2 Rotor Fabrication.....	66
2.3.2 Phase 2 Hub Fabrication	74

3	EXPERIMENTAL TESTING	78
3.1	Phase 1 Testing	78
3.1.1	Phase 1 Test Setup	78
3.1.2	Phase 1 Test Procedure	83
3.1.3	Phase 1 Experimental Results.....	87
3.2	Phase 2 Testing	95
3.2.1	Phase 2 Test Setup	95
3.2.2	Phase 2 Test Procedure	99
3.2.3	Phase 2 Experimental Results.....	103
4	DISCUSSION.....	111
4.1	Bearing Load Assessment.....	111
4.2	Wear Rate Determination	120
4.3	Bearing Speed Simulation.....	128
5	CONCLUSIONS.....	142
5.1	Summary	142
5.2	Recommendations.....	145
A	FABRICATION PROCESSES.....	147
A.1	RCA Clean	147
A.2	BRUCE Furnace Oxidation Recipe #168	148
B	CAD DRAWINGS.....	151
B.1	Phase 2 Rotor CAD Drawings	151
B.2	Phase 2 Polycarbonate Plate CAD Drawing.....	156
B.3	Phase 2 Steel Top Plate CAD Drawing	157
	REFERENCES	158

LIST OF FIGURES

Figure 1:	Sandia microengine driving a micromirror (left) alongside and enlarged view of its microgear train (right).	21
Figure 2:	MIT micromotor-compressor rig (left) alongside a magnified view of its 4 mm diameter radial inflow turbine component (right).....	21
Figure 3:	Sandia microengine failure after 600,000 rotations. Boxed area from the image on the left is magnified on the right depicting wear particles. Note the severe wear in the gap.....	22
Figure 4:	Micrograph of crashed MIT silicon rotor (after only a few seconds of operation). Cleavage along the crystallographic planes of the 4 mm diameter rotor is clearly visible.....	22
Figure 5:	Common bearing categories; (a) Dry rubbing (i.e. journal rotating within sleeve), b) Rolling element, (c) Hydrodynamic, and (d) Hydrostatic.	24
Figure 6:	Operating regimes within EHL. The roughness scale is exaggerated.	26
Figure 7:	Pneumatically driven 5-axis milled (left) and EDM (right) turbine sub-assemblies employing conventional air and ball bearings, respectively.....	28
Figure 8:	3-D schematic of a rotary micromotor (left) alongside a corresponding radial cross-section (right) of the mechanical	

	and electrical components. It should be noted that the SiC coating required for operation is not depicted here.	29
Figure 9:	Bearing cross-sectional profiles. Rotor rotates about stationary hub.....	32
Figure 10:	Schematic depicts the oxidation of silicon.....	36
Figure 11:	Schematic of the photolithographic process.	37
Figure 12:	Schematic of DRIE sequence profile.....	38
Figure 13:	Schematic of KOH etch profile.....	39
Figure 14:	Representation of the LIGA process [].	40
Figure 15:	SEM micrograph of a manually assembled microbearing system (hub and rotor).	42
Figure 16:	Microbearing assembly schematic depicts single channel nitrogen gas flow in order to rotate the rotor.	42
Figure 17:	Phase 1 rotor fabrication sequence: (a) steps 1-6; (b) steps 7-12.	46
Figure 18:	Wafer after release of the rotors.....	48
Figure 19:	Magnified image of single rotor’s KOH etched pitted surface.	49
Figure 20:	Optical microscope image of sprues used to hold rotor in place during KOH etching.	50
Figure 21:	Schematic of the “float” etching technique depicts aerial and cross-sectional views of a wafer and Teflon O-ring circumferentially wrapped with Teflon tape.	51

Figure 22:	Diced Phase 1 hubs (pre-drilled (left) and post-drilled (right)).	55
Figure 23:	SEM micrograph of Phase 1 hub.	55
Figure 24:	Exploded view of Phase 2 microbearing design depicts hydrodynamic sectorial, step thrust bearing pads.	57
Figure 25:	Axial (left) and cross-sectional (right) views of a sectorial, step thrust bearing. The moving rotor shown in Section S-S is omitted in the axial view for clarity.	58
Figure 26:	Hub wafer design layout. Detail A depicts a single hub to which a rotor will be assembled to. Detail B (not shown) contains custom wafer alignment features. All dimensions are in μm unless otherwise denoted.	60
Figure 27:	Rotor mask design layout. All dimensions are in μm unless otherwise denoted.	62
Figure 28:	Process monitoring metrology blocks containing 1 μm minimum features.	62
Figure 29:	Phase 2 rotor geometries.	63
Figure 30:	Rotor schematic depicts novel <i>in situ</i> wear indicators.	65
Figure 31:	Phase 2 rotor fabrication sequence: (a) steps 1-6; (b) steps 7-12.	70
Figure 32:	Photograph of rotor wafer after DRIE.	72

Figure 33:	SEM micrograph depicts the geometry of a Phase 2 rotor after DRIE (left). Magnified image depicts an axial view of the rotor wear indicator features (right).....	73
Figure 34:	Phase 2 fabrication sequence for hubs with thrust pads: (a) steps 1-6; (b) steps 6-11.	75
Figure 35:	Photograph of Phase 2 hub wafer.	77
Figure 36:	Optical image of Phase 2 hub depicts thrust pads.....	77
Figure 37:	Photograph of Phase 1 experimental test setup.....	79
Figure 38:	Top view schematic depicting Phase 1 optical speed measurement methodology.	80
Figure 39:	Exploded-view of Phase 1 microbearing test fixture.....	82
Figure 40:	Photograph of Phase 1 microbearing test fixture. Connections on the tops and left are capped off.	82
Figure 41:	Conformal (top) and non-conformal (bottom) bearing configurations.	83
Figure 42:	Phase 1 optical microscope image sequences comparison for non-conformal test case NC1 (left column) and conformal test case C3 (right column).....	88
Figure 43:	Aluminum SEM fixture used to hold hubs and rotors.....	89
Figure 44:	Phase 1 SEM micrographs of non-conformal hubs and corresponding rotors	90
Figure 45:	Phase 1 SEM micrographs of conformal hubs and corresponding rotors.	91

Figure 46:	Wear morphology of rotor edge surface.	93
Figure 47:	Phase 1 rotor speed waveforms at 13.76 kPa (2 lb/in ²) supply pressure.....	94
Figure 48:	Photograph of Phase 2 experimental test setup.....	95
Figure 49:	Top view schematic depicting optical speed measurement methodology for Phase 2 microbearings.....	96
Figure 50:	Exploded-view of Phase 2 microbearing test fixture.....	98
Figure 51:	Photograph of Phase 2 microbearing test fixture.....	98
Figure 52:	Radial clearance C_0 defined for conformal (top) and non- conformal (bottom) bearing configurations with rotor at maximum axial displacement.	100
Figure 53:	Phase 2 optical microscope image sequences comparison for non-conformal bearing test cases NC4 (left column) and NC5 (right column).....	104
Figure 54:	Phase 2 optical microscope image sequences comparison for conformal bearing test cases C4 (left column) and C5 (right column).	105
Figure 55:	Phase 2 SEM micrographs of non-conformal hubs and corresponding rotors for test cases NC4 and NC5.....	106
Figure 56:	Phase 2 SEM micrographs of conformal hubs and corresponding rotors for test cases C4 and C5.....	107
Figure 57:	Phase 2 rotor speed waveforms at 68.80 kPa (10 lb/in ²) gas supply (gauge) pressure.	109

Figure 58:	Wear morphology of rotor edge surface.	110
Figure 59:	Phase 1 CFD model geometry (not to scale, dimensions in micrometers).	112
Figure 60:	Velocity magnitude and pressure distributions: Phase 1 test case C3 with 7981 RPM rotor speed and 13.76 kPa supply pressure.	114
Figure 61:	Phase 2 CFD model geometry (not to scale, dimensions in micrometers).	116
Figure 62:	Velocity magnitude and pressure distributions: Phase 2 test case NC4 with 9882 RPM rotor speed and 68.80 kPa supply pressure.....	118
Figure 63:	Phase 1 volumetric rotor wear assessment method: (a) regression fit of wear circle with diameter d_w ; (b) conical edge wear geometry.	121
Figure 64:	Phase 1 Comparison of measured and predicted volumetric wear due to adhesion.....	123
Figure 65:	Phase 2 volumetric rotor wear assessment method. Schematic depicts aerial (top) and cross-sectional (bottom) views of silicon wear debris accumulated on rotor's top surface.	124
Figure 66:	Phase 2 Comparison of measured and predicted volumetric wear due to adhesion.....	125

Figure 67:	Schematic of impact model geometry (not to scale) depicts relative kinematic parameters during impact at point p	129
Figure 68:	Variation of simulated average rotor rotational speed with β for Phase 1 case C3.....	137
Figure 69:	Variation of simulated average rotor rotational speed with β for Phase 1 case NC3.....	137
Figure 70:	Variation of simulated average rotor rotational speed with β for Phase 2 cases C4 and C5.....	140
Figure 71:	Variation of simulated average rotor rotational speed with β for Phase 2 cases NC4 and NC5.....	140
Figure 72:	Plot of β vs. C_0 obtained for each Phase 2 test case (NC4, NC5, C4, and C5).....	141

LIST OF TABLES

Table 1:	Bearing type strengths and weaknesses.	25
Table 2:	Phase 1 bearing specifications.	85
Table 3:	Phase 1 durability test procedure.	86
Table 4:	Phase 1 average rotational speeds (RPM) at specified supply pressures.	92
Table 5:	Phase 2 bearing specifications.	101
Table 6:	Phase 2 durability test procedure.	102
Table 7:	Phase 2 rotational speeds (RPM) at specified cumulative rotor cycles.	108
Table 8:	Phase 1 CFD model parameters.	115
Table 9:	Phase 2 CFD model parameters.	119
Table 10:	Model parameters for Phase 1 test cases NC3 and C3.	135
Table 11:	Simulated average rotor rotational speeds (RPM) for Phase 1 cases NC3 and C3.	136
Table 12:	Model parameters for Phase 2 test cases NC4, NC5, C4, and C5.	138
Table 13:	Simulated average rotor rotational speeds (RPM) for Phase 2 cases NC4, NC5, C4, and C5.	139

NOMENCLATURE

d	diameter	(m)
d_{max}	maximum rotor inner diameter	(m)
d_{min}	minimum rotor inner diameter	(m)
d_w	worn rotor diameter	(m)
d_0	unworn rotor diameter	(m)
e	rotor eccentricity	(m)
e_x	rotor eccentricity x -component	(m)
e_{xin}	rotor eccentricity x -component initial	(m)
e_y	y -component rotor eccentricity	(m)
e_{yin}	rotor eccentricity y -component initial	(m)
h_1	gas film thickness	(m)
h_2	gas film thickness over thrust pad	(m)
m	rotor mass	(kg)
r	rotor radius	(m)
r_1	rotor radius	(m)
t	time	(s)
t_w	wear particle thickness	(m)
v_x	velocity x -component	(m/s)
v_{xin}	velocity x -component initial	(m/s)
v_y	velocity y -component	(m/s)

v_{yin}	velocity y-component initial	(m/s)
x	x -coordinate axis	(m)
xc	x -coordinate axis contact frame	(m)
yc	y -coordinate axis contact frame	(m)
x	x -coordinate axis	(m)
z	z -coordinate axis	(m)
A_w	wear debris area	(m ²)
B	hub length	(m)
C	radial clearance	(m)
C_0	radial clearance	(m)
D	bearing diameter	(m)
F_r	radial force	(N)
F_t	tangential force	(N)
F_x	bearing load	(N)
J	mass moment of inertia	(kg-m ²)
K	adhesion wear coefficient	(-)
L	bearing length	(m)
L_s	length of the wear path	(m)
R	F_x moment arm	(m)
R_i	inner radius	(m)
R_o	outer radius	(m)
R_I	hub radius	(m)
V	rotor wear volume	(m ³)

V_{adh}	volumetric rotor wear (adhesion)	(m ³)
V_x	fin linear velocity	(m/s)
α	DRIE axial taper angle	(deg)
α_h	DRIE axial taper angle hub	(deg)
α_r	DRIE axial taper angle rotor	(deg)
β	coefficient of restitution	(-)
δ	rotor axial translation	(m)
η	dynamic coefficient of viscosity	(Pa-s)
θ_1	sectorial boundary angle	(rad)
θ_2	thrust pad sectorial boundary angle	(rad)
μ	dynamic coefficient of friction	(-)
σ_y	yield stress	(Pa)
ω	angular frequency	(rad/sec)
ω_{in}	angular frequency initial	(rad/sec)

1 INTRODUCTION

In the past half century, new uses of silicon were brought to light ushering in the Integrated Circuit (IC) revolution. Advancements in IC processing, during the past couple of decades, led to the introduction of silicon-based MicroElectroMechanical Systems (MEMS). Silicon's prominence within MEMS is attributed to its strength, electrical and oxidation characteristics [1].

Microsystems comprise small components with sub-millimeter critical dimensional parameters which can sense or manipulate their environment (matter or energy). A key incentive fueling the development of microsystems is the low unit cost resulting from mass-fabrication of complex, integrated, silicon-based components by borrowing many established precision IC processing techniques. Of equal significance are the fast response, low weight, and low power consumption characteristics intrinsic to microsystems. Examples of microsystems that have been commercialized over the past decades include inkjet printer components, pressure sensors, accelerometers, optical switches and microfluidic lab-on-chip devices.

On the macroscale, some of the most important systems are those consisting of component surfaces that operate in close relative motion to each other, such as rotating machinery. Examples include turbines, engines, pumps, and compressors that are ubiquitous in power generation, transportation, heating, ventilation, and air conditioning.

Researchers, such as Feynman [2], Kovacs [3] and Madou [4], have inspired efforts to develop micro-sized embodiments of such macrosystems. Possible applications employing microbearings (the integral components of rotating micromachinery) involve microturbines for Power-MEMS [5] (propulsion and distributed, portable power generation), micropumps for labs-on-chips [6] (chemical testing, micromixing, fluidic metering, biomedical engineering, heating and cooling), microengines for optics [7] (optical encoding), and microgears [8] for transmission or actuation (mechanical arming systems and micromirror adjustments).

1.1 Motivation

In response to increasing demand for mobility and multifunctionality at low cost, the range of MEMS applications has been rapidly expanding. Ambitious projects such as the Sandia National Laboratories (SNL) microengine [9] (Figure 1) and Massachusetts Institute of Technology (MIT) Power-MEMS microturbine [10, 11] (Figure 2) have been undertaken over the past two decades. The results of such endeavors are expected to revolutionize sensing and actuation in biomedical, transportation, military, industrial, environmental, industrial technology and recreational activities.

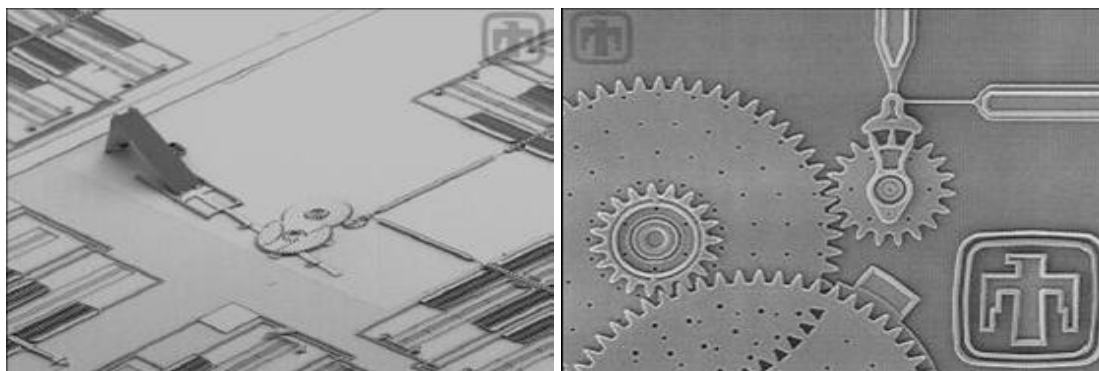


Figure 1: Sandia microengine driving a micromirror (left) alongside and enlarged view of its microgear train (right).

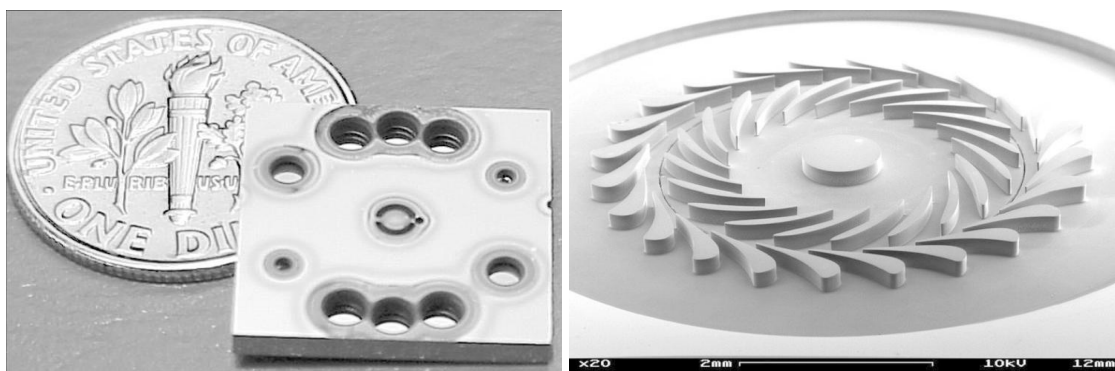


Figure 2: MIT micromotor-compressor rig (left) alongside a magnified view of its 4 mm diameter radial inflow turbine component (right).

In the quest to commercialize microsystems associated with rotating machinery, the primary inhibitor to date has been bearing reliability. This is particularly true for high speed operation (on the order of tens of thousands to millions of revolutions per minute

(RPM)) where seizure, high wear rates (Figure 3) [12], and complete destruction (Figure 4) [13] have been observed.

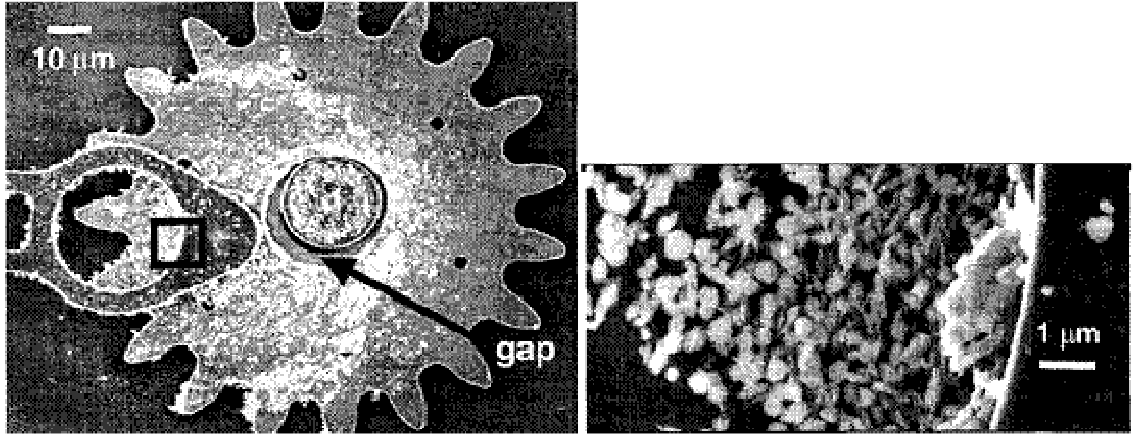


Figure 3: Sandia microengine failure after 600,000 rotations. Boxed area from the image on the left is magnified on the right depicting wear particles. Note the severe wear in the gap.

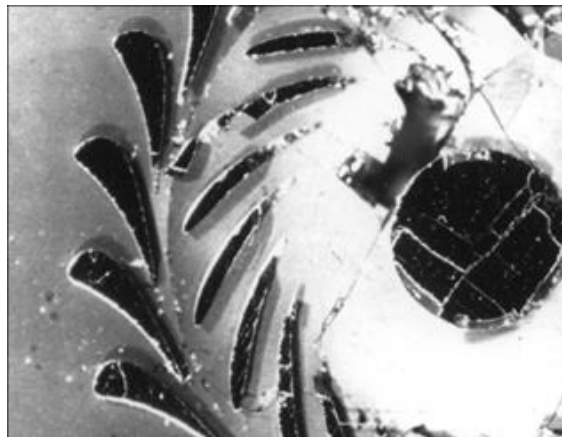


Figure 4: Micrograph of crashed MIT silicon rotor (after only a few seconds of operation). Cleavage along the crystallographic planes of the 4 mm diameter rotor is clearly visible.

In order for any system, regardless of size, to come to fruition, there must be a fundamental understanding of its individual components and the interactions involved between them and the surrounding environment. A fundamental discipline concerning systems involving rotating machinery is known as tribology. Tribology - the study of wear, lubrication, and friction of interacting surfaces in relative motion - becomes increasingly important as systems scale down due to an increased surface to mass ratio [14]. In this regime, rapid bearing wear has indeed proven to be a formidable factor to overcome and relatively little is known about its characteristics. This challenge along with the immense potential for rotary microsystems to change our lives, serve to motivate this investigation of geometric effects on the wear of silicon journal microbearings.

1.2 Overview of Common Bearing Technologies

This section presents a brief overview of bearing operational principles to familiarize the reader with the terminology and concepts contained in the subsequent literature review.

Bearings can generally be classified as dry rubbing, rolling element, hydrodynamic, and hydrostatic, as shown in Figure 5. Dry rubbing bearings consist of two component surfaces, conventionally made from polymer- or carbon-based materials (e.g. nylon, polytetrafluoroethylene (PTFE), or graphite) rubbing against each other in rolling or sliding motion. Rolling element bearings are characterized by the rolling motion of spherical, cylindrical or conical components (typically metal-based) between

surfaces. Hydrodynamic bearings are characterized by a pressurized wedge of gas or liquid film that develops as surfaces move at a slight incline to each other. Hydrostatic bearings maintain a gas or liquid film by a continuous supply of external pressure between non-moving surfaces.

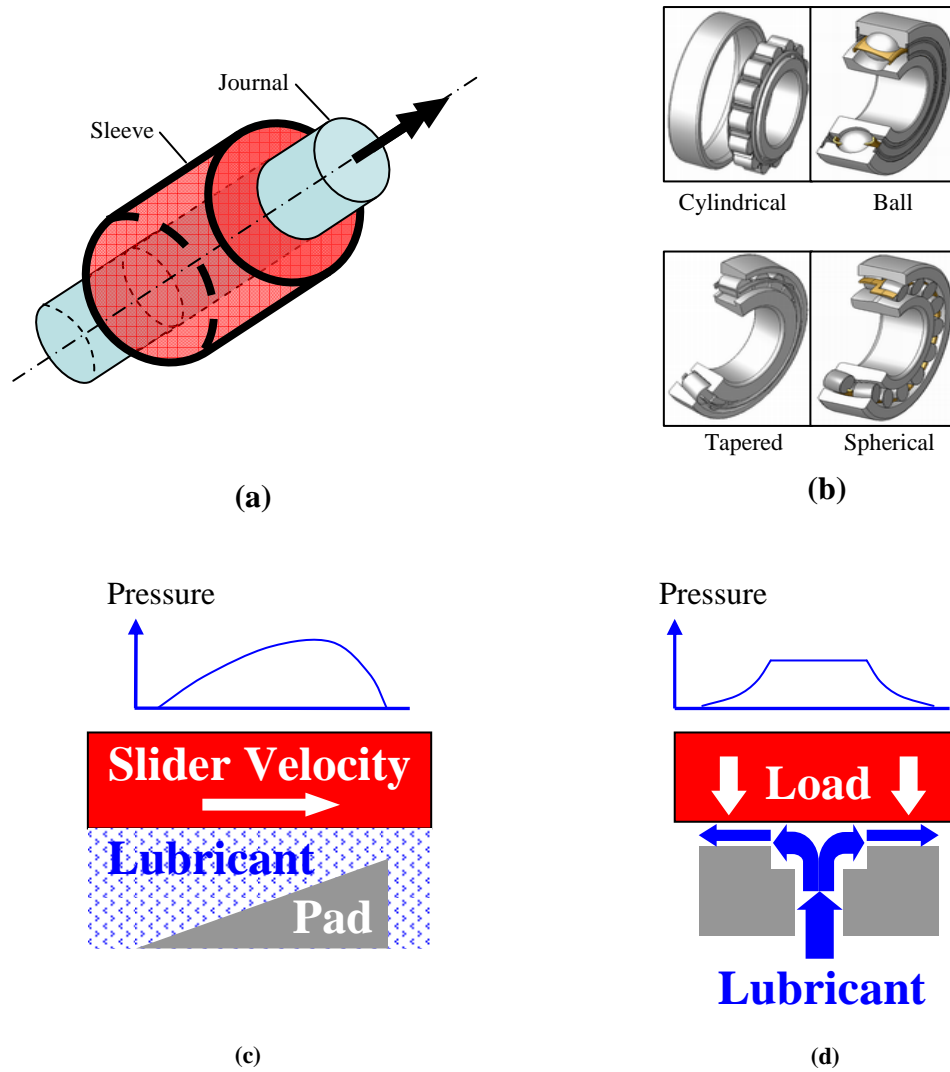


Figure 5: Common bearing categories; (a) Dry rubbing (i.e. journal rotating within sleeve), (b) Rolling element, (c) Hydrodynamic, and (d) Hydrostatic.

The strengths and weaknesses of common bearing technologies are shown in Table 1. It is evident from this comparison that gas bearings are the most attractive alternative for development of micromachinery.

Table 1: Bearing type strengths and weaknesses.

Bearing	Strengths	Weaknesses
Dry rubbing	<ul style="list-style-type: none"> Manufacturability High Load Capacity Contamination avoidance 	<ul style="list-style-type: none"> High friction High wear Low speed Lowest temperature range
Rolling element	<ul style="list-style-type: none"> Good stability High load capacity Wide temperature range 	<ul style="list-style-type: none"> Require cooling Oil/grease lubrication Largest form factor Assembly Manufacturability MEMS fabrication incompatibility
Liquid	<ul style="list-style-type: none"> Compact Lower friction than rolling element bearings 	<ul style="list-style-type: none"> Higher friction than gas bearings Require periodic liquid change Likelihood of contamination
Gas	<ul style="list-style-type: none"> Can use working fluid Contamination avoidance High speed operation Lowest friction Lowest heat generation Manufacturability Minimal wear Most Compact Quiet Widest temperature range 	<ul style="list-style-type: none"> Poor stability Small load capacity

For bearings operating in hydrostatic or hydrodynamic modes, friction, adhesion, stiction (static-friction), stability and thereby wear are influenced by the relative motion of component surfaces through intermediate lubricant films. As loads are transmitted between these bearing surfaces, the film is wedged or squeezed between the surfaces in motion creating a film pressure which tends to separate the surfaces. This film pressure

can in turn induce deformation of the interacting surfaces. The interaction between this film and structural deformation is known as elastohydrodynamic lubrication (EHL). Figure 6 depicts the three regimes within EHL. It should be noted that the bearing surface roughness scale in this figure is exaggerated for clarity.

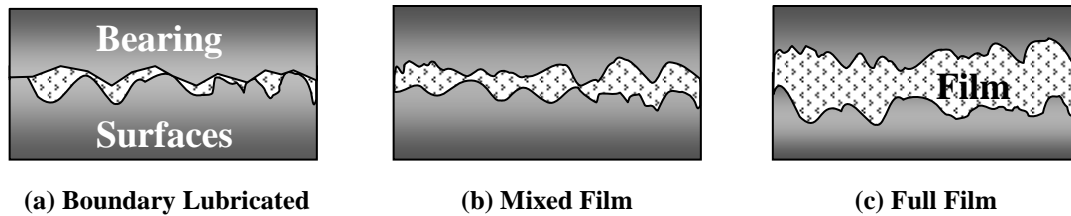


Figure 6: Operating regimes within EHL. The roughness scale is exaggerated.

Under EHL conditions, bearings are considered to be operating in a boundary lubricated regime if the film thickness is on the order of the surface roughness (Figure 6a). In this regime it is the surface asperities, not the lubricant film, that bear the brunt of the applied load. Therefore, in order to mitigate wear or the possibility of seizure, reliance has historically been placed primarily on surface treatments (coatings). In contrast, when the bearing film thickness is roughly greater than three times the surface roughness (Figure 6c), the load is carried by an essentially full lubricant film and the potential for wear is reduced significantly. On the macroscale, most fluid bearings operate in a mixed to full-film regime, and the asperities which influence long term wear carry only a small percentage of the applied load compared with that carried by the lubricant film.

Wear results from a conglomeration of complex parameter interactions including bearing load, pressure, surface temperature, operational speed, material properties, surface roughness, component geometry, and environmental factors such as humidity and cleanliness. It is reasonable to assume therefore, that gas microbearings would be ideal candidates for applications requiring minimal wear and maintenance.

The optimization of gas microbearings will entail the support of acceleration, gas, gravity, and fabrication related imbalance forces. Directionally, all of these forces, acting on the rotor, will contribute to axial and/or radial bearing load design requirements. Satisfying these requirements remains a challenge. In attempting to do so, thrust and journal bearings are generally designed to support axial and radial loads, respectively.

1.3 Review of Previous Research

Ever since the first papers on lubrication experimentation (Beauchamp Tower, 1883) and theory (Osborne Reynolds, 1886) were published, the determination of journal bearing performance and thereby wear characteristics under any conceivable geometric variation has proven to be extremely difficult.

In the past decade, metal-based, pneumatically driven, miniature turbine prototypes manufactured using traditional 5-axis milling [15] and Electric Discharge Machining (EDM) [16] techniques have been reported (Figure 7). Intended for power generation, these prototypes employ conventional air and ball bearings, respectively. Wear characteristics of these meso-scaled (~ 0.5-1.0 cm in diameter) bearings were not

reported. Associated low power densities, large size, and high unit costs, however, render these designs commercially unattractive.

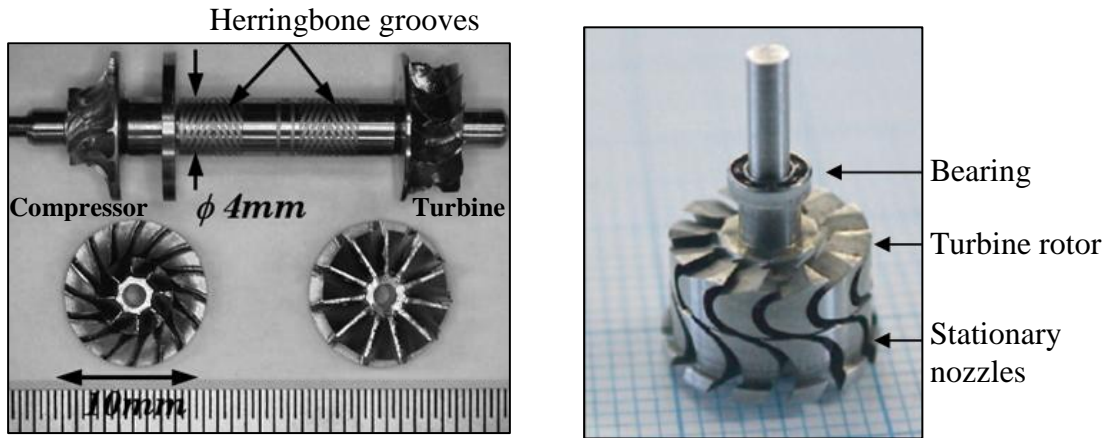


Figure 7: Pneumatically driven 5-axis milled (left) and EDM (right) turbine sub-assemblies employing conventional air and ball bearings, respectively.

More recently, the first rotary micromotor employing steel micro-ball bearings has been reported [17] (Figure 8). One of the key issues with this machine was that its 14 mm diameter, manually aligned, silicon-based rotor would not rotate without the deposition of a silicon carbide (SiC) coating. While this variable-capacitance micromotor briefly attained (upon being coated) a maximum rotation rate of 517 RPM, operation for any extended period of time (greater than a few seconds) was precluded by collisions and jamming between of the 10 manually assembled steel micro-ball bearings, each $\sim 285 \mu\text{m}$ in diameter. Upon applying a minimum of 150 V, operation on the order of a few hours was possible at a low rotation rate of 17 RPM. Based on these considerations, the inherent complexities associated with the application of rolling element bearing technologies appear to be exacerbated at the micro-scale.

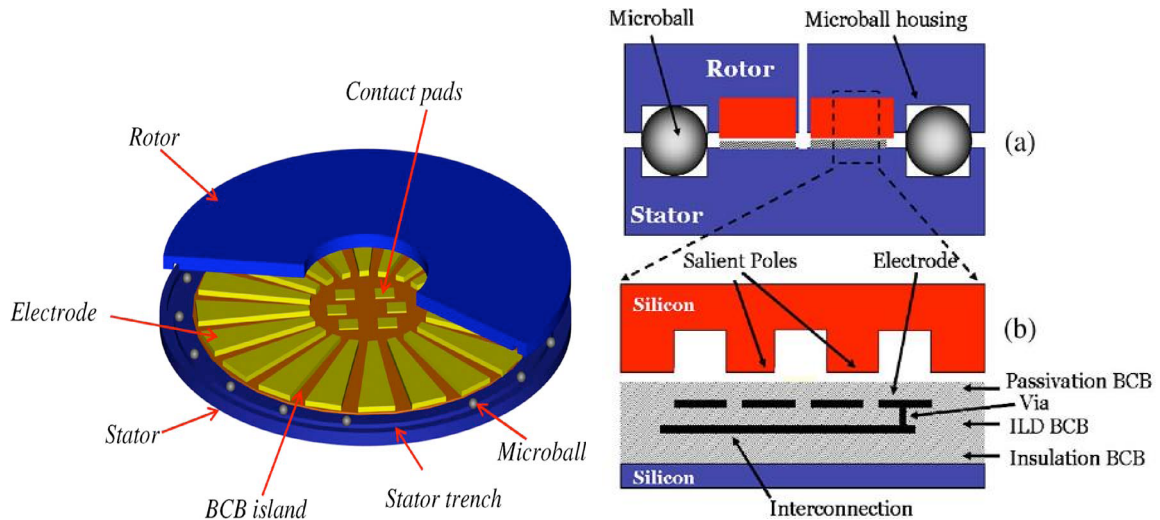


Figure 8: 3-D schematic of a rotary micromotor (left) alongside a corresponding radial cross-section (right) of the mechanical and electrical components. It should be noted that the SiC coating required for operation is not depicted here.

Henceforth this literature review focuses predominantly on journal bearings that have been fabricated using lithographic- or MEMS-based technologies since they offer optimal form factor (small size and a minimal number of bearing components) and the possibility of mass fabrication at low unit cost. Further, particular attention is devoted to silicon-based journal microbearings since they are most compatible with conventional IC as well as more contemporary MEMS processing technologies.

Silicon-based rotating micromachine elements, such as gears and pin joints, were introduced as early as 1987 [18], followed by the introduction of the first surface micromachined electrostatic motor in 1988 operating at 500 RPM [19]. The demonstration of an air-driven turbine measuring 40 μm thick and 900 μm in diameter, operating at 24,000 RPM followed in the same year [20]. Since then, researchers have worked primarily on surface micromachined polysilicon electric-driven rotating

machinery [21, 22, and 23]. The design space available for employing this fabrication methodology has resulted in bearings with length-to-diameter (L/D) or slenderness ratios on the order of approximately 0.05. This ultra small L/D ratio results from limitations of the surface micromachining planar fabrication technology [24]. It is generally agreed upon that the inability of these ultra low aspect ratio bearings to maintain sufficient hydrodynamic lubrication between the post and the rotor is what causes rapid wear/seizure to occur [25]. It is not entirely surprising therefore, that wear mitigation via bearing surface treatment has been the primary area of focus [26], as silicon is generally thought to be a poor tribological material [27, 28]. Unfortunately, surface treatments alone have failed to markedly improve rotating micromachinery wear behavior.

In addition to surface micromachining technologies, researchers have used bulk micromachining [29] technologies such as deep reactive ion etching (DRIE) for microengines [30]. Though still considered a planar fabrication technology, bulk micromachining enables larger aspect ratio structures.

To date, analytical and experimental investigations of both surface and bulk microfabricated bearings have focused primarily on plain cylindrical geometries and rigid bearing components.

The hydrodynamic performances of gas lubricated stepped and plain cylindrical journal microbearings (L=500 μm ; D=500 μm) were predicted in 2004 [31]. For a given eccentricity, the load carrying capacity of the plain cylindrical journal bearing was calculated to be significantly greater than the gas lubricated stepped bearing.

Wear characteristics of similarly large aspect ratio (~ 0.6), plain cylindrical journal bearings with and without tungsten alloy coatings, fabricated using X-ray lithography and Ni electroplating were reported in 2005 [32]. Results indicated that coated microbearings had lower wear rates than uncoated bearings.

While experimental investigations of wave/lobed (non-cylindrical) [33] journal microbearing designs have not been reported, similar load bearing capacity enhancements using lobed microbearings for high speed applications have been predicted [34, 35].

Macroscale foil bearings used in high speed applications (i.e. aerospace) offer enhanced stability and accommodate vibration suppression, elastic and thermal distortions [36]. Currently, there is no published literature on microscale foil bearing development. Motivated by the foil bearing compliance characteristics, a numerical analysis of novel flexible, large-aspect ratio, high-speed journal microbearing designs was recently claimed to improve load capacity and enhance stability [37].

An experimental investigation of the influence of taper on gas macrobearing (rotating tapered shaft within a plain cylindrical bearing) performance was conducted in 1966 [38]. It was determined that the cocking (misalignment) of the shaft would increase due to either increased shaft taper or increased bearing clearance. It was also observed that the half frequency whirl, threshold speed of the tapered shaft was approximately the same as that of an unmodified shaft. It should be noted that the test shaft and bearing lengths were approximately 2.5 and 1.125 inches, respectively while the L/D ratio was approximately 1.0. More recently a numerical study was conducted on axially varying microbearing clearance [39], a signature characteristic of the DRIE process. It was determined that tapered and bowed bearing clearance profiles were detrimental to bearing

load capacities when compared to plain bearing clearances. A schematic illustrating these three bearing profiles is shown in Figure 9. Taper was claimed to be more detrimental than bow. Results also indicated that a lower minimum load was required for stability in the axially varying case.

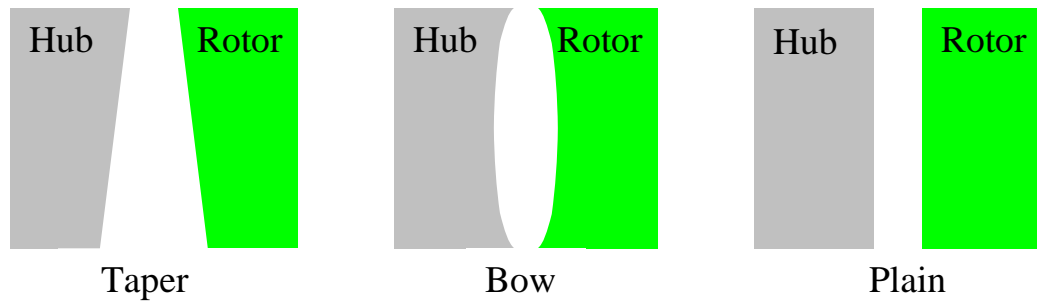


Figure 9: Bearing cross-sectional profiles. Rotor rotates about stationary hub.

1.4 Dissertation Goals and Objectives

To date, relatively little is understood about the wear behavior of large aspect ratio microbearings. The main goals of this dissertation are to investigate the effects of conformality and clearance on wear of microfabricated journal bearings. In addition, the work herein establishes a foundation for future microbearing designs and associated performance characterization techniques.

The specific objectives of this work are to

- design and fabricate large aspect ratio silicon journal microbearings
- develop experimental apparatus necessary to test them
- develop methodologies to measure or characterize
 - load
 - rotor rotational speed
 - clearance
 - wear

By obtaining a more thorough understanding of how these parameters influence bearing reliability, this fundamental hindrance to the development of many MEMS applications can be substantially mitigated.

1.5 Dissertation Outline

Chapter 2 presents microbearing design and fabrication aspects of this work including the technologies and procedures used. Challenges faced and lessons learned from both successful fabrication techniques as well as unsuccessful attempts are also documented.

Chapter 3 covers the experimental test methodology associated with the microbearings. Included here are metrology and wear characterization techniques as well as experimental apparatus development.

A discussion of the experimental test results is contained in Chapter 4. Included here are modeling simulations.

Chapter 5 will conclude with the summary and contributions of this work followed by fabrication and test lessons learned, and recommendations for future research and development.

2 MICROBEARING SYSTEM DESIGN AND FABRICATION

This chapter will discuss microbearing system design and fabrication considerations, including technologies and procedures used to develop the rotor and hub microbearing components. The work herein was conducted in two sequential phases: Phase 1 initiated by researchers at the Rochester Institute of Technology (RIT) [40, 41] and Phase 2 differentiated by design parameters and fabrication processes. Challenges faced and lessons learned from successful fabrication techniques as well as unsuccessful attempts are documented throughout. Detailed fabrication recipes are presented in the appendix.

2.1 Overview of MEMS-Based Fabrication Technologies

This section contains an overview of relevant MEMS-based fabrication technologies. For comparison, a brief contextual overview of LIGA (a competing microfabrication technology not used for this work), is presented at the end of this section.

2.1.1 Thermal Oxidation

Silicon dioxide (SiO_2) can be used as a mask during etch processes. The thermal oxidation of silicon is typically accomplished in an atmosphere containing oxygen (dry oxidation) or water vapor (wet oxidation) at elevated temperatures typically ranging from 900 to 1000 °C. Wet oxidation is characterized by a higher growth rate than dry oxidation and is preferred when growing a thick oxide. On the other hand, dry oxidation yields a higher-density oxide. An elevated temperature is required in order to enhance oxygen's diffusion rate through the growing SiO_2 layer.

The oxide layer depicted in Figure 10 grows thicker as silicon is consumed from the Si- SiO_2 interface. The amount of the silicon consumed is 44 percent of total thickness of the oxide grown.

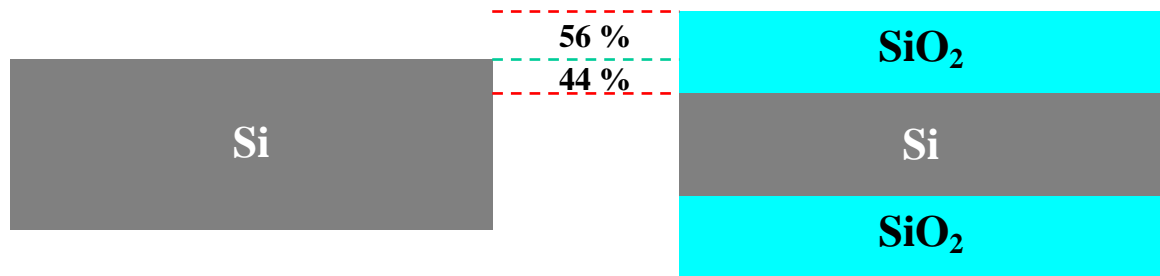


Figure 10: Schematic depicts the oxidation of silicon.

2.1.2 Photolithography

Photolithography is used to transfer patterned device designs onto substrate wafers (Figure 11). During the photolithographic process wafers are coated with a polymer (photoresist) that is sensitive to light. Once the desired regions of the coated wafers are exposed to light through patterned masks, the exposed polymer (in the case of positive photoresist) becomes soluble and can be removed using developer. In contrast, if negative photoresist is used, its polymer chains are cross-linked by the light, rendering the exposed areas insoluble. In either case, the remaining resist then serves to protect the silicon wafer from future etching or material deposition.

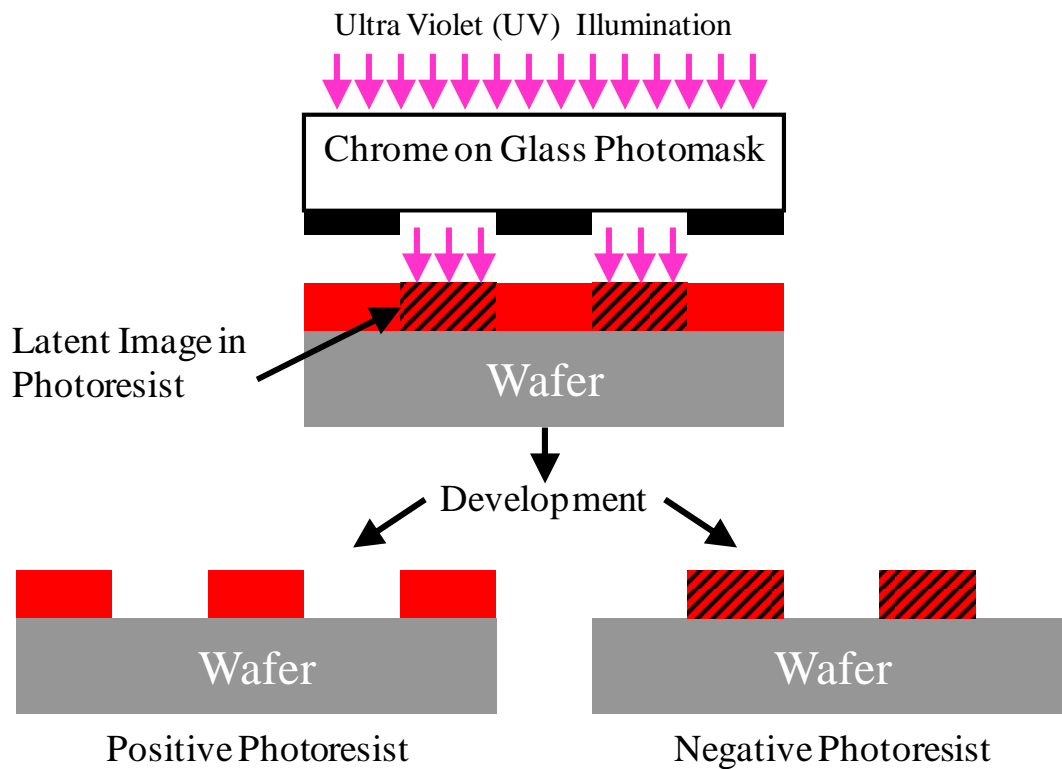


Figure 11: Schematic of the photolithographic process.

2.1.3 Deep Reactive Ion Etching

DRIE can be categorized as an anisotropic bulk micromachining technology and can be used to etch features completely through silicon wafers (typically 500 - 600 μm thick). The DRIE technique (Figure 12), invented by Bosch [42], is characterized by the cyclic repetition of an isotropic etch step using sulfur hexafluoride (SF_6) followed by a passivation step which deposits a Teflon-like layer using octafluorocyclobutane (C_4F_8). The purpose of the passivation layer is to protect the sidewalls from the next iteration of isotropic etching. Nearly vertical walls can be obtained using this technique.

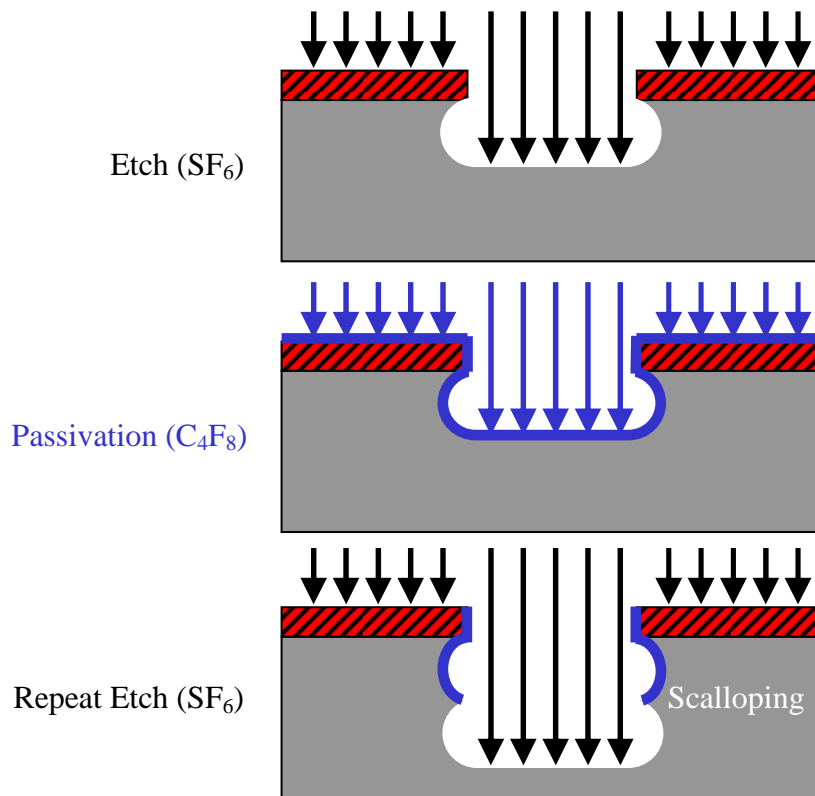


Figure 12: Schematic of DRIE sequence profile

2.1.4 Potassium Hydroxide Etching

Potassium hydroxide (KOH) etching is another bulk micromachining technology that can be used to etch non-cylindrical features completely through silicon wafers. KOH, however, is a wet etchant and is selective as it etches, nearly stopping upon encountering silicon {111} crystal planes (Figure 13). This planar dependency limits through-wafer feature aspect ratios. The KOH etch process is generally carried out at an elevated temperature in order to increase the etch rate of silicon.



Figure 13: Schematic of KOH etch profile.

2.1.5 LIGA

While not used here, LIGA (*lithographie, galvanofornung, und abformung*) is a competing process for fabricating high aspect ratio microstructures (Figure 14). In the first step, high energy X-rays generated by a synchrotron are used to expose an X-ray sensitive resist such as polymethylmethacrylate (PMMA) through a mask. Once a pattern in the resist is developed, metallic microstructures and/or micro-molds are electroformed. In the next step, secondary microstructures made from polymers, metals or ceramics can be molded using the electroplated metallic micro-molds. These secondary microstructures can now be utilized in a secondary electroforming process step to make additional metallic molds. Though relatively straight walls are attainable, one of the challenges in using LIGA is shrinkage during the PMMA polymerization process leading to strain in the resist layer. The major prohibitive consideration is the requirement of a synchrotron.

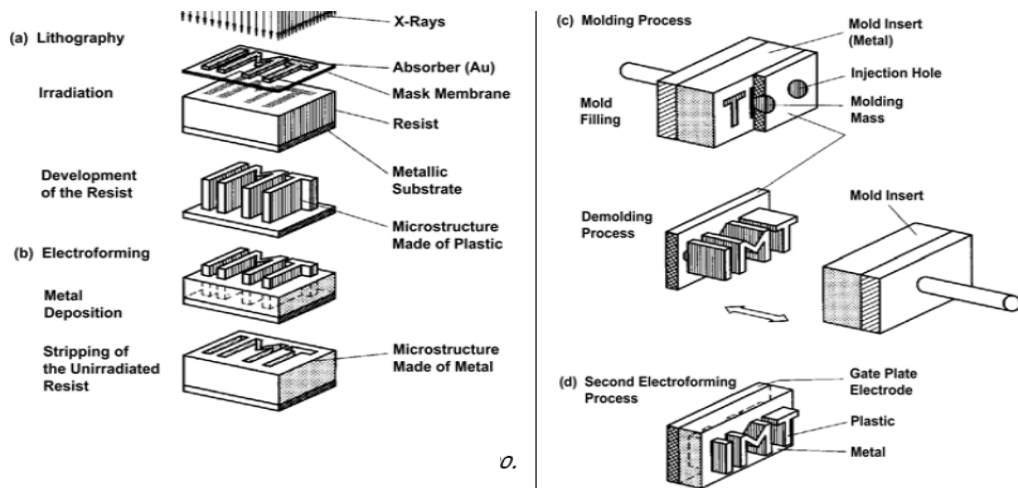


Figure 14: Representation of the LIGA process [43].

2.2 Phase 1 Microbearing System

Figure 15 depicts an SEM micrograph of a rotor that has been manually assembled to a stationary hub to form the microbearing system. The rotor is pneumatically driven by nitrogen gas (Figure 16) which enters a drilled access hole from the backside of the hub and flows through one of the rectangular microchannels.

The rotor bearing length and diameter for this phase are approximately 165 μm and 400 μm , respectively, resulting in an L/D ratio of approximately 0.4. The rotors and hubs used in this phase are created on separate silicon wafers. They are subsequently assembled manually to form the microbearing systems. One of the benefits of manual assembly is that rotors and hubs can be mixed and matched to obtain a broad range of custom radial bearing clearances and configurations. Achieving radial bearing clearances on the order of 1-10 μm (the range of interest for the work herein) by means of *in situ* fabrication of rotors and hubs is not feasible using current MEMS fabrication technologies.

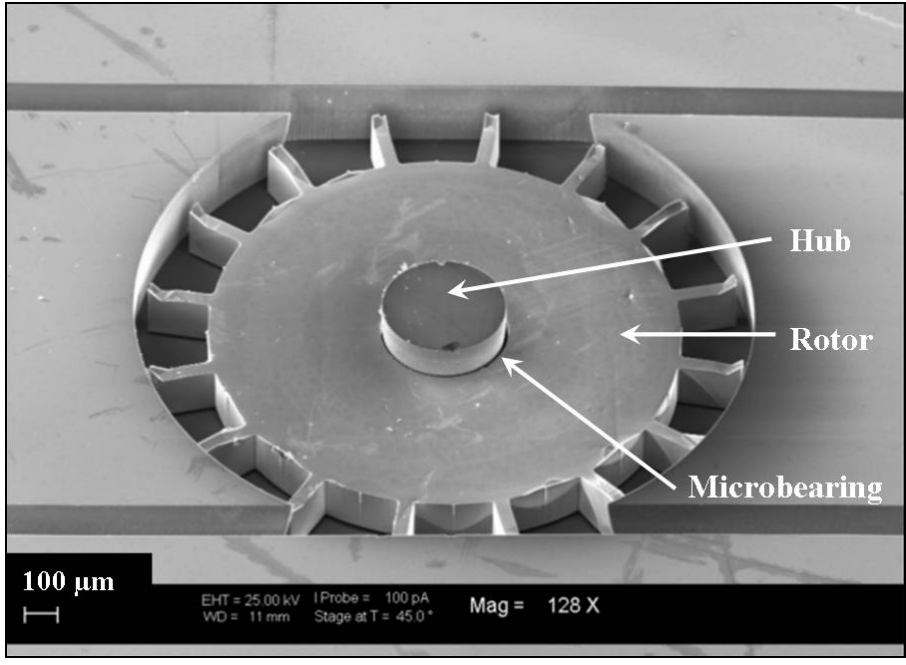


Figure 15: SEM micrograph of a manually assembled microbearing system (hub and rotor).

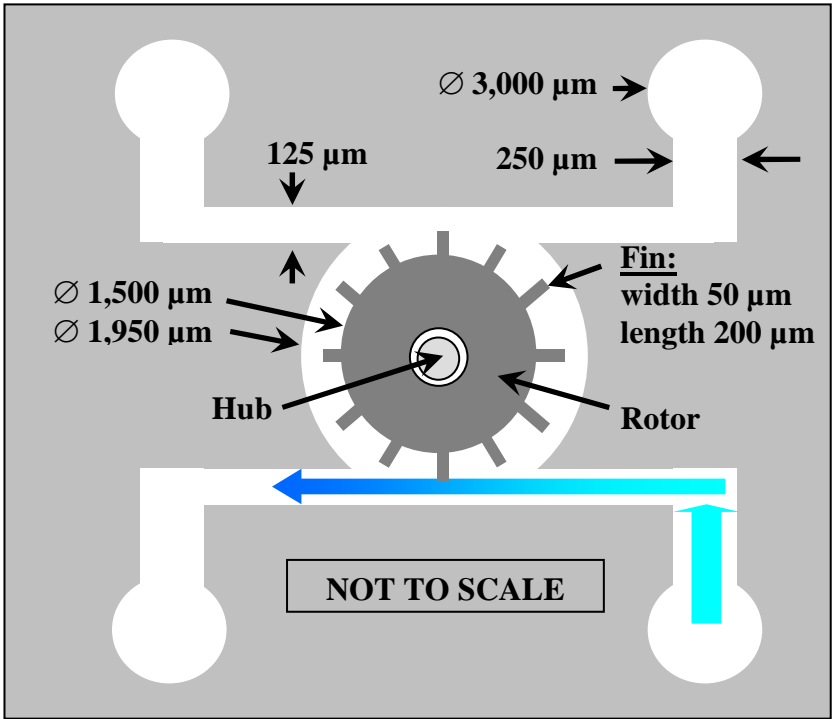


Figure 16: Microbearing assembly schematic depicts single channel nitrogen gas flow in order to rotate the rotor.

2.2.1 Phase 1 Rotor Fabrication

Figure 17 shows the fabrication sequence for Phase 1 rotors. The sequence begins with the RCA cleaning (Appendix A.1) of a double-side-polished (DSP), 100 mm diameter (100), single crystal silicon wafer. The wafer then undergoes a dehydration bake at 200 °C for 2 minutes just prior to being spin-coated with hexamethyldisilazane (HMDS) in order to promote photoresist adhesion.

Next, the wafer is spin-coated with a 4.7 μm thick layer of AZ4620 photoresist at a rotational speed of 3,000 RPM for 45 seconds. It is then placed onto a 90 °C hotplate for 2 minutes to evaporate the photoresist solvent as well as to improve photoresist uniformity, adhesion, and etch resistance.

Once photoresist coated, a portion of the wafer is exposed for 20 seconds through a reticle using a 5X projection photolithography system (GCA 6700 g-line stepper). This process is repeated 8 more times as the wafer is stepped (moved by specific increments), under the system's series of optical pattern reduction elements, to unexposed areas, resulting in a 3X3 matrix of rotor pattern designs.

Rendered soluble, the irradiated regions of the positive photoresist coating are dissolved away upon a 7 minute immersion into MF-CD-26 (tetramethylammonium hydroxide (TMAH)) developer.

A deionized (DI) water rinse is then performed for 60 seconds prior to DRIE. After DRIE, the photoresist is stripped away in a BRANSON 3200 ASHER using O₂ plasma for 4.5 minutes. The wafer now undergoes a second RCA cleaning.

In order to reduce the inherent sidewall roughness, resulting from DRIE, a technique known as “oxide polishing” is employed. A 2.5 μm thick SiO_2 layer is thermally grown on the wafer using a BRUCE horizontal diffusion furnace, rendering the resulting Si- SiO_2 interface smoother than the initial DRIE-formed sidewall. Upon the subsequent removal of this oxide layer, an averaged sidewall roughness of 300 nm Ra is obtained using a WYKO optical profilometer. This roughness value is similar to that obtained by researchers [44] for DRIE-formed silicon microchannel structures of similar aspect ratio.

In preparation for another photolithography step, the wafer is first cleaned with DI water and then with isopropyl alcohol before being air dried. It is then baked on a hotplate at 140 $^\circ\text{C}$ for 3 minutes before being spin-coated with HMDS at 3,000 RPM for 60 seconds.

A 1.5 μm thick layer of Shipley 1813 (g-line photoresist) is now spun on at 3,000 RPM for 60 seconds. This is followed by a pre-exposure bake on a 90 $^\circ\text{C}$ hotplate for 120 seconds.

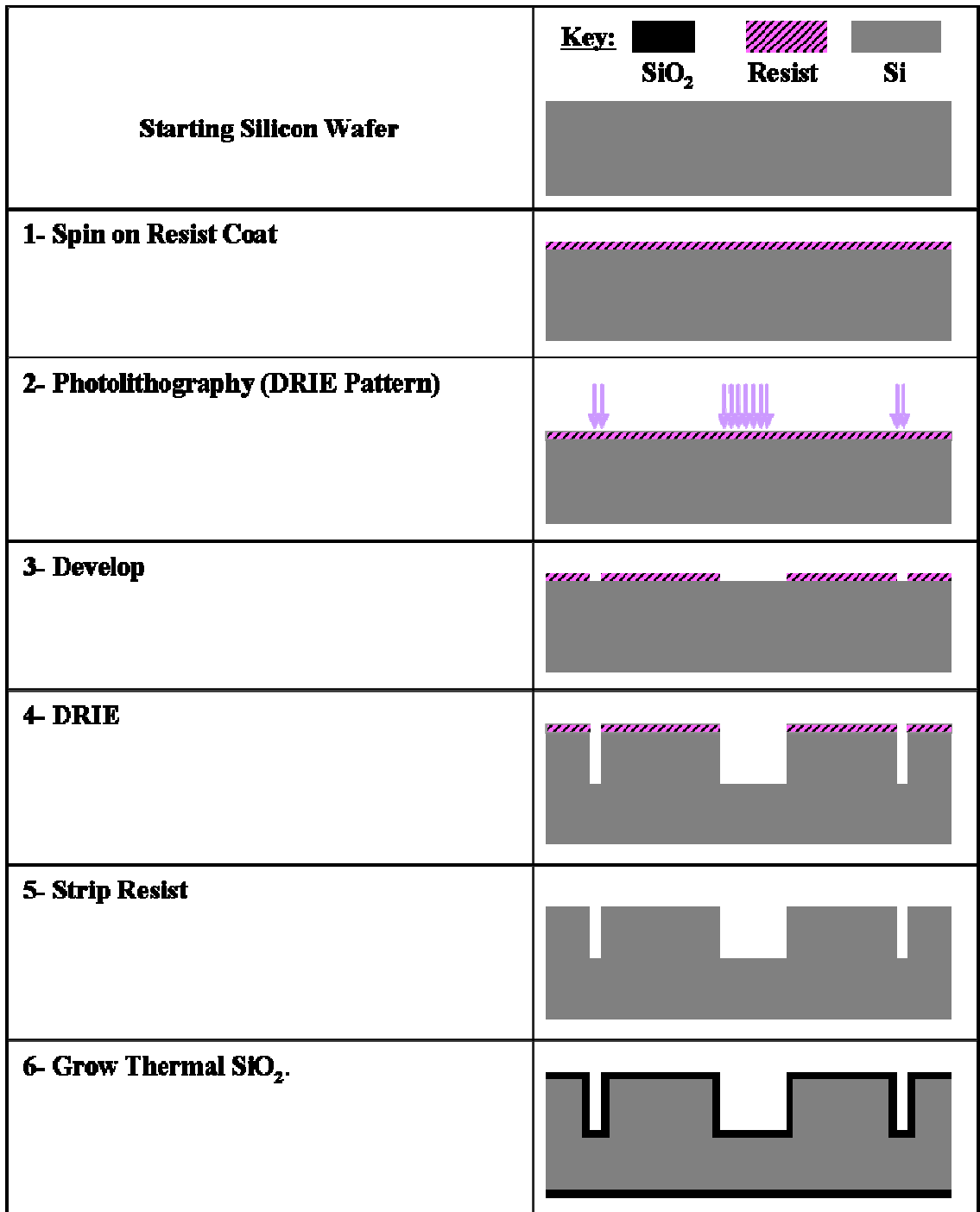
In this second photolithography step, the wafer’s backside is nearly completely exposed for 30 seconds, in hard contact mode, using a 1X photolithography system (KARL SUSS MA150 contact aligner). No special mask is required for this step. A simple ring of construction paper is taped to a blank reticle in order to mask an 8 mm annular region starting from the edge of the wafer. This is done to ensure the rigidity of the wafer for handling purposes upon subsequent KOH etching.

Once exposed, the wafer is hand developed for 120 seconds in a PYREX tray using MF-CD-26. It is manually agitated during development and subsequently inspected for clarity under an optical microscope.

The SiO₂ on the exposed backside of the wafer is then removed using a buffered oxide etch (BOE) solution containing a 10 to 1 ratio of ammonium fluoride (NH₃F) to hydrofluoric acid (HF). The wafer is then placed in DI water for 5 minutes and dried.

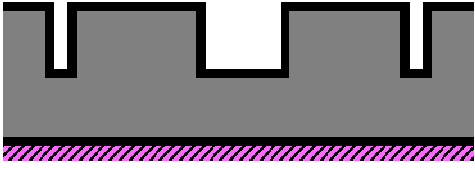
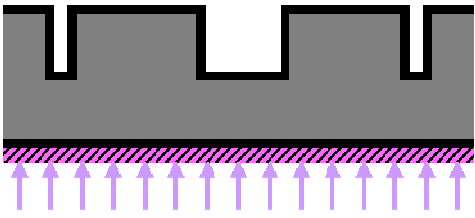


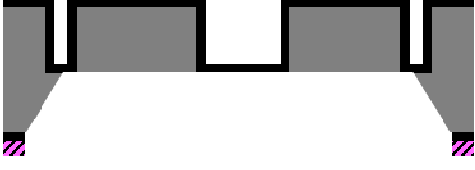

The wafer's backside is then KOH etched until the SiO₂ at the bottom of the DRIE-formed trenches is reached (~ 4 hours in this case). The 40 percent KOH solution utilized is maintained at 90 °C to achieve an etch rate of approximately 1 μm per minute.

In a final rotor release sequence, the wafer is first submersed into a 10:1 mixture of BOE with surfactant and then into DI water for periods of 60 minutes and 15 minutes, respectively, before being air dried. The intent of the surfactant is to assist in the complete removal of SiO₂, especially from the rotor bearing surfaces.



(a) Steps 1-6

Figure 17: Phase 1 rotor fabrication sequence: (a) steps 1-6; (b) steps 7-12.

<p>7- Spin on Resist Coat</p>	
<p>8- Photolithography (KOH opening)</p>	
<p>9- Develop</p>	
<p>10- HF Etch Backside</p>	
<p>11- KOH Backside</p>	
<p>12- HF Release Rotor</p>	

(b) Steps 7-12

Figure 17: (Continued)

A photograph of the KOH etched rotor wafer surface is shown in Figure 18 while a magnified optical image of a single rotor's KOH etched surface is shown in (Figure 19). The pitting seen in these photographs is indicative of non-uniform etching, most likely due to

- micro-masking by pre-existing contaminants in the KOH etch bath
- non-uniform temperature distribution of the KOH bath
- micro-masking due to hydrogen bubble accumulation

The pitting does not appear to affect rotor performance for the test cases studied in this work.

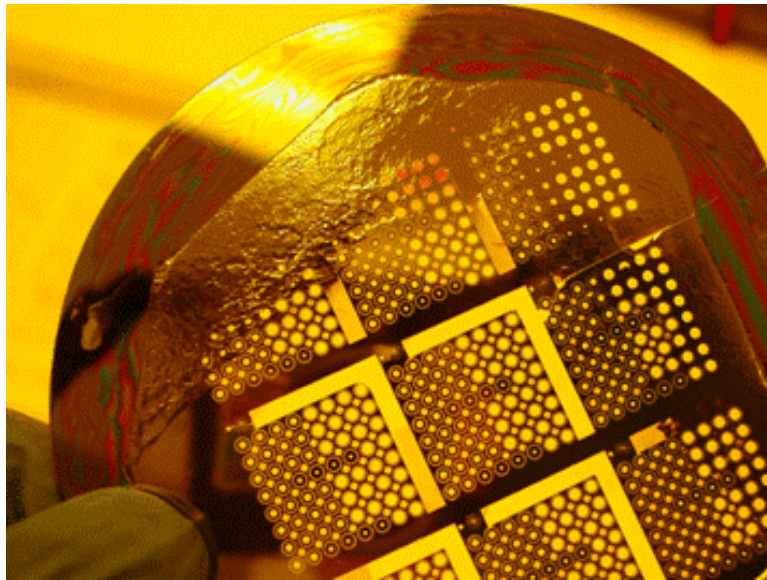


Figure 18: Wafer after release of the rotors.

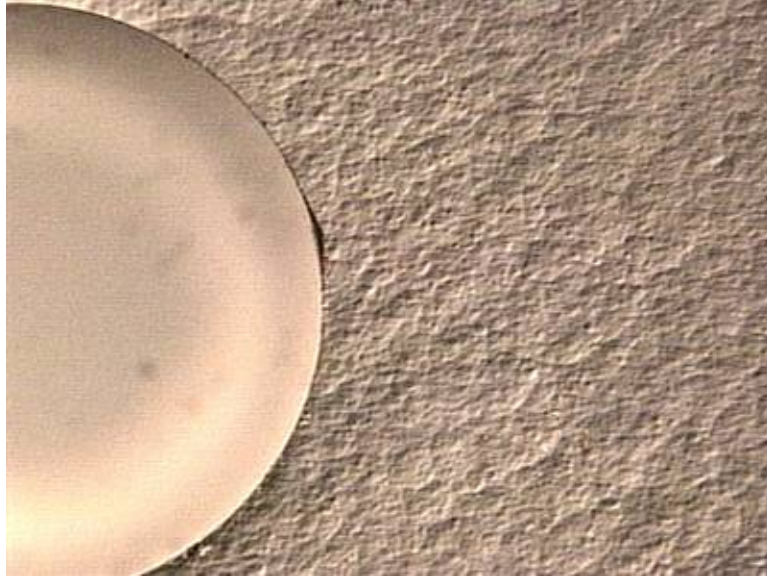


Figure 19: Magnified image of single rotor's KOH etched pitted surface.

Novel “sprue” features and a “float” etching technique enable the development of these rotors. The sprues, patterned using the DRIE mask (fabrication process step 4), hold the rotors in place during the KOH etching process. They start off as thin silicon fasteners, located on the outer diameter of the rotors between the rotor fins and on the fin tips, connecting the rotors to the rest of the wafer frame (Figure 20). The sprues are then fully oxidized during the oxide growth step and finally dissolved away during the rotor release etch step.

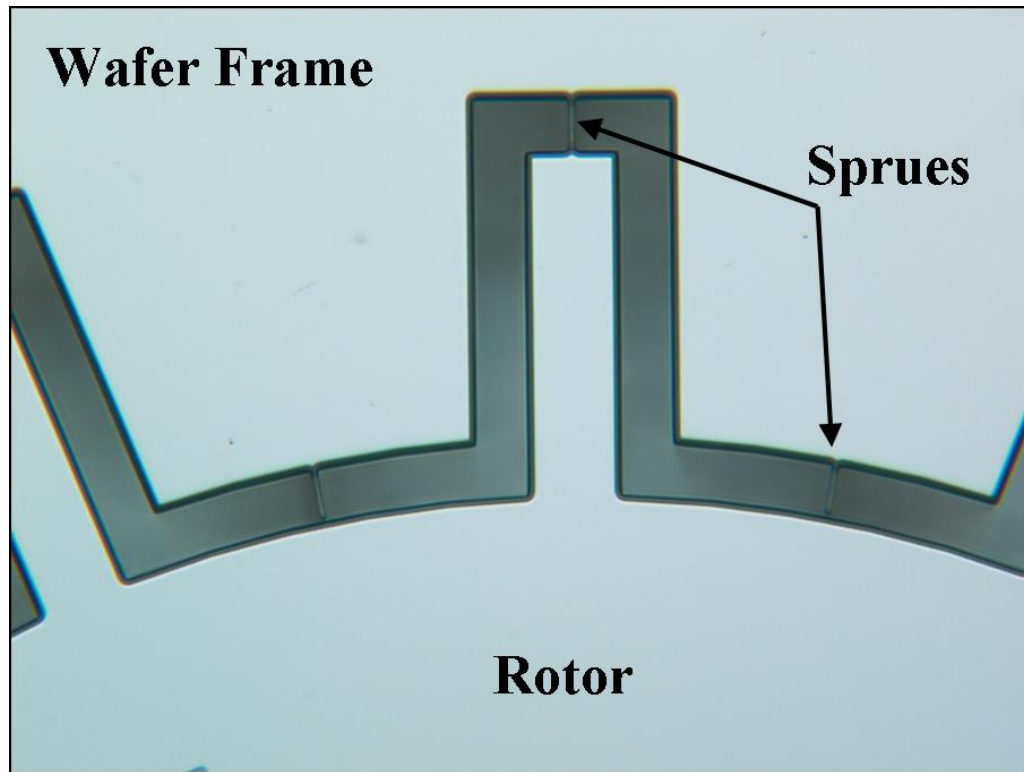


Figure 20: Optical microscope image of sprues used to hold rotor in place during KOH etching.

The float etching technique, depicted in Figure 21, entails floating the device wafer on top of the KOH etchant bath (fabrication process step 11). The rotors are oriented upward (away from the KOH bath) during this backside etch. This is done in order to prevent the rotors' top and critical vertical bearing surfaces from being etched.

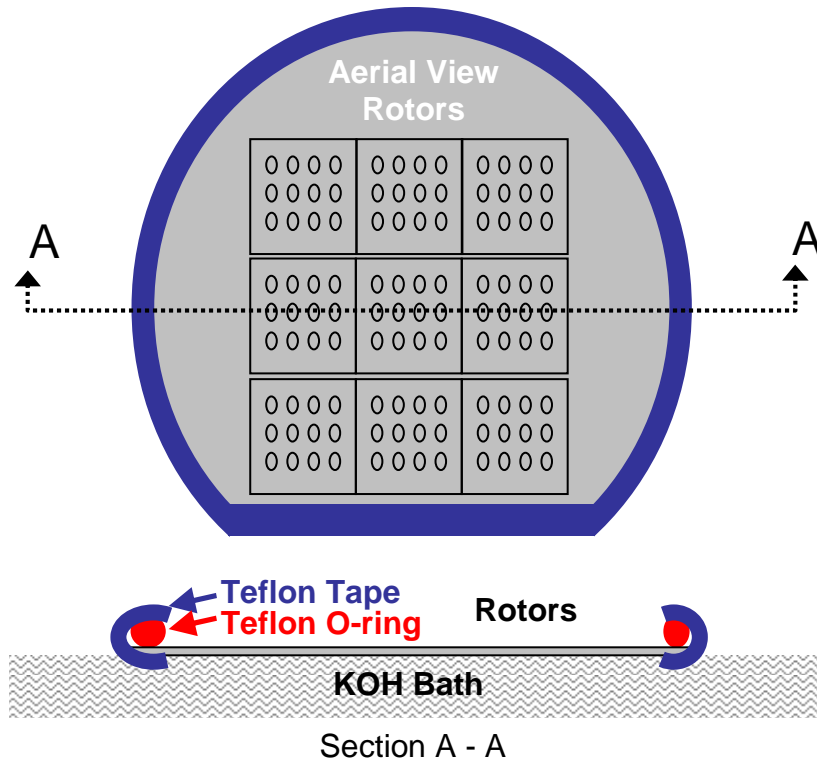


Figure 21: Schematic of the “float” etching technique depicts aerial and cross-sectional views of a wafer and Teflon O-ring circumferentially wrapped with Teflon tape.

The sprue features and the float etching technique provide the following advantages

- cumbersome and costly protective wafer rigging that is standard operating procedure when KOH etching is eliminated
- general process visualization is enhanced
- a visual etch end-point-detection scheme is introduced, thereby eliminating the need for multiple inspection withdrawals of wafers from the hot KOH bath
- process safety is enhanced and the possibility of cross-contamination is reduced as a direct result of the minimization of inspection withdrawals as well as associated logistical handling throughout the fabrication facilities
- induced thermo-mechanical stresses are minimized as a direct result of minimizing the frequency of insertions and withdrawals of the device wafers into the heated etch bath
- messy “black” waxes that are typically used for device masking are eliminated, thereby reducing cleaning and maintenance costs to equipment as well as to the actual device wafers

It should be noted that a small amount of KOH vapor condenses onto the lid of the KOH bath and drips onto the device side of the wafer. This weak condensate at a relatively lower temperature does not affect the device side of the wafer due to the thick conformal SiO₂ coating.

2.2.2 Phase 1 Hub Fabrication

To optimize material cost, the (100) single crystal starting wafer used for hub fabrication is only single side polished (SSP). In contrast to the case for rotor fabrication, a DSP wafer is no longer required as hub wafer backside etching is not employed. The fabrication sequence for the Phase 1 hub is identical to that of the Phase 1 rotor and is completed at step 5 of Figure 17.

Upon completion of step 5, the wafer is diced using a diamond wafer saw, resulting in approximately 20 mm by 20 mm bearing hub assemblies on to which the rotors are manually assembled. The hub DRIE depth must, therefore, be greater than the rotor thickness in order to seal the assembled microbearing with a glass cover slide during testing.

Once diced, an identification number is diamond scribed onto the back of the hub. The four nitrogen access holes on each hub are then manually drilled using a high-speed diamond coated tool bit. To accomplish this, the hubs are placed onto a rigid particle board laminated in smooth veneer in order to minimize flexure of the hubs upon application of drill bit pressure while allowing for possible penetration of the drill into the veneer upon nitrogen access hole breakthrough. During this delicate operation, resulting debris are continuously blown off the hub's top surface while the drill head is lightly tapped aiding in drilling end-point-visualization. In addition, the sound of drilling is used to detect completion as minimal tactile feedback is present during the operation.

Cleavage along the microchannels, during drilling, results in a hub yield rate of approximately 60 percent

In a final cleaning sequence, the hub is

- immersed in acetone for 45 minutes
- immersed in isopropyl alcohol for 15 seconds
- sprayed thoroughly with DI water
- dried using an air gun

Upon completion, the hubs are stored with their DRIE-formed surfaces facing down in a corrugated container to minimize debris accumulation inside the test cavities.

Figure 22 shows a diced hub prior to and after nitrogen access hole drilling, respectively, while Figure 23 shows a magnified SEM micrograph of the hub geometry. It is evident from this image that the bottoms of the access holes are not perfectly circular. This is due to the abrupt cleavage of these thin silicon membranes along their crystal planes upon drill breakthrough. Any remnants not rigidly attached to the hub should be removed as they may inadvertently dislodge upon the application of nitrogen pressure during testing, resulting in flow blockage or rotor destruction. Care must be taken, however, in any attempt to break off remnants of concern in order to prevent the entire die from cleaving. A diamond wafer scribing pen was used in several cases to accomplish this task.

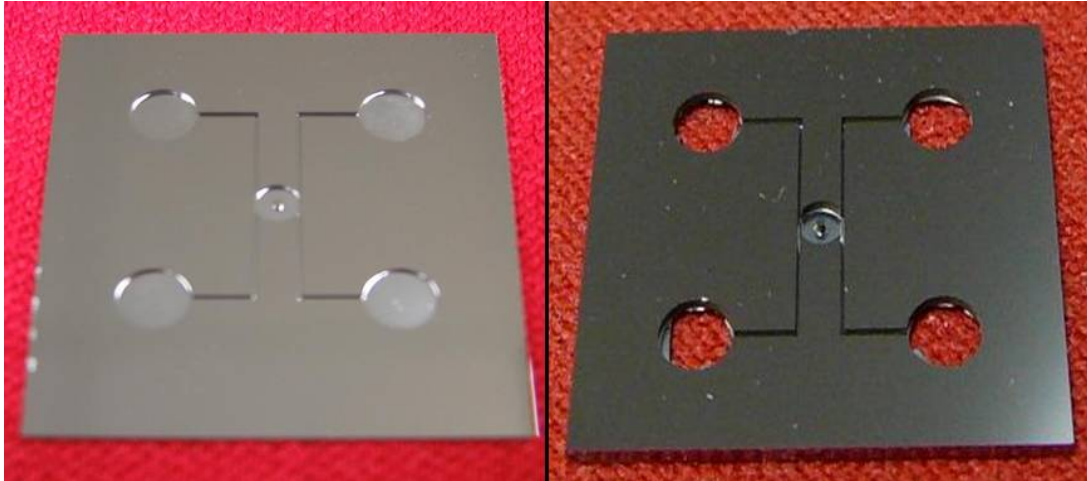


Figure 22: Diced Phase 1 hubs (pre-drilled (left) and post-drilled (right)).

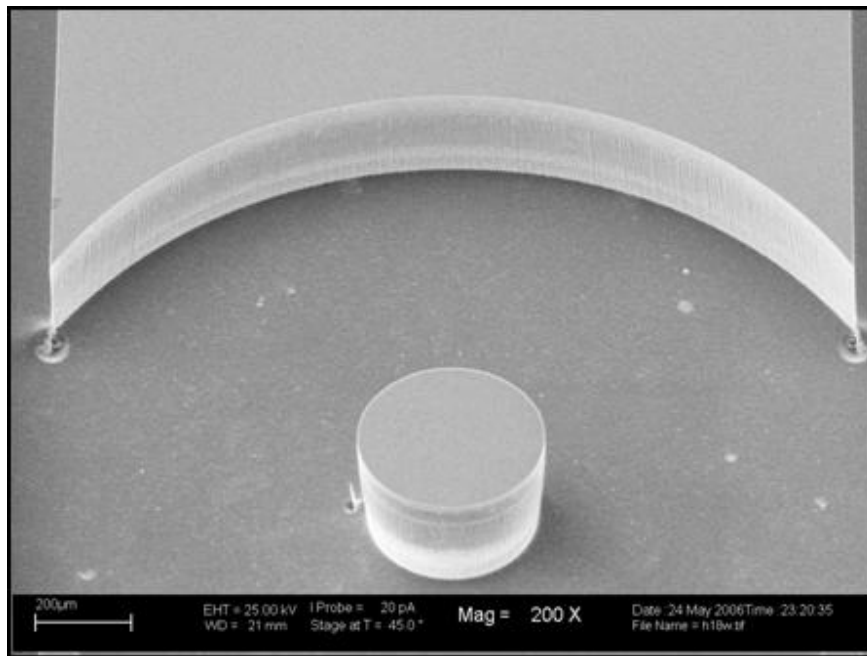


Figure 23: SEM micrograph of Phase 1 hub.

2.3 Phase 2 Microbearing System

Figure 24 shows an exploded view schematic of a representative Phase 2 microbearing characterized by a rotor-hub (analogous to Phase 1) system. In accordance with the system design intent of achieving custom bearing clearances and configurations, Phase 2 microbearings are also designed for manual assembly. Four significant changes, however, are made in the development of the Phase 2 microbearing systems with the aid of lessons learned from Phase 1. Changes related to the hub design are first covered, followed by changes related to the rotor.

First, as illustrated in Figure 24, compressed nitrogen gas will now be supplied to the rectangular microchannel from the hub's top surface via a 3 mm in diameter feed hole, thereby eliminating the need for drilling access holes completely through the brittle silicon as was done in Phase 1. Several significant benefits arise from the elimination of the drilling procedure including

- a device yield increase via the elimination of drilling induced cleavage
- the elimination of the possibility of destruction by way of loose silicon drilling remnants dislodging and striking the rotor upon system pressurization
- a reduction in possibility of nitrogen leakage, since only the top surface of the hub now requires sealing
- the elimination of post-drilling cleaning procedures, thereby reducing the possibilities of handling damage and residual contamination

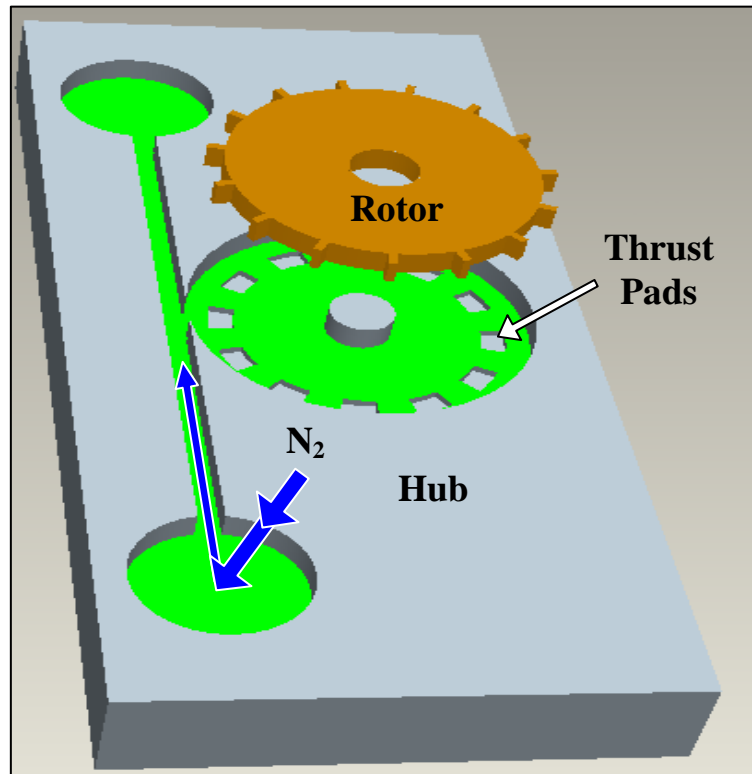


Figure 24: Exploded view of Phase 2 microbearing design depicts hydrodynamic sectorial, step thrust bearing pads.

Second, two types of hubs, one with sectorial, step thrust bearing pads, shown schematically in Figure 24, and one without (not shown), are designed to be fabricated on separate wafers, respectively. The thrust bearing pads, incorporated at the bottom of the hub's base, are defined using a separate photolithographic mask pattern. The design intent of these pads is to promote gas lubrication between the bottom of the rotor and the base of the hub, thereby reducing contact friction and in turn, increasing rotor rotational speed.

Due to current MEMS-based technology fabrication constraints, the most feasibly implementable self-acting thrust bearings are stepped thrust bearings. The theory of these bearings (also referred to as Rayleigh stepped bearings) was first discussed by Rayleigh in 1918, when he determined the optimum geometry for maximum load capacity for 1-dimensional stepped bearings. Later, Archibald [45] discussed the load carrying capacity of the stepped sectorial thrust bearing depicted in Figure 25, where radii R_i and R_o and angles θ_1 and θ_2 represent the sectorial boundaries. A representation of the moving rotor (included on the top of the cross-sectional view) is removed from the axial view (left) in this figure for clarity. The film thicknesses above each sector are represented by h_1 and h_2 (i.e., h_2 represents the film thickness between the bottom of the rotor and the bottom surface of the thrust pad).

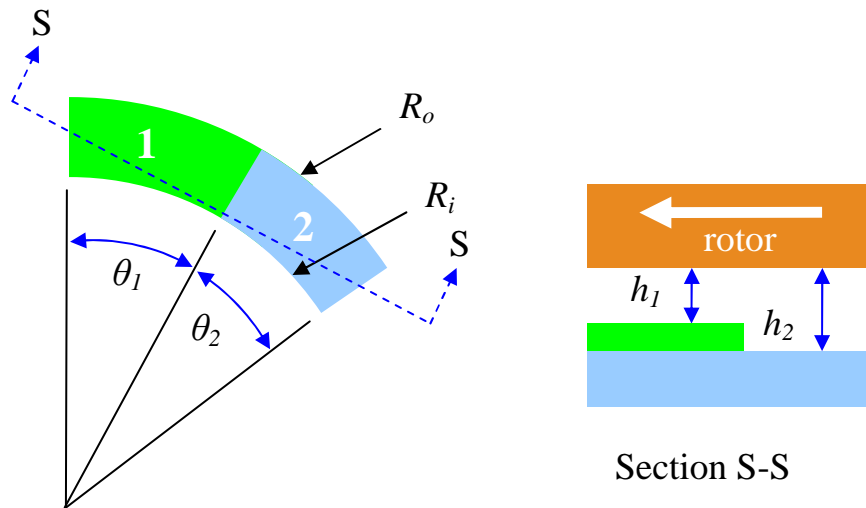
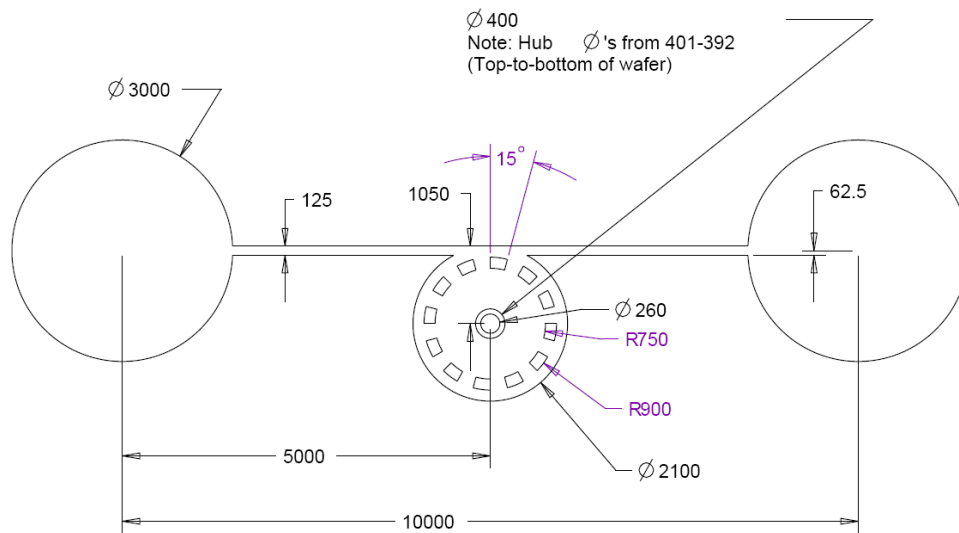
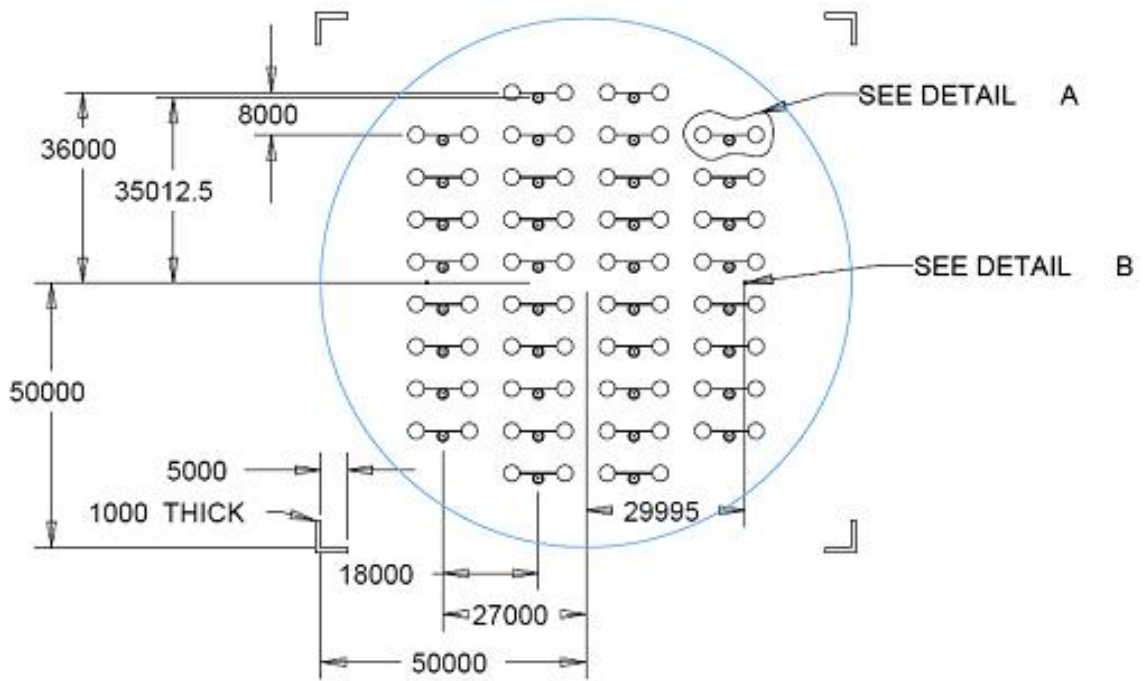


Figure 25: Axial (left) and cross-sectional (right) views of a sectorial, step thrust bearing. The moving rotor shown in Section S-S is omitted in the axial view for clarity.

Third, as depicted in Figure 26, all Phase 2 hubs incorporate straight, single, nitrogen flow microchannels that are shorter in length than those in Phase 1. Consequently, the device yield per wafer is increased by 400 percent, from 9 hubs to 36, in turn, resulting in a reduction of unit fabrication cost. Additionally, manufacturing concerns pertaining to inter-wafer process uniformity are now mitigated. As a final benefit, attributable to the straight and shortened microchannel design, a lower nitrogen supply pressure is required to achieve Phase 1 rotor operational speeds.

In the fourth and final significant hub design change, the need for wafer dicing is eliminated as the test apparatus and methodology, to be discussed in Chapter 3, is re-engineered to incorporate the entire wafer. The elimination of this wafer dicing step minimizes cost while maximizing yield, by eliminating the possibility of wafer damage during dicing as well as associated intermittent handling and post-dicing cleaning procedures.

As is illustrated in Figure 26 (Detail A), a maximum of 10 hub diameters (two middle columns), ranging vertically on the wafer, from 401-392 μm , in increments of 1 μm , are designed on the mask. This mask design layout mitigates concerns related to intra-wafer device uniformity by taking into consideration radially dependent fabrication processing such as DRIE. In this work, since the hub diameters in each row are equal, radially equidistant hubs in each row will be nearly identical when processed. In a final note pertaining to the wafer hub design, the spacing between successive hubs is constrained by the size of the experimental fixture gas connectors described in Chapter 3.



DETAIL A
SCALE 20.000

Figure 26: Hub wafer design layout. Detail A depicts a single hub to which a rotor will be assembled to. Detail B (not shown) contains custom wafer alignment features. All dimensions are in μm unless otherwise denoted.

The Phase 2 rotor mask design layout, shown in Figure 27, incorporates eight identical metrology blocks (enlarged in Figure 28) which include 1 μm sized minimal features that are used for both intra- and inter-wafer fabrication process monitoring and device comparison. A maximum of ten rotors (shown together in Figure 29 for comparison and depicted at higher magnification in Appendix B.1 for clarity), designed to be distinguishable by the unaided eye for rapid sorting and test selection, are patterned radially on this mask. Since achieving an ample rotor sample size for testing is of concern, this radial configuration is then patterned circumferentially in 15 degree increments, resulting in a maximum of 24 identical rotors of each design and thereby mitigating concerns related to radial dependent processing.

The microbearings in this phase are designed to have L/D ratios ranging from 0.4 (similar to Phase 1 microbearings) to 0.7. Since the hub bearing diameters are designed to be on the order of 400 μm , rotors with different bearing lengths are fabricated on separate wafers. It is important to note that in the event of either wafer under- or over-etching, rotors 1, 3, and 5 are each designed with bearing diameters that differ slightly from the rest of the 400 μm bearing diameter rotors. Moreover, this design methodology potentially broadens the range of possible bearing clearances.

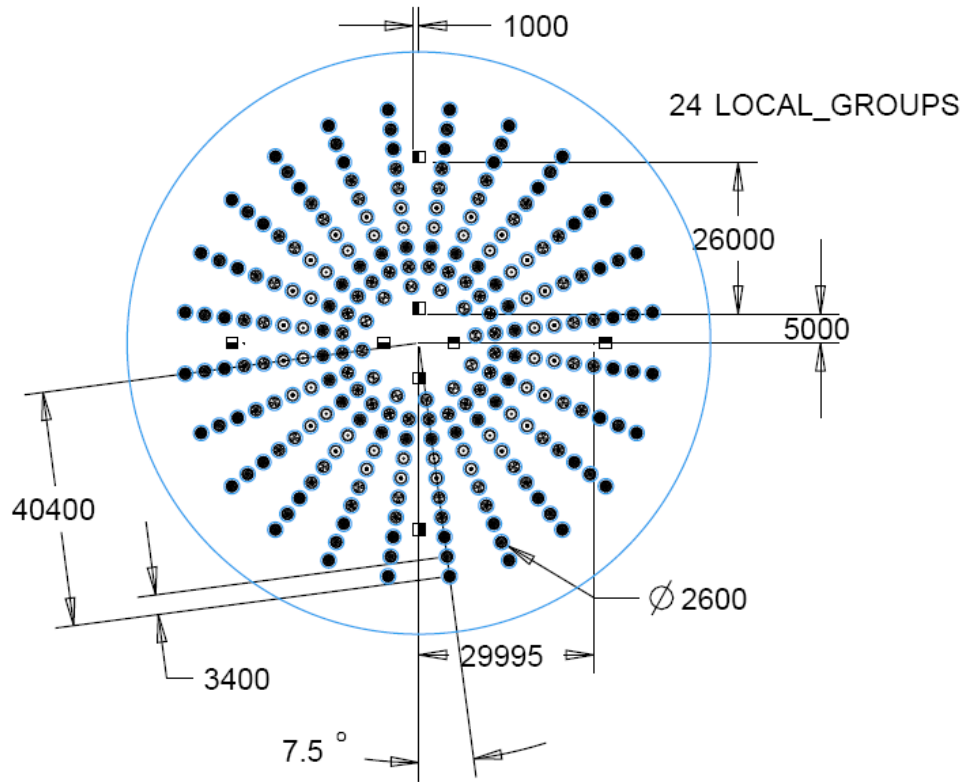


Figure 27: Rotor mask design layout. All dimensions are in μm unless otherwise denoted.

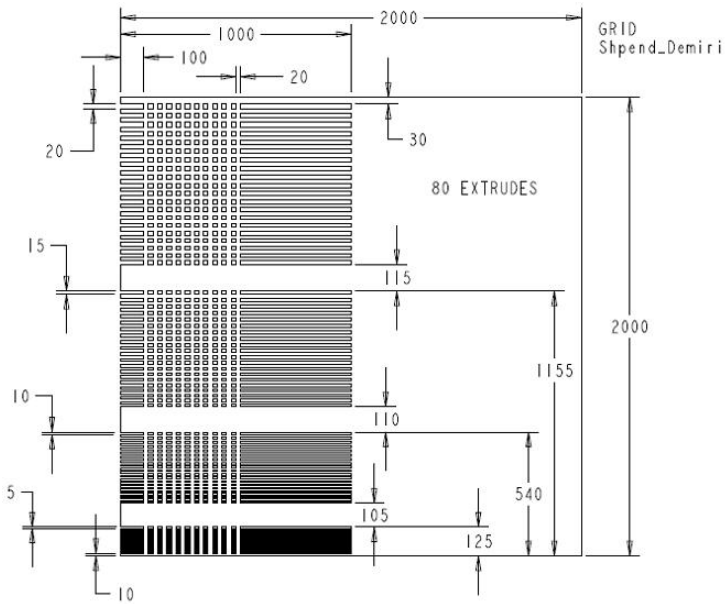


Figure 28: Process monitoring metrology blocks containing $1\ \mu\text{m}$ minimum features.

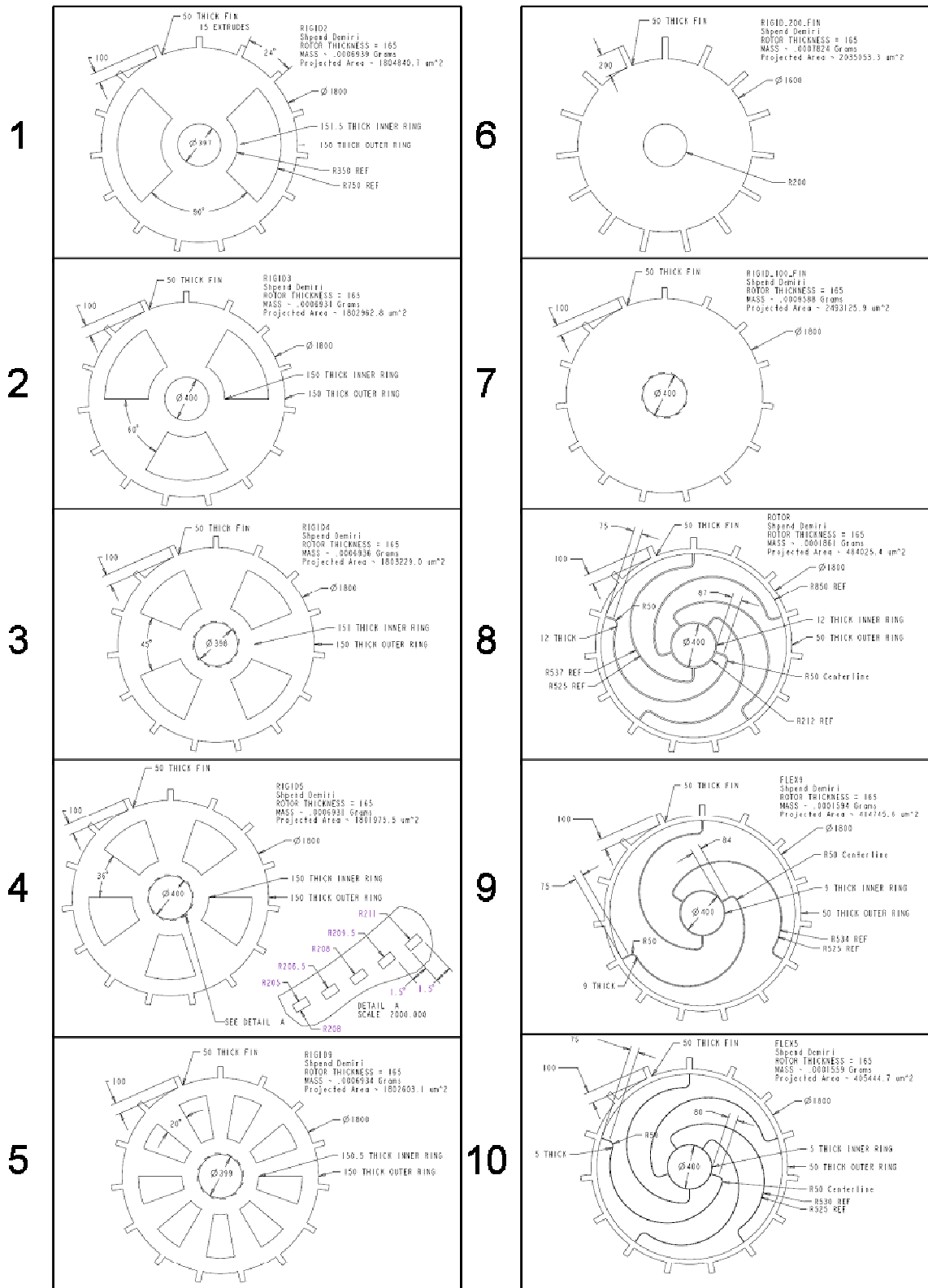


Figure 29: Phase 2 rotor geometries.

Novel *in situ* “wear indicators” (enlarged in Figure 30 (Detail A)), intended to facilitate the rapid quantitative and qualitative determination of wear, are incorporated in the designs of rotors 3, 4, 5, and 7. Moreover, the incorporation of these built-in metrology features eliminates the need for expensive metrology hardware, software, and associated repetitive calibrations. A relatively inexpensive handheld magnifying glass is all that is required for rotor sample wear comparisons.

Each of the 5 sectorial wear indicators per set is characterized by a 3 μm radial length and 1.5 degree arc span. The first wear indicator in a set begins 5 μm from the rotor bearing surface. Successive wear indicators are patterned radially and circumferentially in increments of 1.5 μm and 1.5 degrees, respectively, resulting in a 1.5 μm maximum wear resolution. The resulting set is then patterned circumferentially in increments of 30 degrees, enabling the determination of non-concentric wear. In order to minimize their effect on wear, indicators should be as superficial as possible, requiring both infinitesimal radial lengths and DRIE depths. It is important, therefore, to note that the equipment and fabrication process capabilities, particularly those related to photolithography, constrain the wear indicator design geometries used herein.

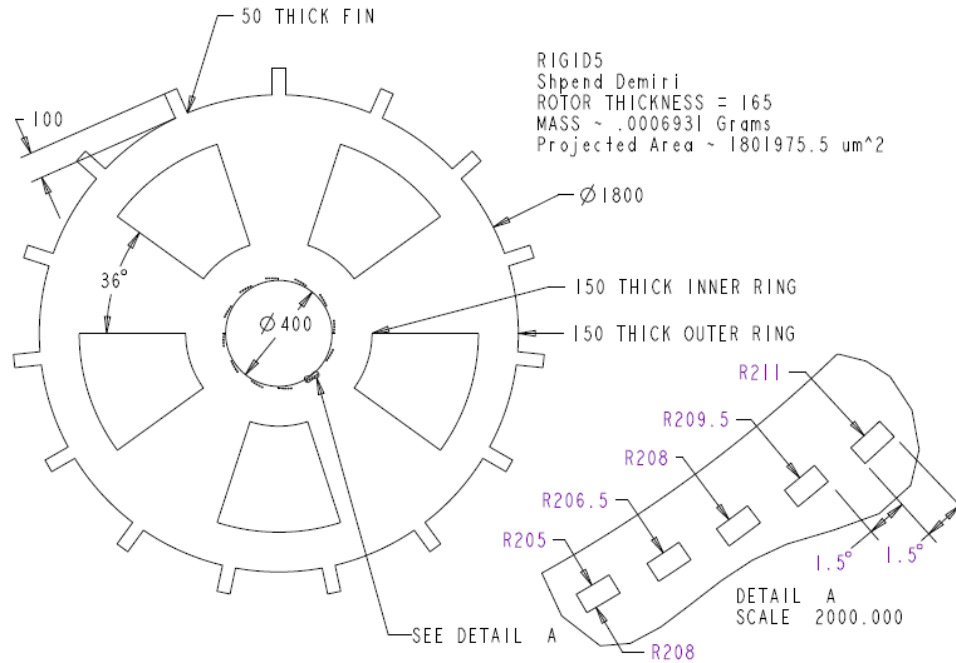


Figure 30: Rotor schematic depicts novel *in situ* wear indicators.

Rotors 1-5 are designed to be rigid and nearly identical in mass and contain 2, 3, 4, 5, and 9 spokes, respectively, in order to facilitate identification. While the fin tip-to-tip diameters of rotors 6 and 7 are identical, rotor 7's outside diameter is larger, resulting in shorter fins. In contrast to rotors 1-7, novel compliant design geometries are employed for rotors 8-10. The design intents of the thin (on the order of 5-12 μm) inner rings and fasteners are to render the rotor locally and globally elastic, respectively. Upon considering the limitations imposed by the available MEMS fabrication technologies, the smaller feature thickness limit of 5 μm is based on achieving the approximately 200 μm bearing length considered here. Furthermore, as the salient feature thickness decreases, the consequential increase in rotor frailty renders rotor-to-hub assembly increasingly challenging.

2.3.1 Phase 2 Rotor Fabrication

A 100 mm diameter, double-side-polished, (100) single crystal silicon wafer, containing a 2 μm thick layer SiO_2 , is utilized in the fabrication of Phase 2 rotors. The thickness of this thermally grown SiO_2 is verified using a PROMETRIX SM300 SPECTRAMAP. In preparation for processing, the wafer then undergoes a dehydration bake at 200 $^\circ\text{C}$ for 2 minutes just prior to being spin-coated with hexamethyldisilazane (HMDS) at 3,000 RPM for 20 seconds in order to promote photoresist adhesion.

Figure 31 shows the remainder of the major rotor fabrication sequence steps beginning with the wafer being spin-coated with a 3.0 μm thick layer of MEGAPOSIT SPR 220-3.0 positive photoresist at a rotational speed of 3,000 RPM for 30 seconds. It is then placed onto a 115 $^\circ\text{C}$ hotplate for 90 seconds to evaporate the photoresist solvent as well as to improve photoresist uniformity, adhesion, and etch resistance.

Once photoresist coated, the wafer is exposed for 9 seconds (a time determined using a dose mask to expose sectorial regions of a process characterization wafer), in hard contact mode, using an HTG System III-HR contact aligner. A post exposure bake, used to reduced standing waves, is then performed at 115 $^\circ\text{C}$ for 90 seconds.

After exposure, the wafer is developed for 60 seconds in a HAMATECH-STEAG single wafer spin processor using AZ-300-MIF (tetramethylammonium hydroxide (TMAH)). A deionized (DI) water rinse is then performed for 60 seconds.

The 2.0 μm thick layer of thermal SiO_2 is then removed using a fluorine based OXFORD PLASMALAB 100 inductively coupled plasma (ICP) etcher. Before

removing this oxide, however, an oxygen-plasma clean is performed using a “dummy” silicon wafer. As the thermal oxide on the device wafer is relatively thick, the ICP etcher must be constantly monitored for overheating. In such an event, 30 minute long intermittent cooling shut downs may be required to complete the etch process. Upon completion of this etch step, the wafer is placed into a bath of hot (75 °C) photoresist stripper (AZ300T) for 60 minutes.

A single chamber inductively coupled plasma / reactive ion etcher (UNAXIS 770 SLR ICP Deep Silicon Etching system) is used to DRIE the patterned rotors. The passivation step of the DRIE process is performed for 5 seconds at 24×10^{-3} Torr, using mass flow rates of 70 sccm, 2 sccm, and 40 sccm for C_4F_8 , SF_6 , and Ar, respectively. RIE and ICP power settings for the passivation step are 0.1 W and 850 W, respectively. The passivation step is followed by a 2 second etch step at 23×10^{-3} Torr to remove the passivation coating at the bottom of the channel, using mass flow rates of 2 sccm, 70 sccm, and 40 sccm for C_4F_8 , SF_6 , and Ar, respectively. RIE and ICP power settings for this first etch step are 8 W and 850 W, respectively. This is followed by a 5 second etch step at 23×10^{-3} Torr to remove the exposed silicon material, using mass flow settings of 2 sccm, 100 sccm, and 40 sccm for C_4F_8 , SF_6 , and Ar, respectively. RIE and ICP power settings for this second etch step are 8 W and 850 W, respectively. It should be noted that there is a 1 second lag between each of the preceding DRIE steps. Upon the completion of this DRIE step, an oxygen-plasma clean (using a BRANSON 3200 ASHER) is performed for 120 seconds to remove any residual passivation coating.

In preparation for wet oxidation, the wafer is RCA cleaned. A 1 μm thick layer of oxide is then thermally grown on the wafer in the BRUCE furnace using Recipe 168 (Appendix A.2).

A 1.5 μm thick layer of Shipley 1813, g-line photoresist is now spun on at 3,000 RPM for 60 seconds. This is followed by a pre-exposure bake on a 90 °C hotplate for 120 seconds.

In this second photolithography step, the wafer's backside is nearly completely exposed for 30 seconds, in hard contact mode, using a 1X photolithography system (KARL SUSS MA150 contact aligner). No special mask is required for this step. Prior to exposure, a simple ring of thick construction paper is taped to a blank reticle in order to mask an 8 mm annular region starting from the edge of the wafer. This is done to ensure the rigidity of the wafer for handling purposes upon subsequent KOH etching.

Once exposed, the wafer is hand developed for 120 seconds in a PYREX tray using MF-CD-26. It is manually agitated during development and subsequently inspected for clarity under an optical microscope.

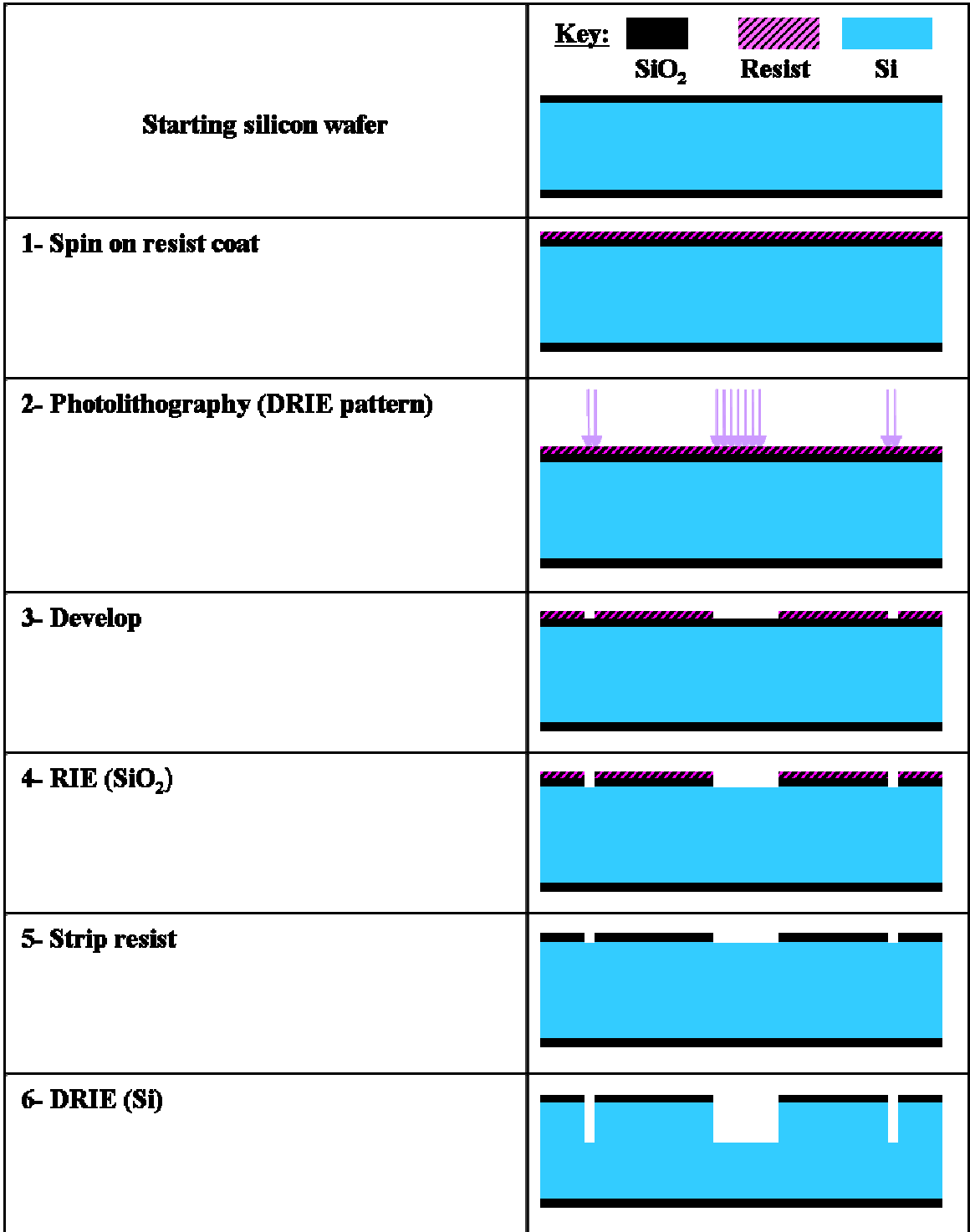
The SiO_2 on the exposed backside of the wafer is then removed using a BOE solution containing a 10 to 1 ratio of NH_3F to HF. The wafer is then placed in DI water for 5 minutes and dried.

In deviating from the KOH etching technique used for Phase 1 rotor fabrication, the Phase 2 rotor wafer is completely immersed vertically into the KOH bath. The 40 percent KOH solution is maintained at 90 °C to achieve an etch rate of approximately 1 μm per minute. To protect the rotors from etching, a so-called "device sandwiching" procedure is developed. In this procedure, the polished side of a dummy silicon wafer is

first placed adjacent to the DRIE-formed side of the rotor wafer. The corresponding wafer flats are then oriented so that they are in a co-linear configuration. Finally, this wafer sandwich is circumferentially wrapped with Teflon tape, creating a hermetic seal between the two wafers. Once immersed into the KOH, the wafers are etched until the sandwiched rotor pattern is visible. It is observed that some rotors start dislodging from random wafer locations soon after the DRIE-formed pattern begins to emerge. This is due to the insufficiently thick 1 μm thermal oxide intended to temporarily withstand the KOH. In an attempt to salvage the remaining intact rotors the wafer is immediately removed from the KOH etchant. After inspection, it is determined that the intra-wafer etch uniformity achieved in this Phase is substantially better than that achieved in Phase 1. Additionally, pitting is no longer visible with the unaided eye. These improved characteristics are attributed to

- the freshly prepared KOH bath, free of black wax and other contaminants
- and the vertical immersion of the wafer into the bath, thereby eliminating the underside coalescence of micro-masking bubbles

In a final rotor release sequence, the wafer is first submersed into a 10:1 mixture of BOE with surfactant and then into DI water for periods of 30 minutes and 15 minutes, respectively, before being air dried. The intent of the surfactant is to assist in the complete removal of the thermally grown SiO_2 , especially from the rotors' bearing surfaces. Upon completion of this process step, it is determined that a sufficient KOH etch depth was not achieved rendering the rotors unusable.



(a) Steps 1-6

Figure 31: Phase 2 rotor fabrication sequence: (a) steps 1-6; (b) steps 7-12.

7- RCA clean	
8- Grow thermal SiO ₂	
9- Spin on Resist Coat	
10- Photolithography (KOH opening)	
11- Develop	
12- HF Etch Backside	
13- KOH etch backside	
14- HF rotors (release)	

(b) Steps 7-12

Figure 31: (Continued)

Figure 32 shows a photograph of a rotor wafer after DRIE (Step 5). Radial dependent etching of the thermally grown SiO_2 is evident from the photograph as signified by the color change along the peripheral annular region of the wafer, where the SiO_2 is measured to be thickest. The design intent of this circumferentially patterned rotor layout is, therefore, considered fulfilled.

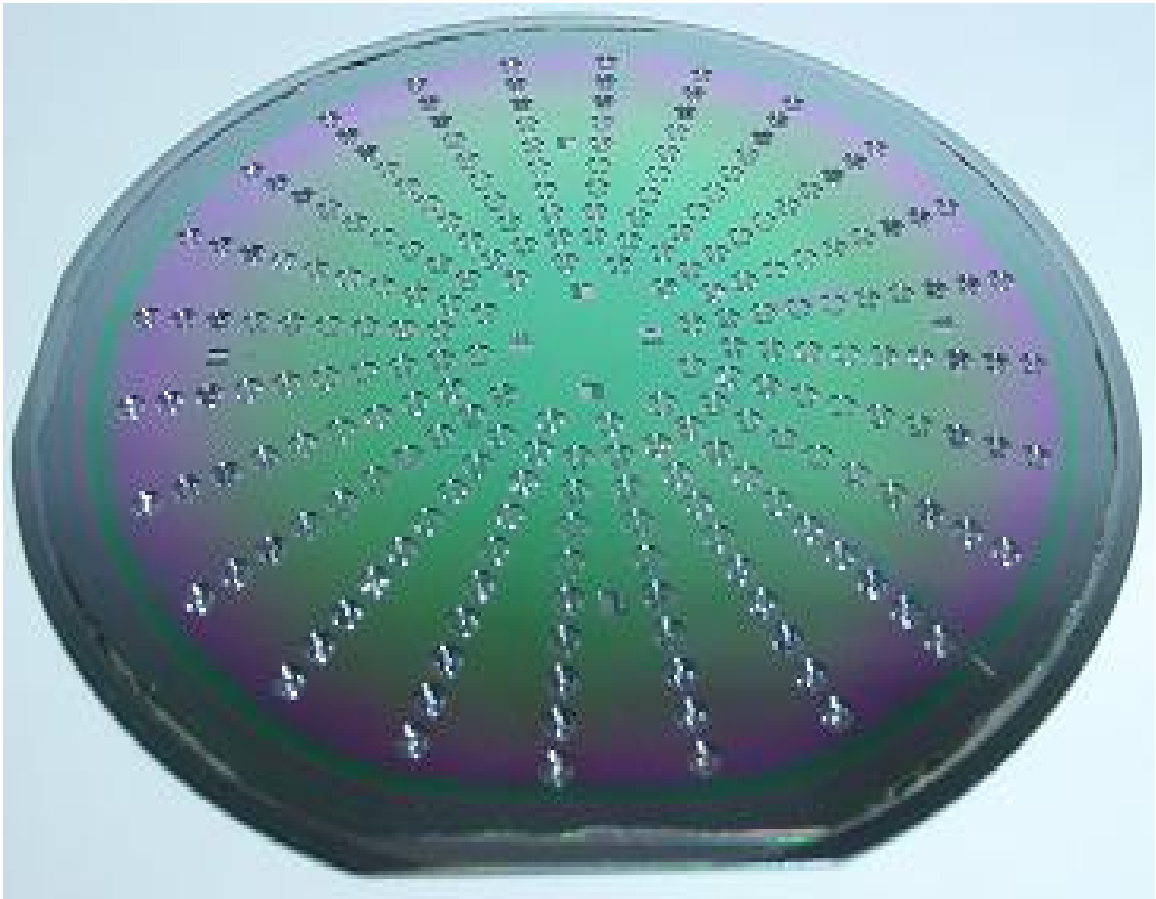


Figure 32: Photograph of rotor wafer after DRIE.

Figure 33 shows an SEM micrograph and a magnified optical image of a Phase 2 rotor after DRIE, characterized by the successful incorporation of wear indicator features. At higher magnification, the DRIE-formed wear indicators are observed to be oval in shape as opposed to sectorial. This is due, primarily, to the laser spot size utilized in writing the photolithography mask. A smaller laser spot size yields a higher resolution and hence sharper corners.

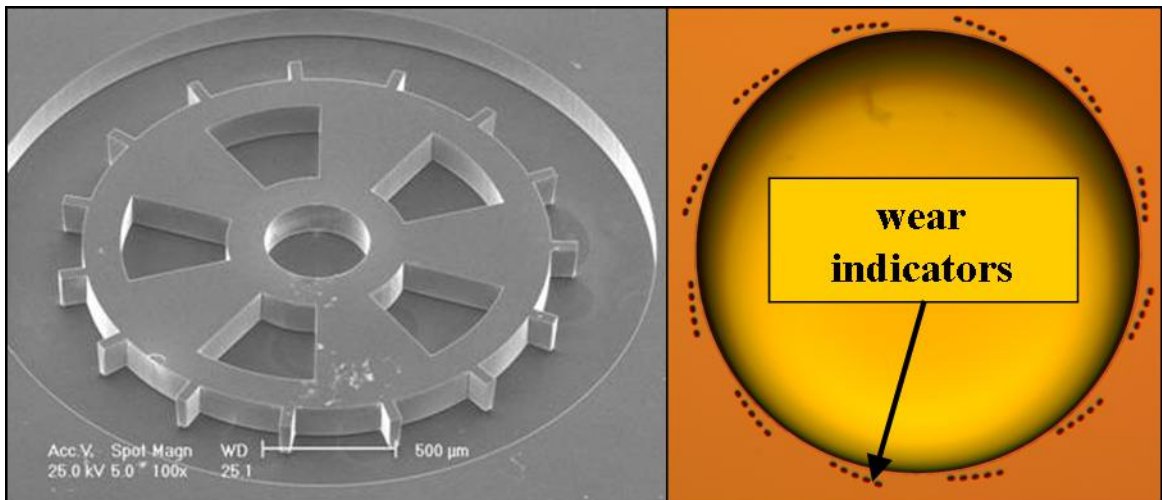


Figure 33: SEM micrograph depicts the geometry of a Phase 2 rotor after DRIE (left). Magnified image depicts an axial view of the rotor wear indicator features (right).

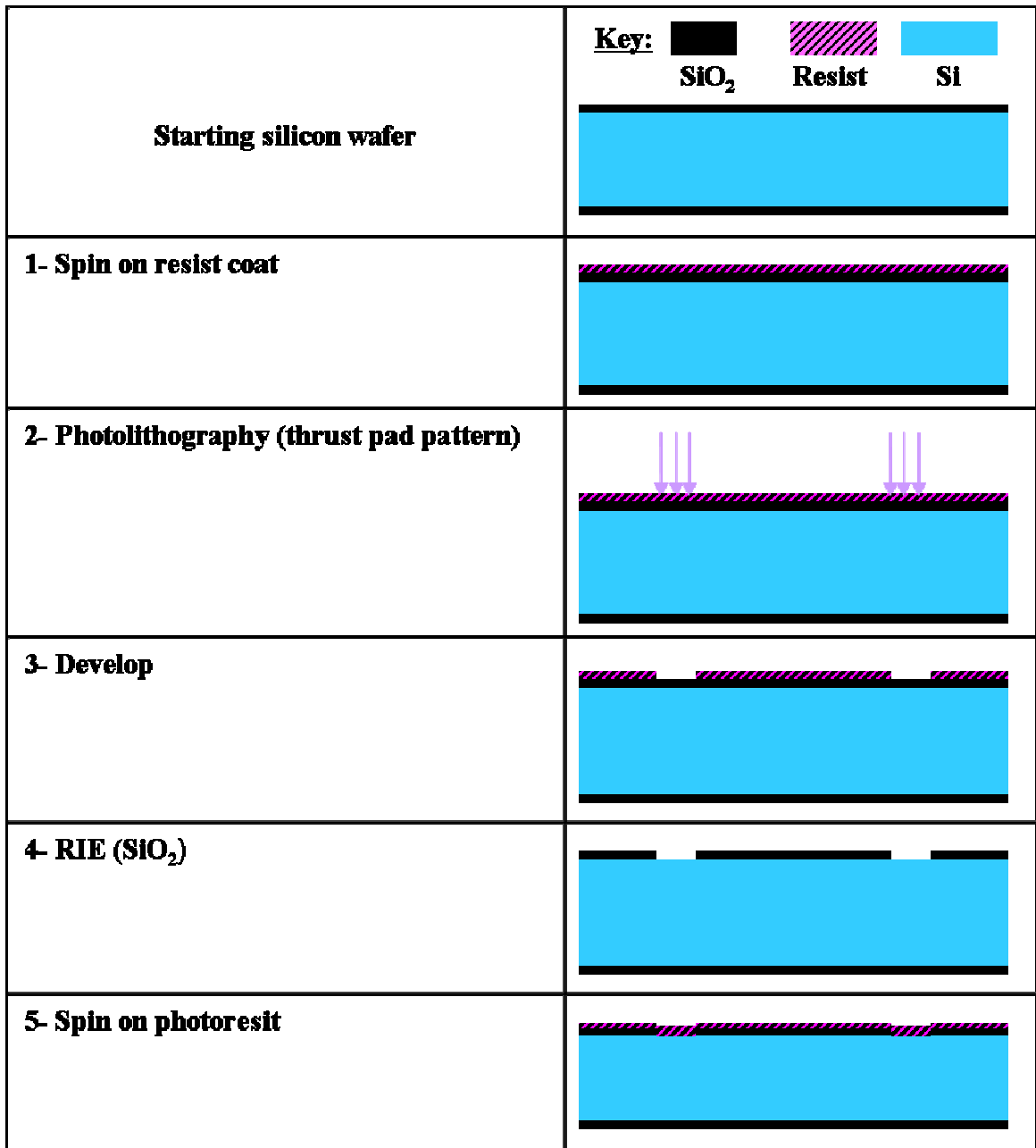
2.3.2 Phase 2 Hub Fabrication

Following the reasoning described for Phase 1 hub fabrication, Phase 2 hubs are fabricated on the same type of (100) single crystal, single side polished wafer substrates. The fabrication sequence for the Phase 2 hub, without thrust pads is identical to that of the Phase 2 rotor through step 8 of Figure 31. As was the case in Phase 1, the hub DRIE depth must be greater than the rotor thickness for subsequent sealing during testing.

After performing this oxide polishing process step, the thermally grown SiO₂ is removed using a BOE solution containing a 10 to 1 ratio of NH₃F to HF. The wafer is then placed in DI water for 5 minutes and dried. Once the processing sequence is completed, the hub wafer is stored with its DRIE-formed surface facing down in a wafer container to minimize debris accumulation inside the test cavities.

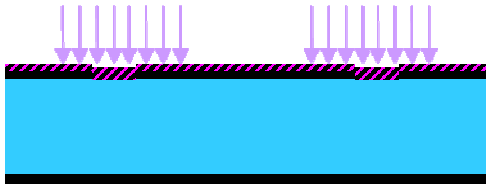



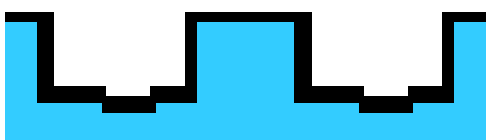

The process for fabricating hubs with sectorial stepped thrust pads is depicted in its entirety in Figure 34. It entails the insertion of steps 2 through 4 into the aforementioned Phase 1 hub (without thrust pads) process sequence. As is evident from Figure 34, a separate photolithography mask, containing the thrust pad pattern, is required.

Figure 35 shows a photograph of a completed hub wafer. Figure 36 depicts the successful incorporation of the first known microsystems-based stepped thrust bearings pads.



(a) Steps 1-5

Figure 34: Phase 2 fabrication sequence for hubs with thrust pads: (a) steps 1-6; (b) steps 6-11.

6- Photolithography (DRIE hub pattern)	
7- Develop	
8- RIE (SiO₂ and Si)	
9- DRIE Si	
10- Grow thermal SiO₂	
11- BOE SiO₂	

(b) Steps 6-11

Figure 34: (Continued)



Figure 35: Photograph of Phase 2 hub wafer.

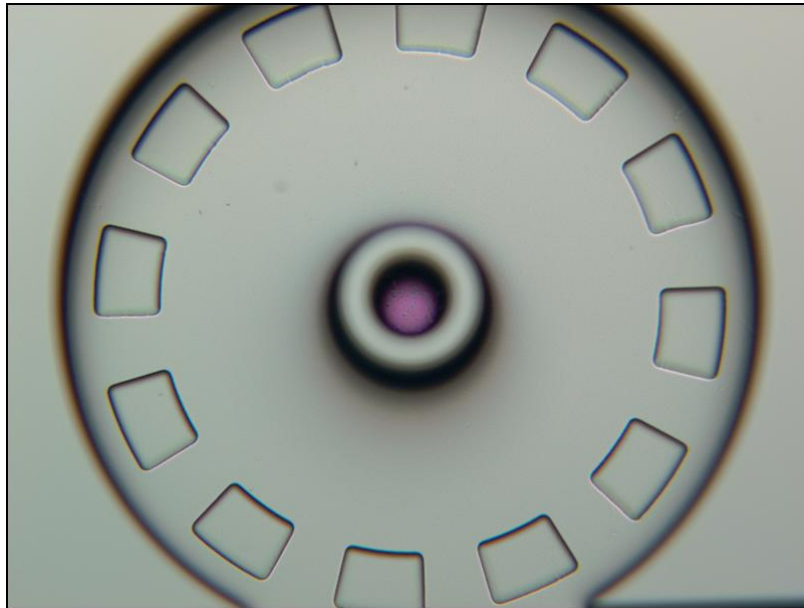


Figure 36: Optical image of Phase 2 hub depicts thrust pads.

3 EXPERIMENTAL TESTING

This chapter presents the experimental aspects of this work for both phases, including the test setup and test procedures used. The apparatus developed for testing and metrology is also detailed. Apparatus schematics are presented in the Appendix. Detailed discussions of the experimental results are presented in Chapter 4.

3.1 Phase 1 Testing

The primary intent of Phase 1 testing is to investigate conformality effects on the wear of microbearings. The following three sections present the test setup, test procedures, and experimental results.

3.1.1 Phase 1 Test Setup

A photograph and schematic of the Phase 1 experimental test setup are shown in Figure 37 and Figure 38, respectively. The optical bench is pressurized during testing for vibration isolation. Light is transmitted from the light source through an optical fiber coupler via an optical fiber. The emitting end of the optical fiber is situated perpendicular to the top surface of one of the rotor's fins. As the fins traverse the

perpendicular light path, some of the light is reflected back into the optical fiber and back through the coupler to be picked up by the light meter via another optical fiber. The power signal from the light meter is then transmitted into the oscilloscope in order to determine the rotational frequency of the rotor. Using the optical apparatus, depicted in the schematic, rotational frequencies of up to 1 GHz can be accurately measured. Nitrogen gas from a supply tank is first fed through a high pressure regulator and then through a low pressure regulator in order to step down the supply pressure from approximately 20 MPa (3000 lb/in²) to as low as 1.3 kPa (0.2 lb/in²).

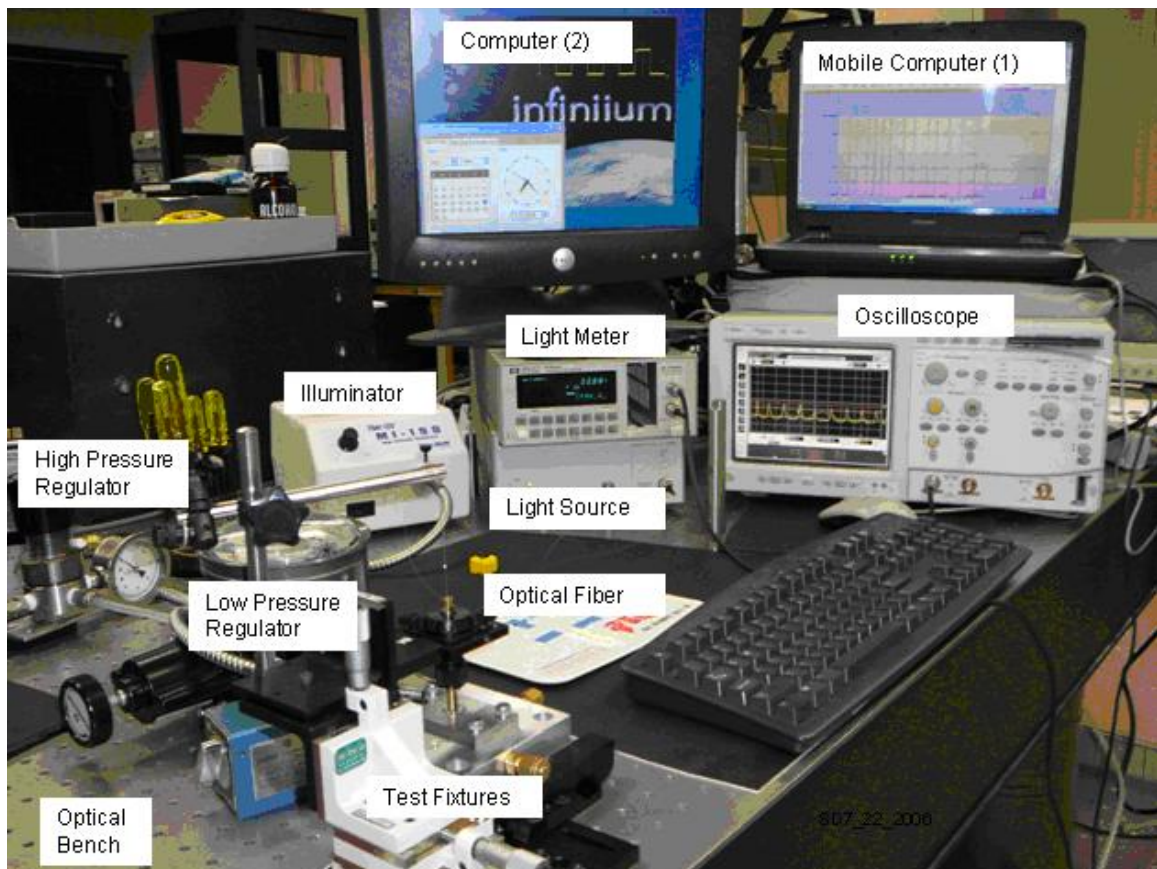


Figure 37: Photograph of Phase 1 experimental test setup.

The nitrogen gas flows through the rectangular channel, rotates the hub, and exits the channel at ambient pressure. All reported pressures in this work are gauge, relative to ambient (zero gauge) pressure.

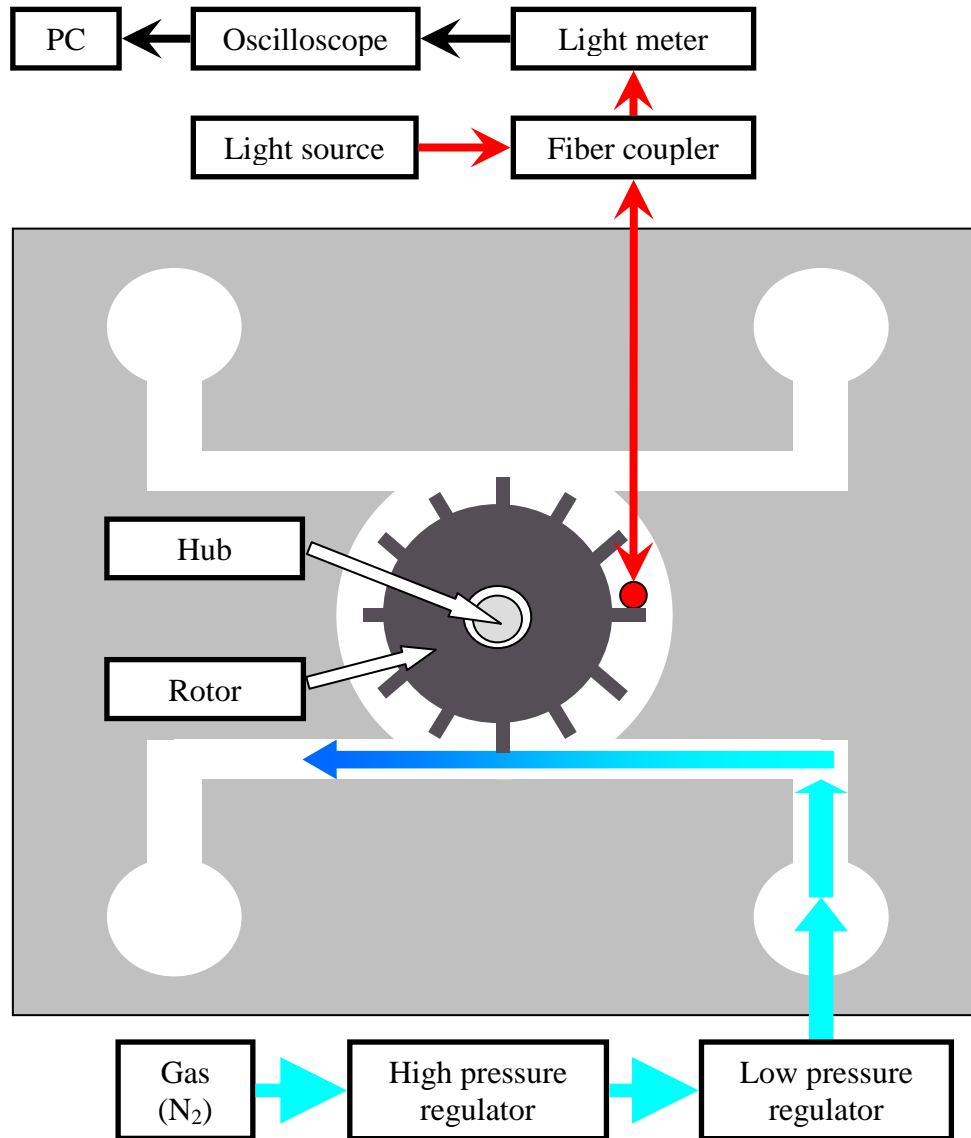


Figure 38: Top view schematic depicting Phase 1 optical speed measurement methodology.

In order to image the microbearing components, an optical microscope's image capture software is calibrated to a grating of known dimension. The top-side of the rotors and hubs are then imaged and relevant dimensions are obtained. The rotors are then turned over for back-side imaging and further measuring.

An exploded-view schematic and a photograph of the bearing test fixture are shown in Figure 39 and Figure 40, respectively. One set of the brass compression fitting gas feed connections is capped off as only a single jet of nitrogen is used here. As illustrated in Figure 39, four O-rings are first seated into the gas fixture counterbores. The microbearing system is then placed on top of the O-rings and covered by a 1 mm thick glass slide which is left in place during the periodic imaging between test runs, in order to prevent external debris from contaminating the assembly. Finally, a steel plate is placed on top of the glass slide and bolted to the fixture which compresses the O-rings and seals the fixture. A glass cover groove was precision ground into this steel top plate to ensure a 15 percent compression of the O-rings upon bolting. This geometric constraint (serving as a hard-stop for bolting), enabled by the groove, also mitigates hub cleavage concerns related to the unequal application of torque when fastening the top plate.

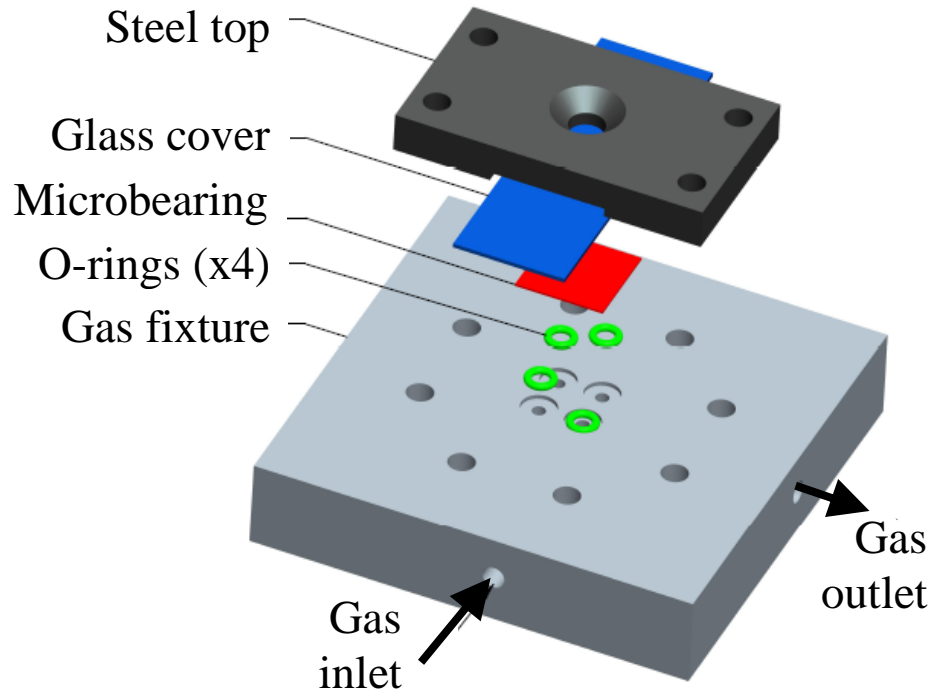


Figure 39: Exploded-view of Phase 1 microbearing test fixture.

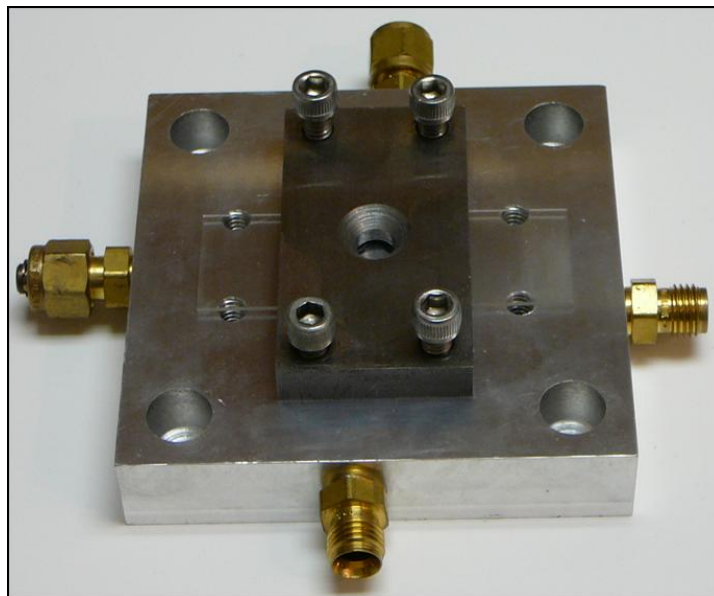


Figure 40: Photograph of Phase 1 microbearing test fixture. Connections on the tops and left are capped off.

3.1.2 Phase 1 Test Procedure

The DRIE fabrication process step produces a small axial taper on both hub and rotor surfaces. Since the rotors and hubs are fabricated separately, it is possible to test the assembled bearing system in so-called "conformal" and "non-conformal" configurations, as shown schematically in Figure 41. An x - y - z system frame is fixed to the hub with its origin at the hub center and with the x axis oriented parallel to the channel. Hub and rotor have lengths B and L and taper angles α_h and α_r , respectively, and the rotor is positioned at an axial distance δ relative to the top of the hub. The bearing surface is defined over the region $\delta \leq z \leq \delta + L$ and rotor axial translation δ can take on values between 0 and $B-L$.

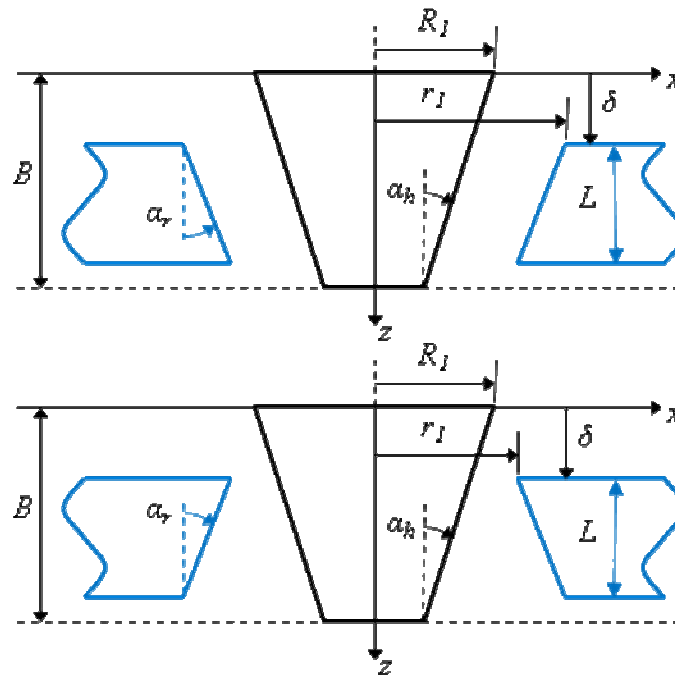


Figure 41: Conformal (top) and non-conformal (bottom) bearing configurations.

The rotor taper angle α_r is found from

$$\tan \alpha_r \approx \alpha_r = \frac{d_{\max} - d_{\min}}{2L} \quad (1)$$

where d_{\min} and d_{\max} refer to measured minimum and maximum rotor inner diameters, respectively. The hub taper angle α_h cannot be measured directly in a non-destructive manner, but it can be safely inferred to be of similar magnitude as that of the rotor since both rotor and hub employ the same DRIE fabrication process, and both were fabricated from wafers in the same batch run.

When the hub and rotor axes are coincident, and setting $\alpha_r \approx \alpha_h \equiv \alpha$, the bearing radial clearance C in the conformal configuration is uniform over the bearing surface and is given by

$$C = r_1 - R_1 + \alpha\delta \quad (2)$$

while in the non-conformal configuration, the bearing radial clearance varies linearly in the axial direction and is given by

$$C(z) = r_1 - R_1 + \alpha(2z - \delta) \quad (3)$$

with average value

$$\langle C \rangle = r_1 - R_1 + \alpha(\delta + L) \quad (4)$$

A total of six microbearing wear tests were conducted, with a sample size of three bearings each for conformal (C1-C3) and non-conformal (NC1-NC3) configurations. Table 2 lists the dimensional specifications for each of the six tests, with the intent of having similar average clearance values for all cases.

Table 2: Phase 1 bearing specifications.

Rotor length $L = 165 \mu\text{m}$

Hub length $B = 285 \mu\text{m}$

Test Case	R_l (μm)	r_l (μm)	α_r ($^\circ$)	$\langle C \rangle$ (μm) $\delta = 0$	$\langle C \rangle$ (μm) $\delta = B-L$
C1	197.0	202.9	1.5	5.9	9.1
C2	197.0	203.2	1.6	6.2	9.7
C3	197.0	202.0	1.2	5.0	7.6
NC1	197.0	198.5	1.4	5.5	8.4
NC2	197.0	198.5	1.3	5.3	8.1
NC3	197.0	198.5	1.2	5.0	7.5

The duty cycle employed for wear testing is summarized in Table 3. Each bearing wear test was initially run-in at 1.72 kPa (0.25 lb/in²) supply pressure for 15 minutes. The supply pressure was then set at 13.76 kPa (2 lb/in²), and the bearing system was run at this fixed supply pressure for a specified number of cycles. The supply pressure was incremented in 13.76 kPa intervals up to 68.80 kPa (10 lb/in²), and each bearing was run at the specified fixed supply pressure for a specific number of cycles for each interval. The cumulative number of cycles for each test (as well as the variability among all the tests) are also provided in Table 3. The variability in the number of cycles among all the tests is partially attributed to small changes in the measured rotor speed within a given interval.

Table 3: Phase 1 durability test procedure.

Supply pressure (kPa)	Cumulative rotor cycles (x 10 ⁶)
13.76	1.14 ± 0.03
27.52	1.89 ± 0.05
41.28	2.64 ± 0.07
55.04	3.39 ± 0.08
68.80	4.14 ± 0.10

3.1.3 Phase 1 Experimental Results

Figure 42 compares the progression of wear observed in a pair of tests representative of non-conformal (NC1) and non-conformal (C3) bearing configurations. The images are taken with an Olympus optical microscope at a common number of cumulative cycles. Focusing on the rotor surfaces, the optical microscope image sequence indicates that discernable wear starts in the conformal bearing at a much earlier time than that observed in the non-conformal bearing. Similar trends are observed with the remaining test cases. The wear behavior is essentially confined to the hub-rotor bearing interface, even after some of the rotor teeth have sheared off, as observed for the non-conformal bearing after 4,140,000 cycles.

An SEM is also used to periodically image the bearing components. Conventionally, SEM samples are adhered to sample holders via carbon matrix adhesive strips. The inevitable contamination and likelihood of cleavage upon attempting to dislodge bearing components for re-use renders this method infeasible. The aluminum fixture shown in Figure 43 was, therefore, developed to hold the hubs and rotors inside of the SEM for imaging. The fixture's corrugated compartments prevent the bearing components from falling inside the SEM vacuum chamber even if tilted to nearly 90 degrees. Once milled, these compartments were sand-blasted to eliminate burrs ensuring flush mating between the bearing components and fixture surfaces.

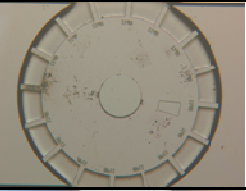
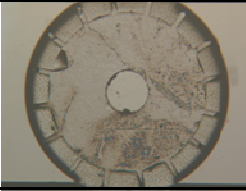
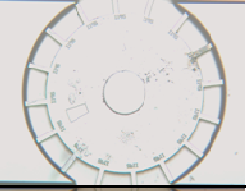
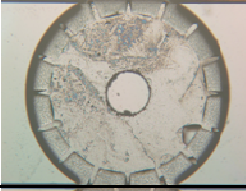
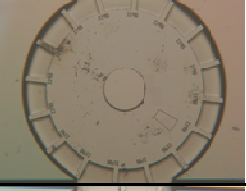

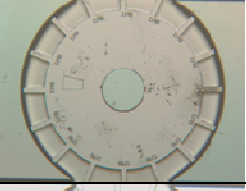

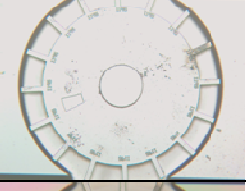

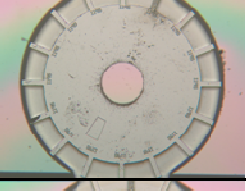

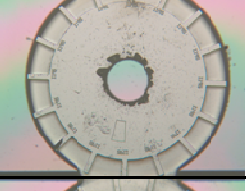
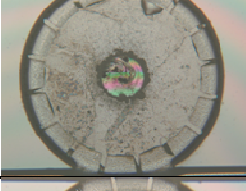
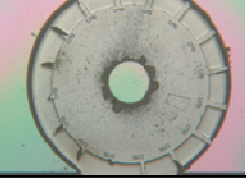
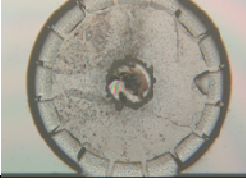
Cycles	NC1	C3
0		
390,000		
765,000		
1,140,000		
1,890,000		
2,640,000		
3,390,000		
4,140,000		

Figure 42: Phase 1 optical microscope image sequences comparison for non-conformal test case NC1 (left column) and conformal test case C3 (right column).

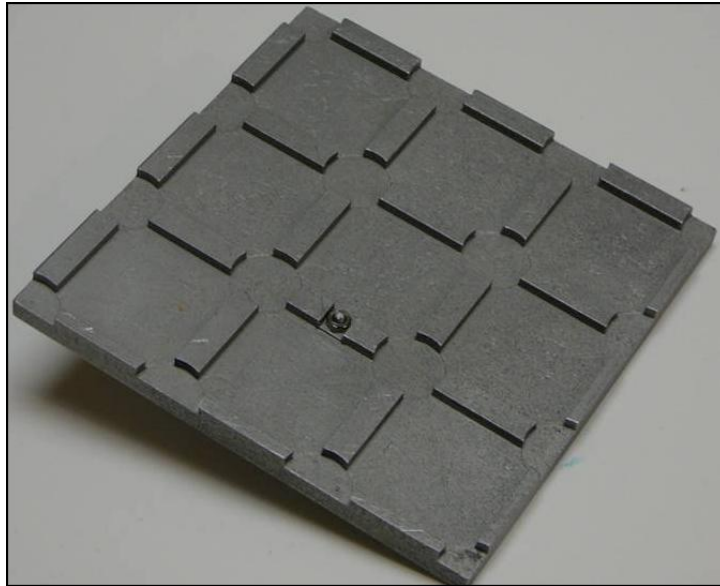


Figure 43: Aluminum SEM fixture used to hold hubs and rotors.

Figure 44 and Figure 45 show detailed SEM micrographs for the hub-rotor bearing interface corresponding to each of the non-conformal and conformal bearing tests, respectively. At the specified cumulative cycle, rotor and hub were disassembled, and the rotors were placed onto an aluminum holding fixture before insertion into the SEM. Observed white markings at zero cycles are due to small imperfections on the holding fixture and are not indicators of bearing wear. For the non-conformal configuration, negligible wear on either rotor or hub is observed in each of the three test cases NC1-NC3 through approximately 2×10^6 cycles. However, significantly more rotor surface wear is observed at 2×10^6 cycles for conformal test cases C1-C3, confined largely to the bearing surface edges.

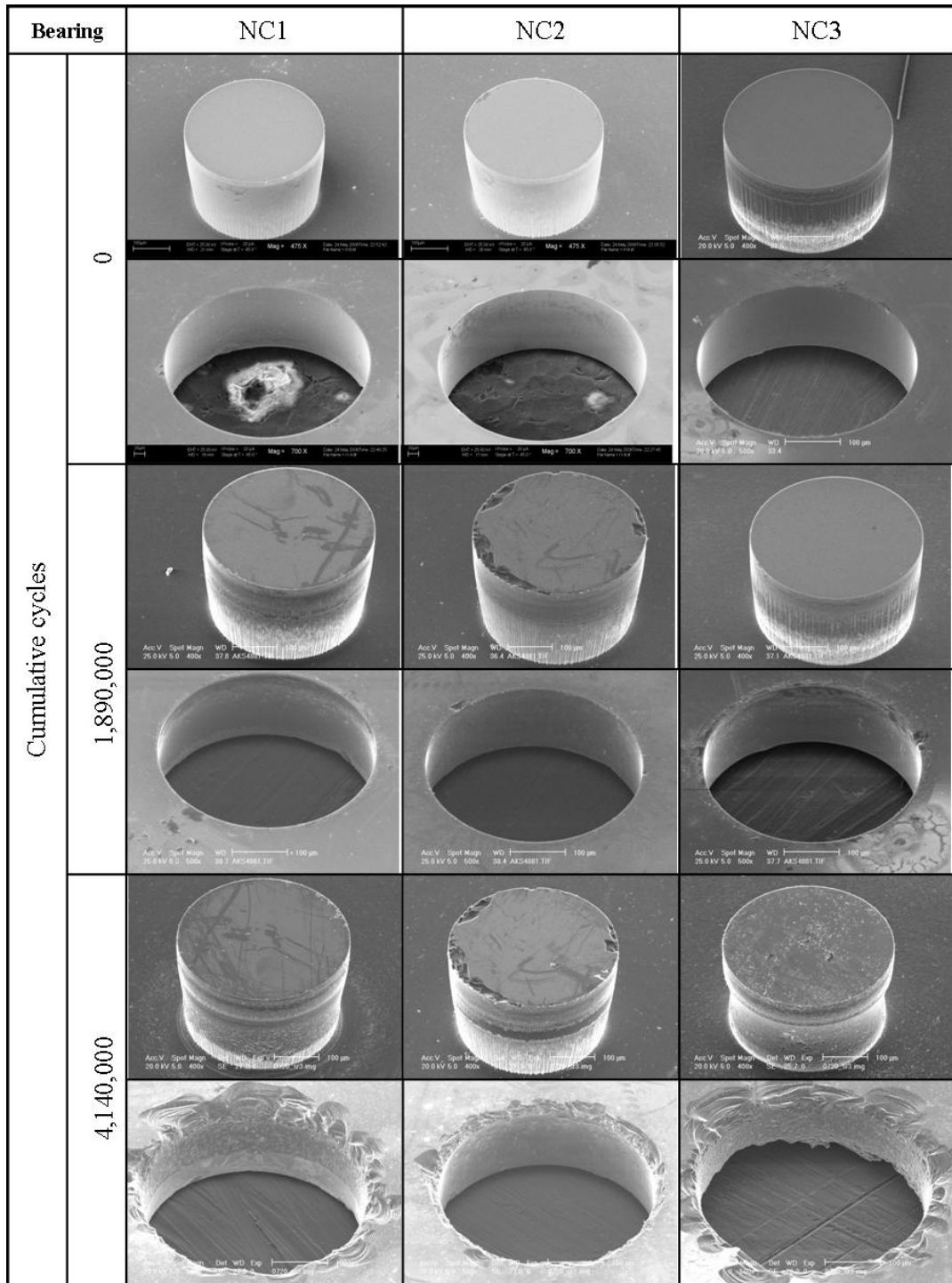


Figure 44: Phase 1 SEM micrographs of non-conformal hubs and corresponding rotors

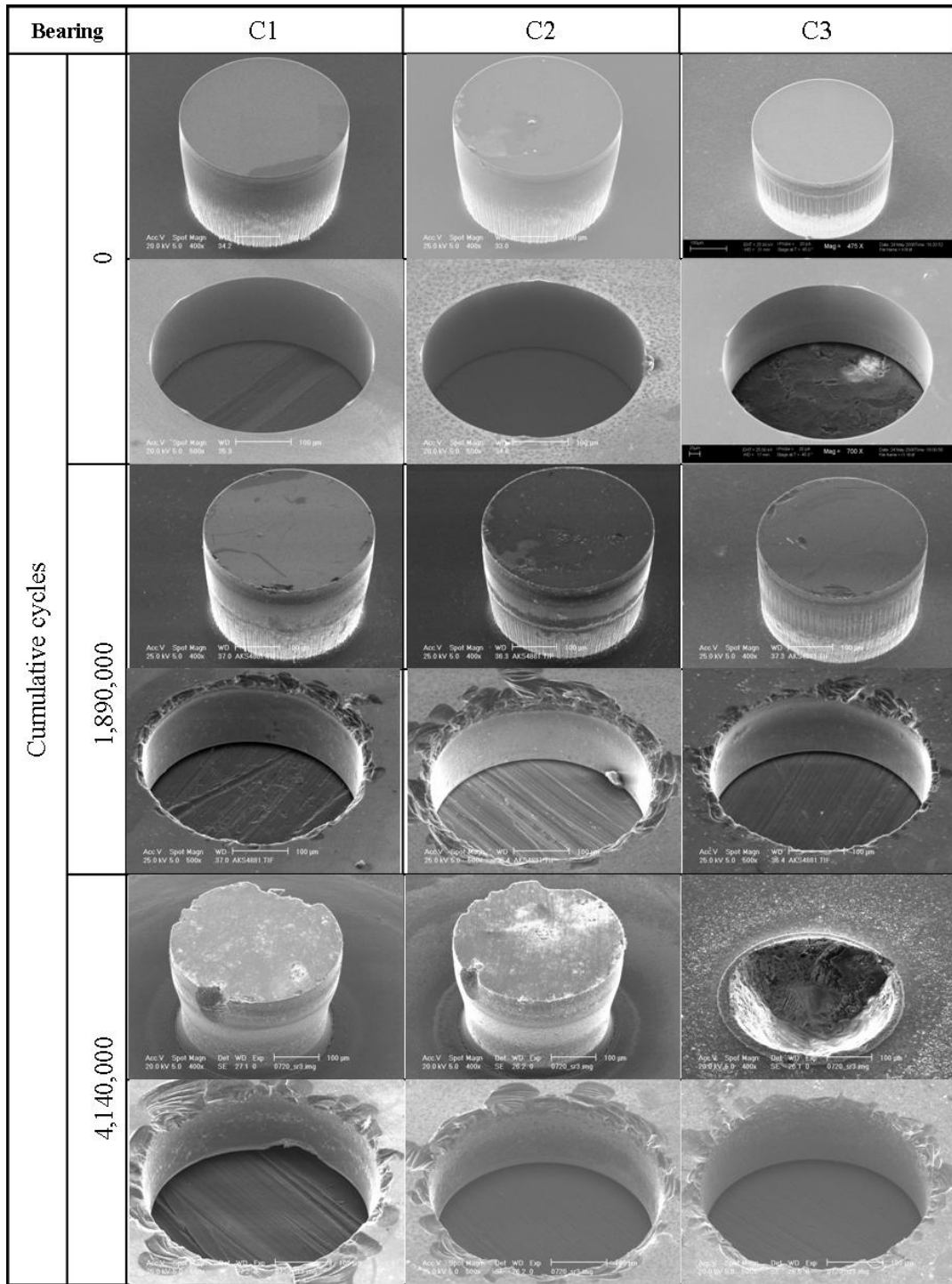


Figure 45: Phase 1 SEM micrographs of conformal hubs and corresponding rotors.

At approximately 4×10^6 cycles, non-conformal and conformal rotors have similar wear profiles, but serious undercutting and pitting is consistently observed on all conformal hubs. The extent of undercutting on hub C3 was so severe that it detached upon rotor disassembly prior to SEM imaging. Further inspection of SEM micrographs taken after 4,140,000 cycles indicates additional wear to the bottom surfaces of the conformal configuration hubs. With the exception of test case NC3, the non-conformal hubs have not yet taken wear profiles similar to those of their conformal counterparts, nor have their bases worn comparatively.

Although all bearings were imaged after undergoing an approximately equal number of cycles, Table 4 shows that the measured conformal bearing speeds were in general consistently greater up to 41.28 kPa (6 lb/in²) supply pressure. This speed trend changed at 55.04 kPa (8 lb/in²) supply pressure presumably due to the wear-induced change in bearing clearance profile.

Table 4: Phase 1 average rotational speeds (RPM) at specified supply pressures.

Supply pressure (kPa)	1.72	13.76	27.52	41.28	55.04	68.80
C1	2715	11412	17963	27778	35086	41921
C2	2679	11543	19602	29573	38344	40758
C3	2199	7981	16132	23807	22321	29558
NC1	1053	6272	11988	14971	18581	39113
NC2	1085	6513	12981	18055	22581	23292
NC3	1403	5421	11992	17606	37500	51398

The wear morphology of the rotor surface for test case C3 at 1,890,000 cycles is shown in Figure 46, where significantly large micron-scale non-spherical particles are found in addition to aggregates of near-spherical nanometer-scale particles. The striations on the worn areas are suggestive of material removal induced by impact. Neither large particles nor striations were observed in the Sandia microactuator systems, where adhesion appeared to be dominant wear mechanism [25, 46].

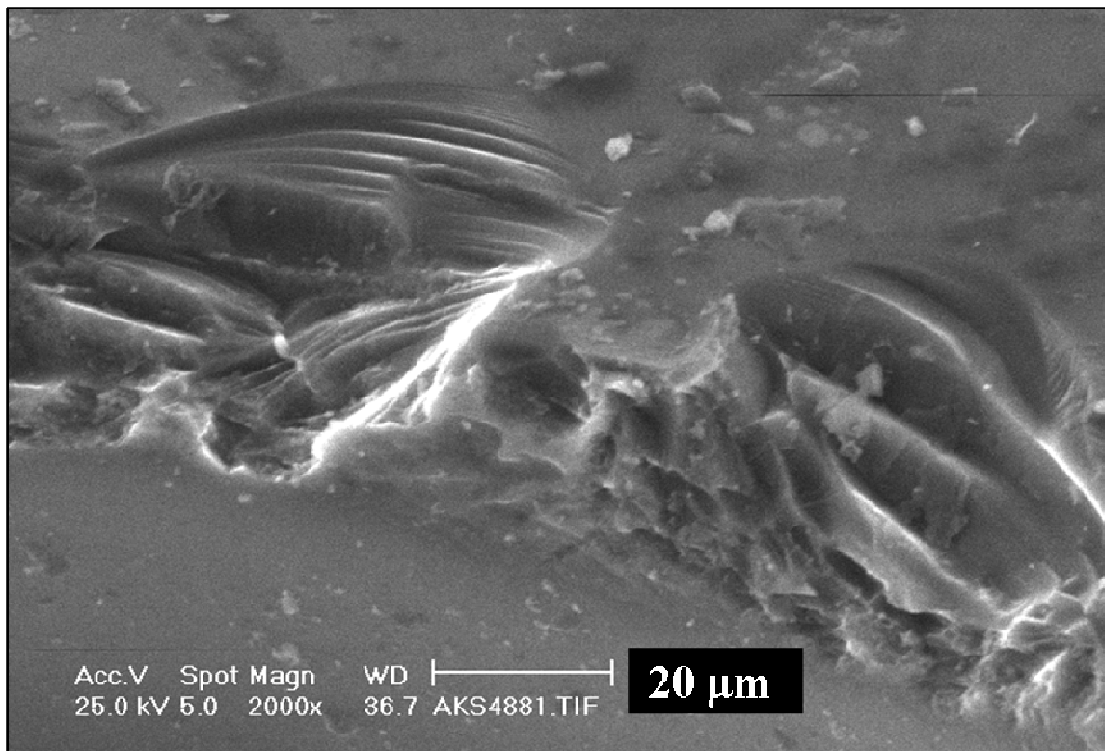
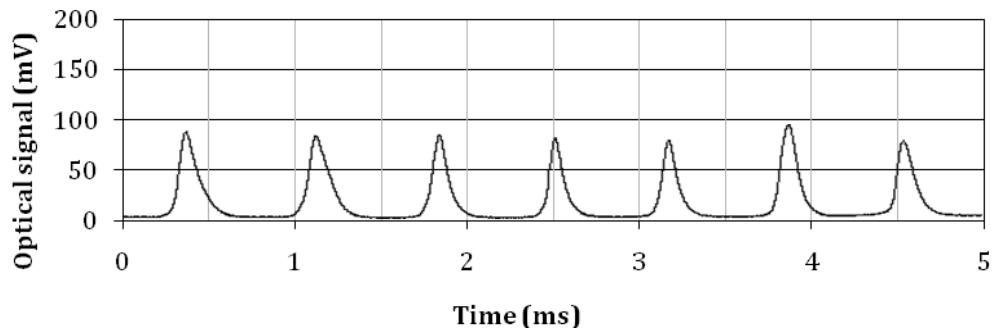
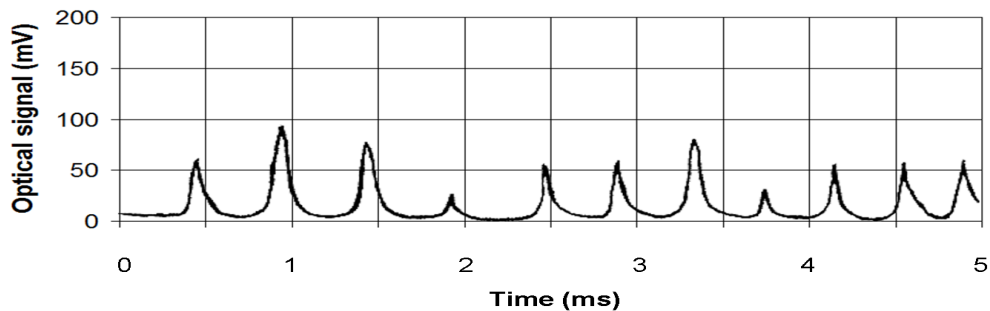


Figure 46: Wear morphology of rotor edge surface.

Figure 47 shows time histories of measured voltage representing the strength of the reflected optical signal for conformal and non-conformal bearing systems taken at a supply pressure of 13.76 kPa (2 lb/in²). Similar trends are observed at higher supply pressures. Voltage peaks indicate a hub fin passing under the optical signal, and the relative amplitude of the peaks provides an indication of rotor motion in the axial direction. The voltage peaks are noticeably more uniform for the non-conformal configuration, which when coupled with observed edge wear, indicates that the non-conformal bearing exhibits less out-of-plane rotor misalignment and/or translation when compared with its conformal counterpart.



(a) non-conformal case NC3



(b) conformal case C3

Figure 47: Phase 1 rotor speed waveforms at 13.76 kPa (2 lb/in²) supply pressure.

3.2 Phase 2 Testing

The primary intent of Phase 2 testing is to investigate clearance effects on the wear of microbearings. The following three sections present the test setup, test procedures, and experimental results.

3.2.1 Phase 2 Test Setup

A photograph and schematic of the Phase 2 experimental test setup are shown in Figure 48 and Figure 49, respectively. The methodology and apparatus for obtaining rotor rotational speed using an optical fiber setup follows closely to that described in Phase 1.

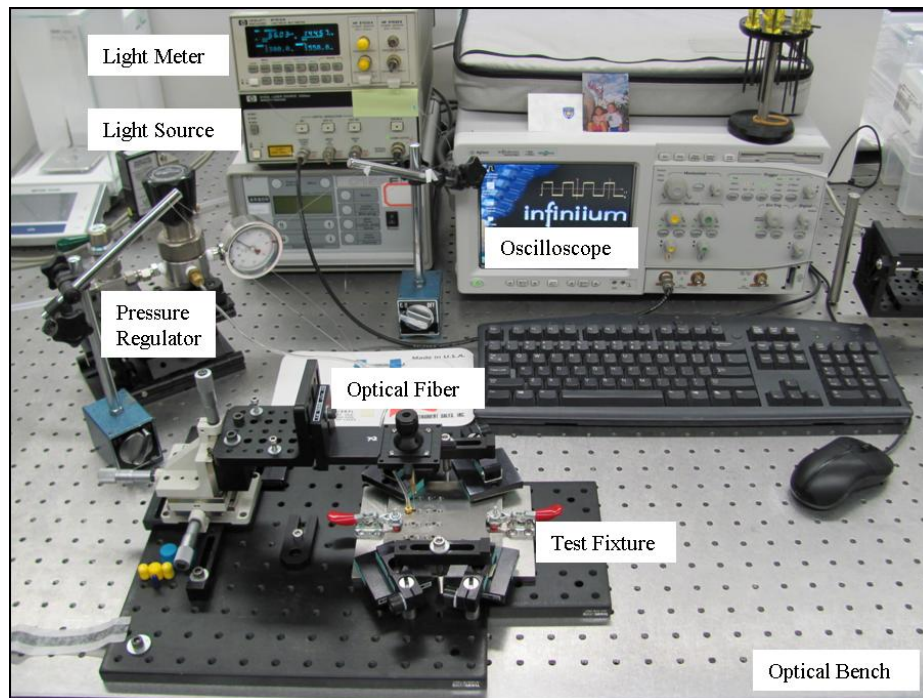


Figure 48: Photograph of Phase 2 experimental test setup.

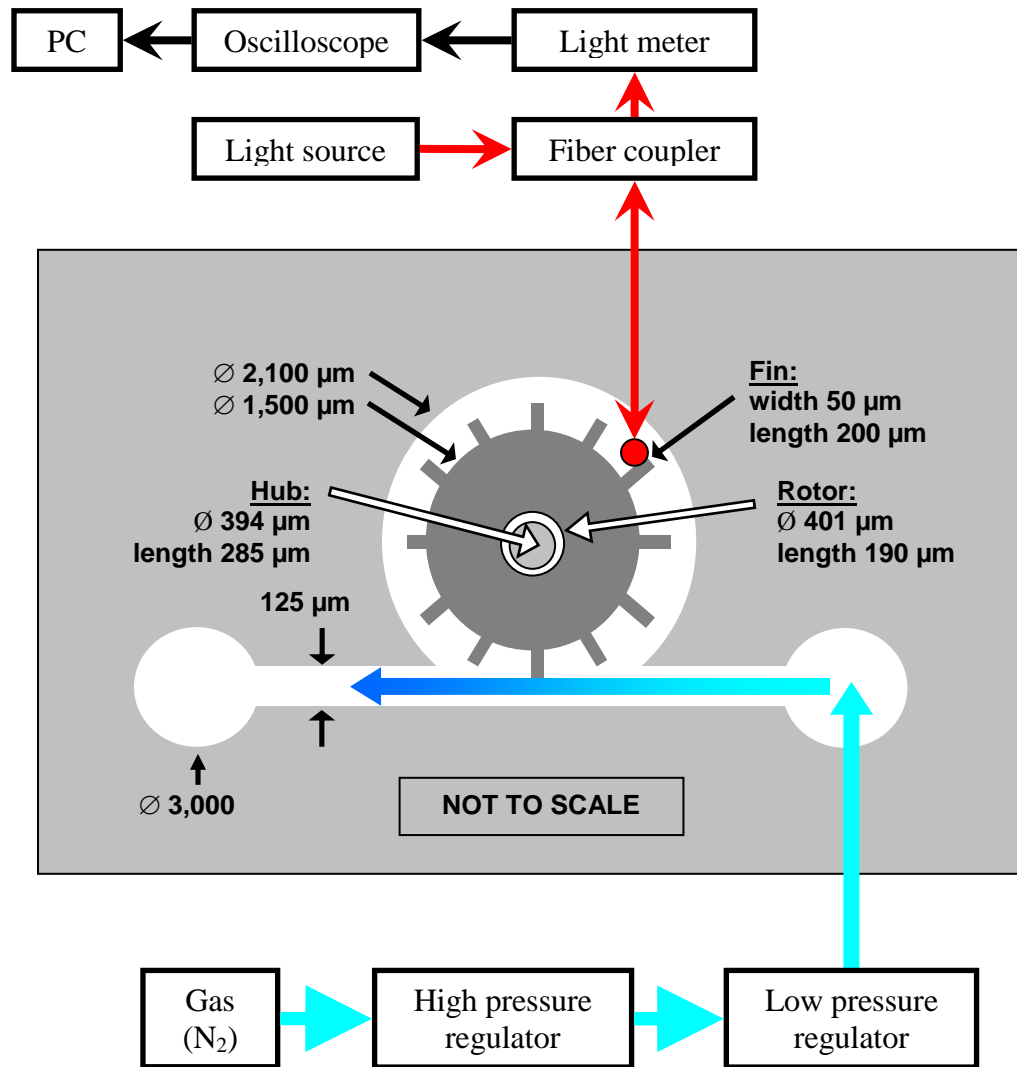


Figure 49: Top view schematic depicting optical speed measurement methodology for Phase 2 microbearings.

For this phase, a new bearing test fixture is developed to incorporate the entire hub wafer. An exploded-view schematic and a photograph of the Phase 2 microbearing test fixture are shown in Figure 50 and Figure 51, respectively. Once multiple test rotors are assembled to their respective hubs, the hub wafer is placed onto a precision ground 8 mm thick stainless steel base plate. A 1 mm thick polycarbonate plate (Appendix B.2) containing drilled nitrogen access holes is then aligned and clamped over the hub wafer. During test runs, this plate is left clamped in place during sequential optical imaging steps in order to prevent external debris from contaminating the assembly. Next, a 1 mm thick silicone sheet containing a similar array of nitrogen access holes is aligned over the polycarbonate sheet. An 8 mm thick precision ground steel top plate (Appendix B.3) with corresponding nitrogen access holes is then placed over of the silicone sheet and bolted to the fixture which compresses the silicone sheet and seals the fixture. Push-Quick (quick-release) gas feed connections, threaded into the top of this steel top plate, are employed for this phase; instead of the compression-type fittings used for Phase 1. The use of these fittings eliminates the potential for metallic debris, which may be generated from compression fitting components, to enter into the gas flow path after reconnection. In addition, the time required to connect/disconnect the tubing is reduced.

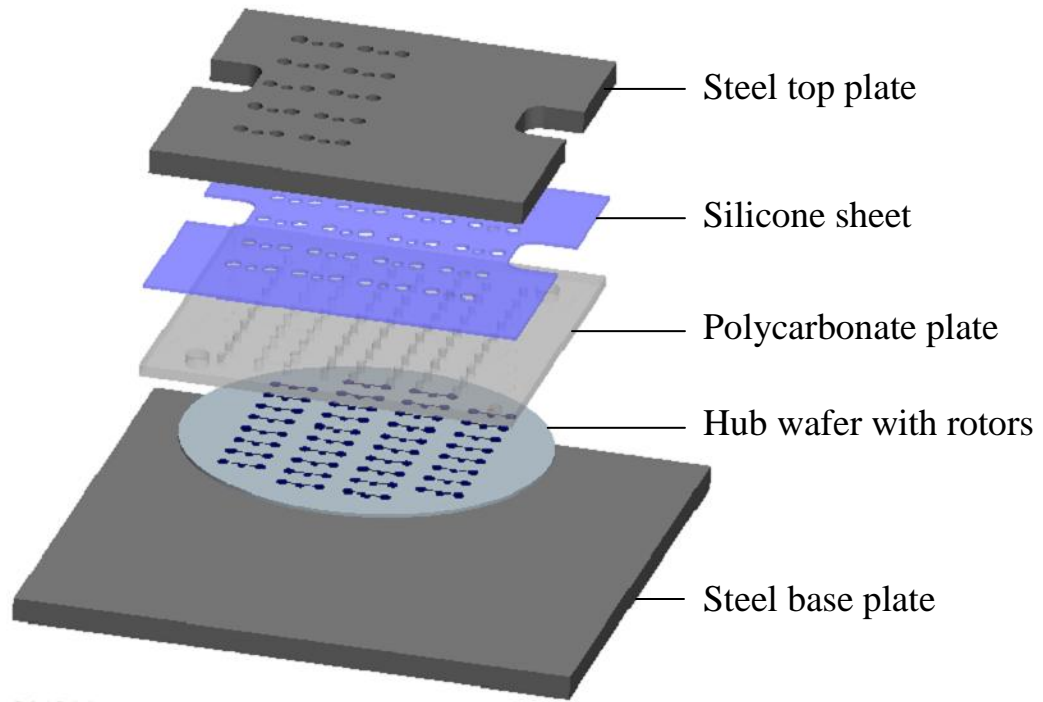


Figure 50: Exploded-view of Phase 2 microbearing test fixture.

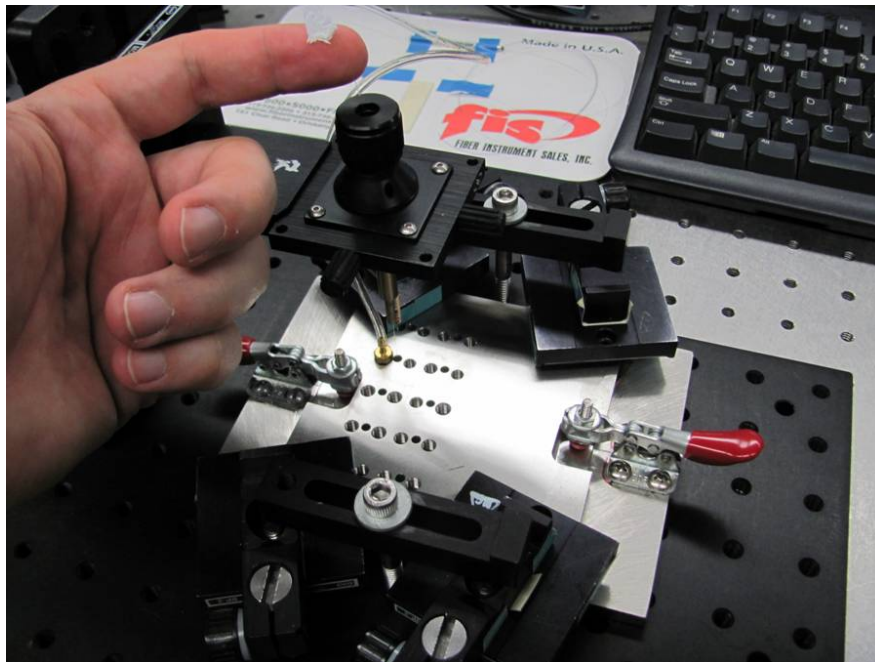


Figure 51: Photograph of Phase 2 microbearing test fixture.

3.2.2 Phase 2 Test Procedure

Figure 52 shows the geometry of the bearings in conformal and non-conformal configurations as defined previously in Phase 1 with the rotor concentrically positioned at its maximum axial position. Since the microbearing system is operated horizontally on the optical table, i.e., with its positive z -axis coincident with the direction of gravitational force, the rotor will have a tendency to be biased at maximum axial displacement. A radial clearance parameter C_0 is defined as

$$C_0 = r_1 - R_1 + \alpha(B - L) \quad (5)$$

where common axial taper α on rotor and hubs is a result of the DRIE etch process. In the non-conformal configuration, C_0 is the radial clearance at the top of the rotor, and in the conformal configuration, C_0 is constant over the entire clearance space. This radial clearance C_0 is the kinematic limit of rotor translation in the x - y plane provided rotor and hub are axially aligned with the rotor at maximum axial displacement.

A total of four tests, each with a different clearance, are presented for microbearings in conformal (C4 and C5) and non-conformal (NC4 and NC5) configurations. Clearance variation for both configurations is accomplished by assembling dimensionally similar rotors to hubs with varying diameters.

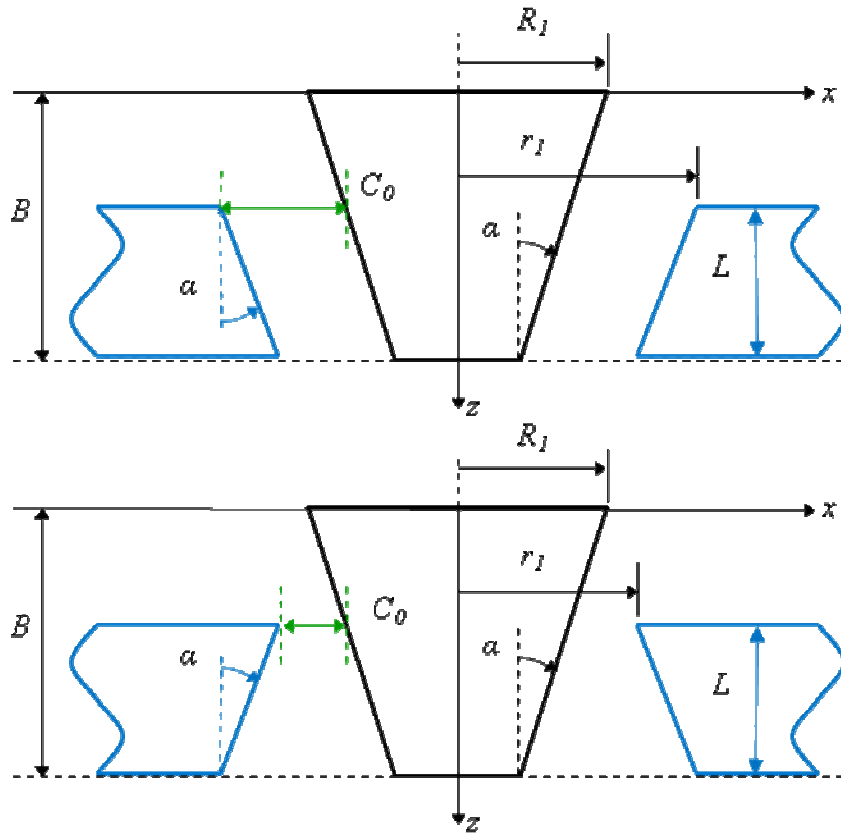


Figure 52: Radial clearance C_0 defined for conformal (top) and non-conformal (bottom) bearing configurations with rotor at maximum axial displacement.

Table 5 lists the dimensional specifications for each of the four tests, with the intent of having a similar mass specification for all rotors.

Table 5: Phase 2 bearing specifications.

Rotor length $L = 190 \mu\text{m}$

Hub length $B = 290 \mu\text{m}$

Test Case	R_l (μm)	r_1 (μm)	α_r (deg)	C_o (μm)
C5	195.8	202.8	1.28	9.2
C4	197.3	202.8	1.28	7.7
NC5	195.8	198.5	1.28	5.0
NC4	197.3	198.5	1.28	3.5

The duty cycle employed for Phase 2 wear testing is summarized in Table 6. Each bearing wear test was initially run-in at 6.88 kPa (1 lb/in²), 13.76 kPa, 27.52 kPa, and 55.04 kPa supply pressures for 2 minutes each. The supply pressure was then set at 68.80 kPa (10 lb/in²), and each bearing system was run at this fixed supply pressure for a specified number of cycles. The cumulative number of cycles for each test as well as the variability among all the tests are also provided in Table 6. The variability in the number of cycles among all the tests can be attributed to small changes in the measured rotor speed within a given interval.

Table 6: Phase 2 durability test procedure.

Supply pressure (kPa)	Cumulative rotor cycles (x 10 ⁶)
68.80	0.50 ± 0.01
68.80	1.00 ± 0.03
68.80	1.50 ± 0.04
68.80	2.00 ± 0.05
68.80	2.50 ± 0.06
68.80	3.00 ± 0.08
68.80	3.50 ± 0.09
68.80	4.00 ± 0.10
68.80	4.50 ± 0.11
68.80	5.00 ± 0.13

3.2.3 Phase 2 Experimental Results

Figure 53 compares the progression of wear observed for non-conformal bearings NC4 and NC5 with C_0 values of 3.5 μm and 5.0 μm , respectively. The images are taken with an Olympus optical microscope at a common number of cumulative cycles. Focusing on the rotor surfaces, the optical microscope image sequence indicates that discernable wear started in the bearing with larger C_0 at an earlier time than that observed in the bearing with smaller C_0 .

Figure 54 compares the progression of wear observed for conformal bearings C4 and C5 with C_0 values of 7.7 μm and 9.2 μm , respectively. Following a trend similar to that in the preceding case, this optical sequence indicates that discernable wear started in the bearing with larger C_0 at an earlier time than that observed in the bearing with smaller C_0 .

Figure 55 and Figure 56 show detailed SEM micrographs for the hub-rotor bearing interface corresponding to non-conformal and conformal bearing tests, respectively. At the specified cumulative cycle, rotors were disassembled and placed onto the bottom surfaces of the hub wafer gas feed holes. The entire wafer was then mounted to a standard fixture before insertion into the SEM. The most rotor surface wear is observed for test case C5, largely confined to the bearing surface edge. It should be noted here that SEM micrographs for test case NC4 at 5 million cycles do not exist as this test was halted after 2.5 million cycles due to handling damage.

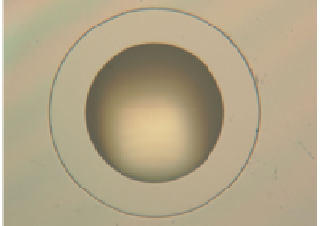

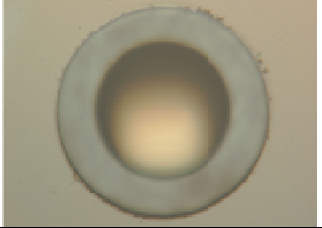
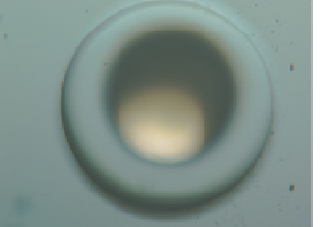
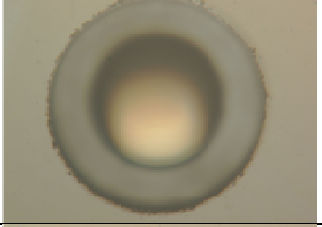
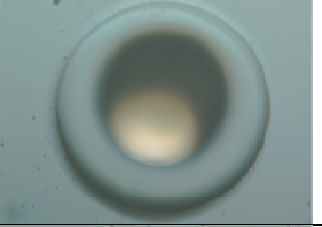
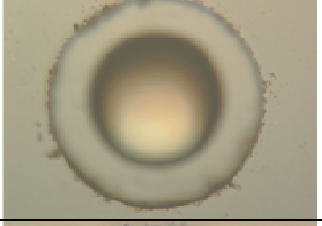
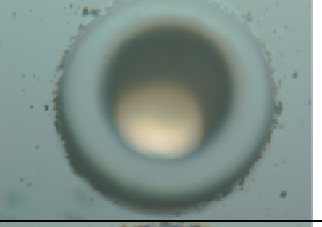
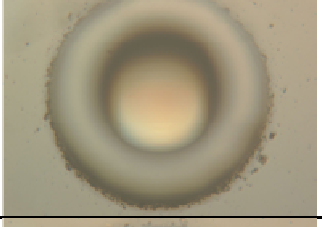
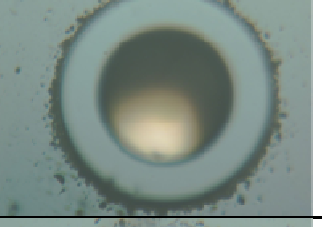
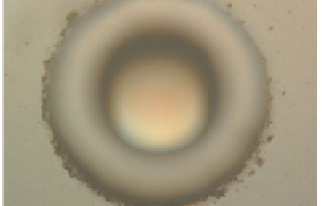
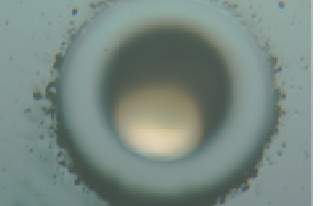
Cycles (Million)	NC4	NC5
0.0		
0.5		
1.0		
1.5		
2.0		
2.5		

Figure 53: Phase 2 optical microscope image sequences comparison for non-conformal bearing test cases NC4 (left column) and NC5 (right column).

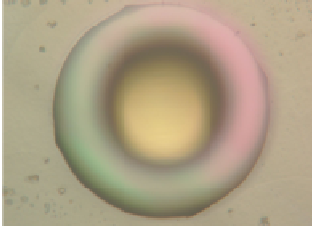
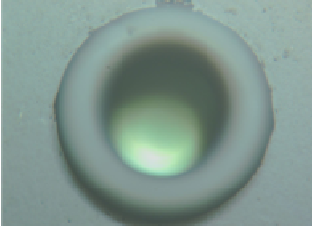
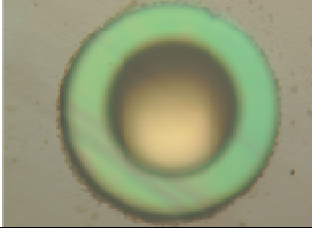
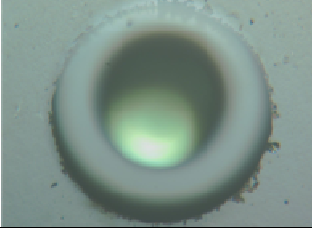

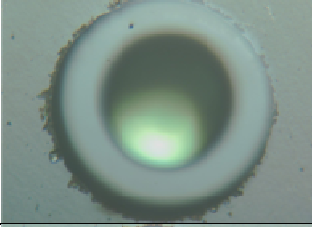
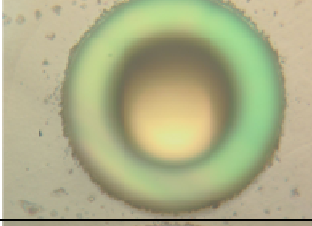
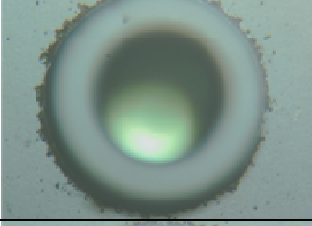
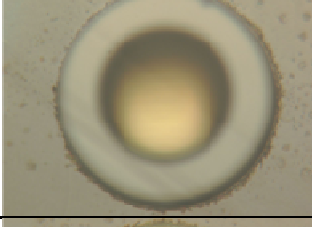
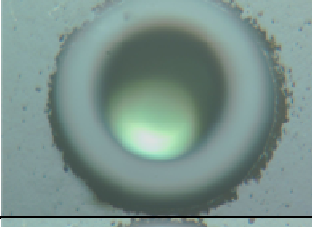
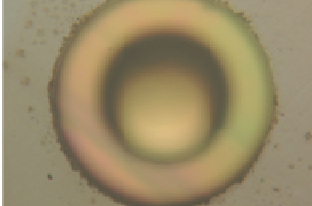
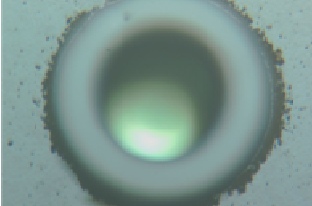
Cycles (Million)	C4	C5
0.0		
0.5		
1.0		
1.5		
2.0		
2.5		

Figure 54: Phase 2 optical microscope image sequences comparison for conformal bearing test cases C4 (left column) and C5 (right column).

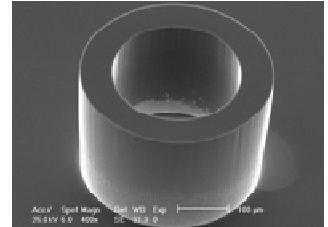
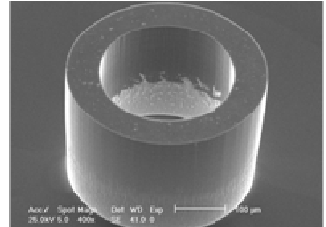
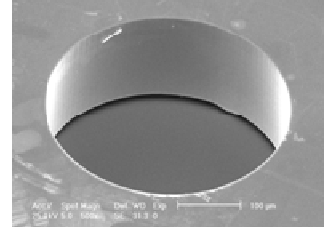
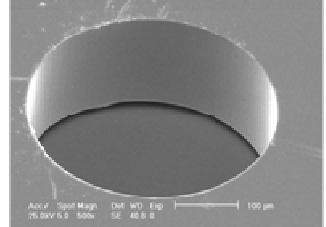
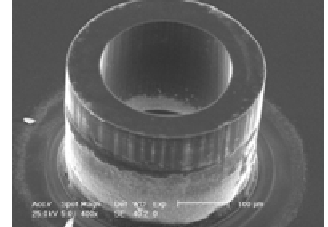
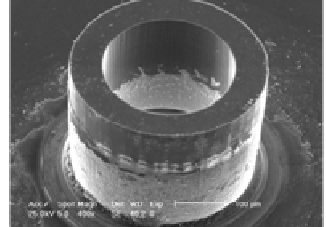
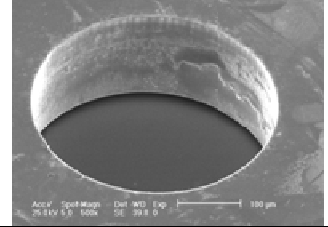
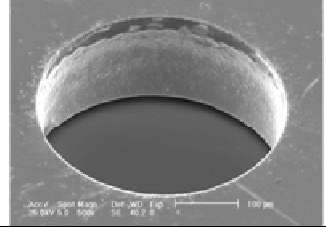

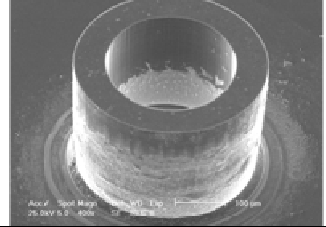
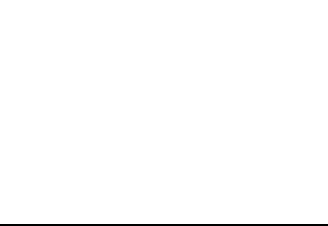
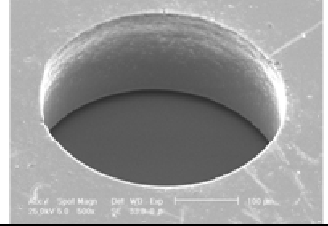
Cycles (Million)	NC4	NC5
0.0		
0.0		
2.5		
2.5		
5.0		
5.0		

Figure 55: Phase 2 SEM micrographs of non-conformal hubs and corresponding rotors for test cases NC4 and NC5.

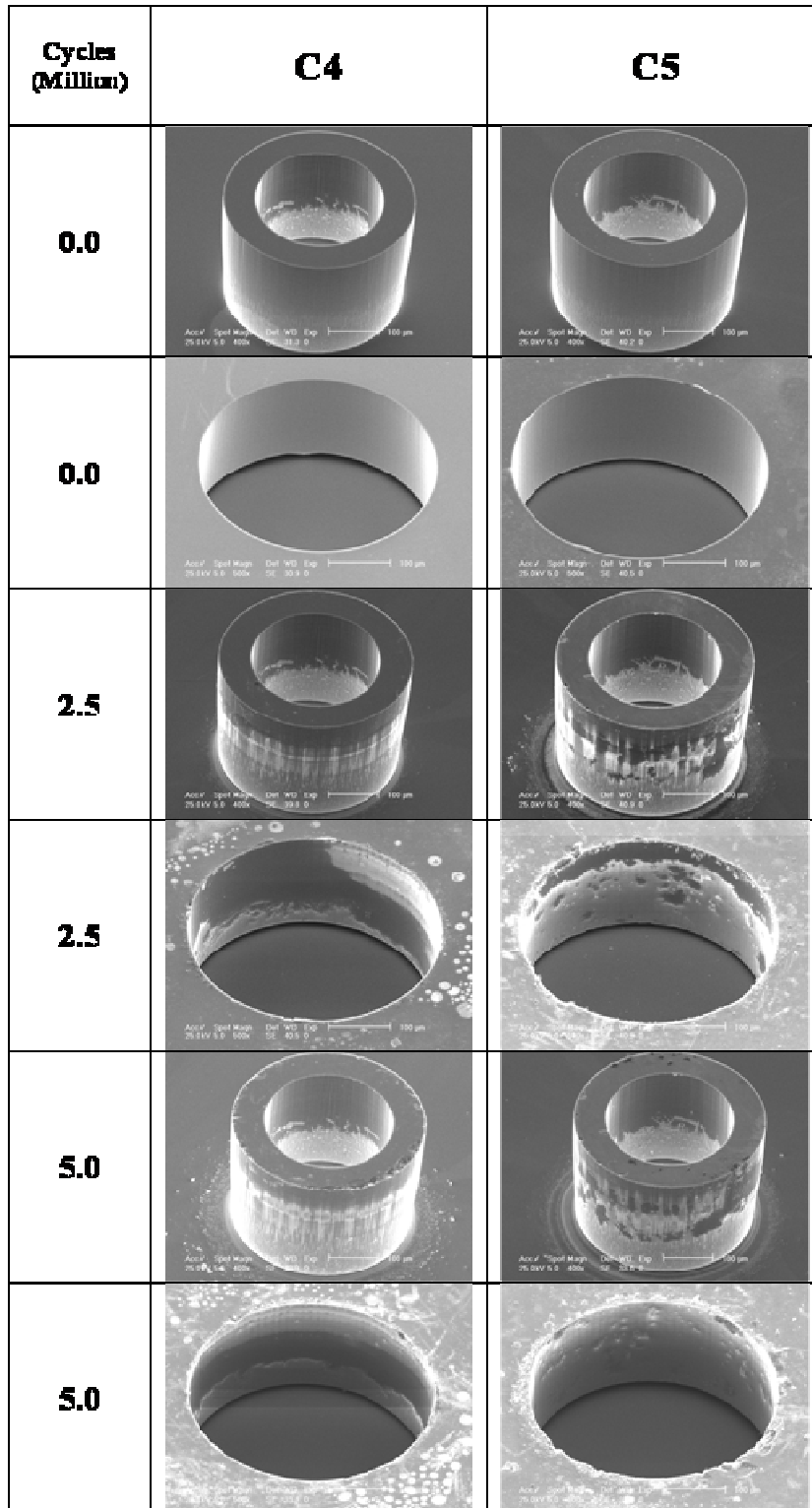


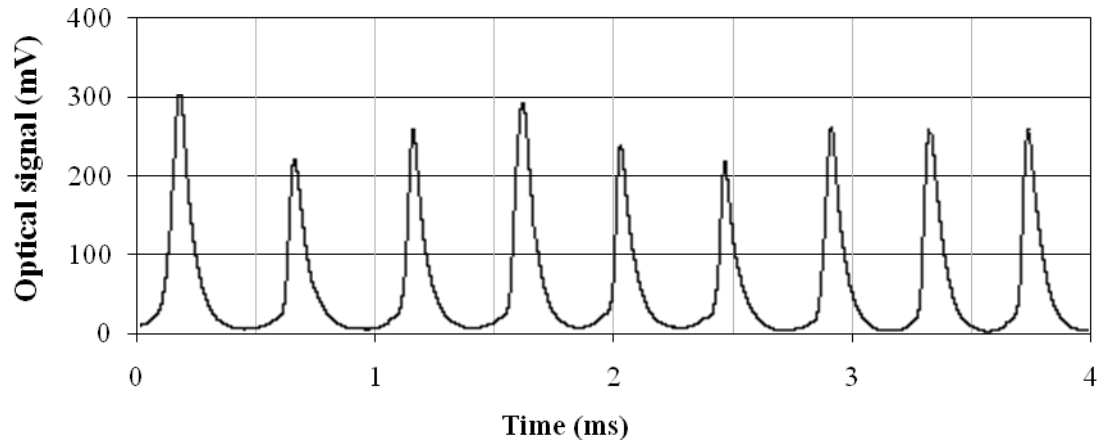
Figure 56: Phase 2 SEM micrographs of conformal hubs and corresponding rotors for test cases C4 and C5.

Although all bearings were imaged after undergoing an approximately equal number of cycles, Table 7 shows that the measured conformal bearing speeds were in general consistently greater.

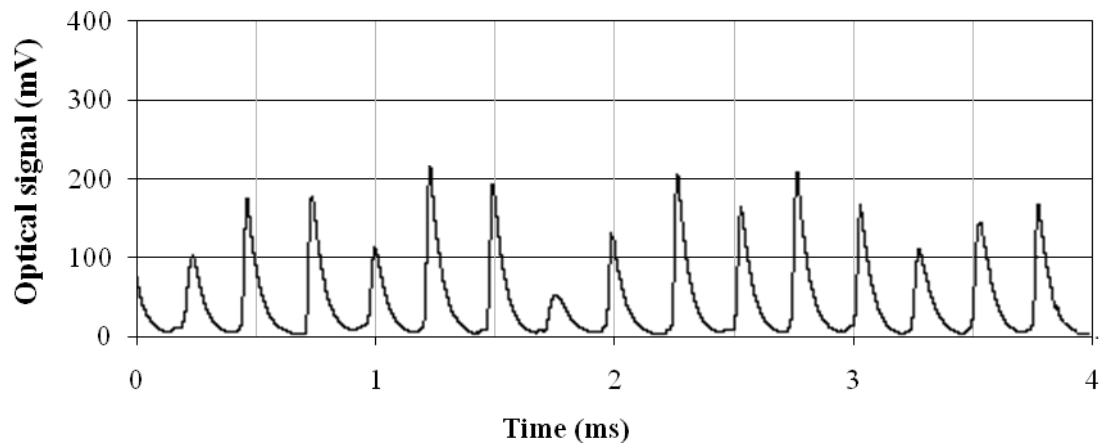
Table 7: Phase 2 rotational speeds (RPM) at specified cumulative rotor cycles.

Cumulative rotor cycles (x 10 ⁶)	0.5	1.0	1.5	2.0	2.5	3.0	3.5	4.0	4.5	5.0
C5	15719	16006	15813	15719	15813	15909	15625	15625	15719	15625
C4	14747	14665	14344	14665	14423	14503	14423	14266	14503	14266
NC5	10135	9795	9943	10096	9795	9868	9722	10096	9686	9686
NC4	8360	8281	8052	8052	8102					

Figure 57 shows time histories of measured voltage representing the strength of the reflected optical signal for conformal and non-conformal bearing systems taken at a gas supply (gauge) pressure of 68.80 kPa (10 lb/in²). Signal trends were similar to those obtained during Phase 1 testing. Voltage peaks indicate a hub fin passing under the optical signal, and the relative amplitude of the peaks provides an indication of rotor motion in the axial direction.



(a) non-conformal case NC4



(b) conformal case C4

Figure 57: Phase 2 rotor speed waveforms at 68.80 kPa (10 lb/in²) gas supply (gauge) pressure.

The voltage peaks are noticeably more uniform for the non-conformal configuration, which when coupled with observed edge wear, indicates that the non-conformal bearing likely exhibits less out-of-plane rotor misalignment and/or translation when compared with its conformal counterpart.

The wear morphology of the rotor surface for Phase 2 test case C5 at 5 million cycles is shown in Figure 58, where significantly large micron-scale non-spherical particles are found in addition to aggregates of near-spherical nanometer-scale particles. Similar to the observations made in Phase 1, the striations on the worn areas are suggestive of material removal induced by impact.

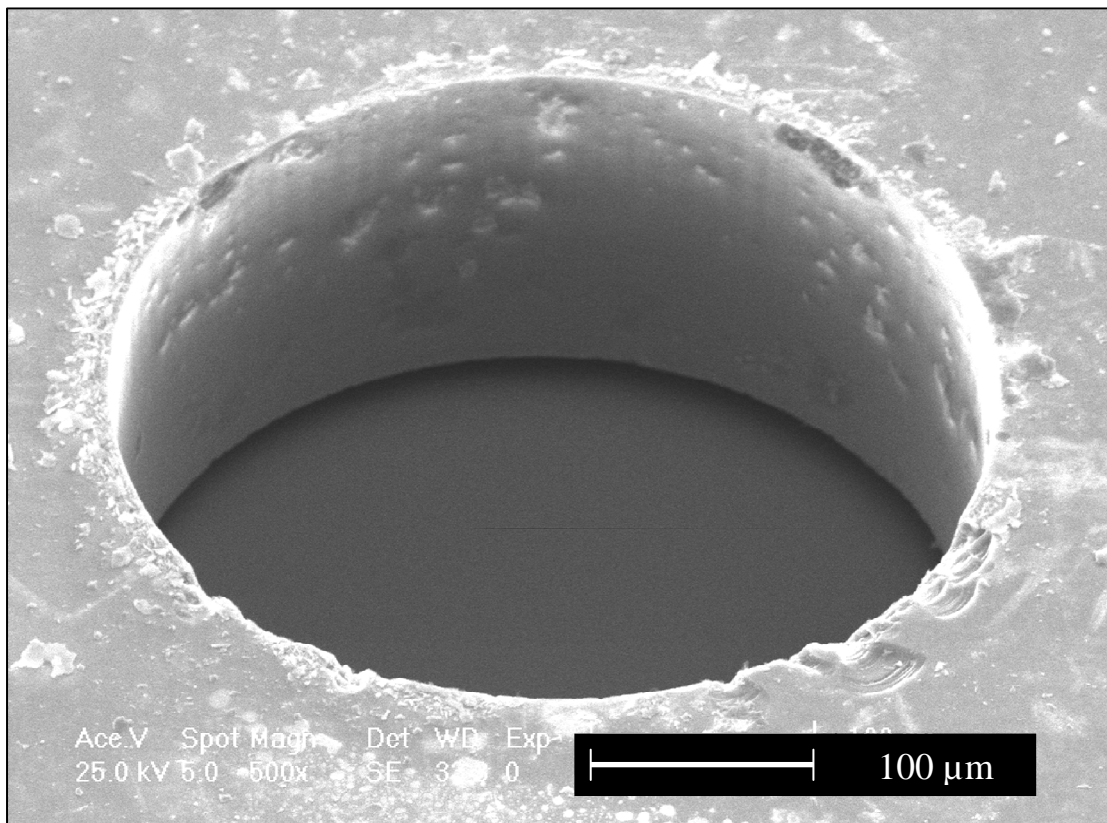


Figure 58: Wear morphology of rotor edge surface.

4 DISCUSSION

The following three sections of this chapter contain discussion on the experimental test results obtained for both the conformality (Phase 1) and the clearance (Phase 2) investigations. Section 4.1 presents the assessments of bearing loads, calculated using computational fluid dynamics (CFD). These bearing loads are then used in Section 4.2 to compare measured rotor wear to that predicted by an adhesion wear model. Finally, Section 4.3 contains discussion on a dynamic impact model, developed and implemented in a computer simulation program, in order to predict rotor speed and a coefficient of restitution value.

4.1 Bearing Load Assessment

As the channel flow impinges on the rotor teeth, a statically-equivalent radial load (in the system x - y plane of Figure 41) and torque (about the system z axis) is transmitted from the rotor to the hub bearing surface. Both load and moment are generally dynamic (time-dependent) due to fin pattern motion in the channel flow field combined with loads induced from rotor imbalance.

A first-order assessment of Phase 1 bearing load can be calculated from a representative CFD model shown in Figure 59 which corresponds to the instant when one of the hub teeth is normal to the channel flow. The model takes into account turbulence (via a standard k- ϵ model) and approximates the channel flow as two-dimensional parallel to the system x-y plane. No-slip impermeable boundary conditions are imposed on the channel walls, and velocity boundary conditions (in the system x-direction only) based on measured rotor speed are imposed on surfaces representing the moving fin and rotor outer diameter. The model employs four-noded isoparametric two-dimensional ANSYS FLOTRAN FLUID141 finite elements. Measured supply pressure and zero (ambient) pressure boundary conditions are applied to the model channel inlet and outlet, respectively.

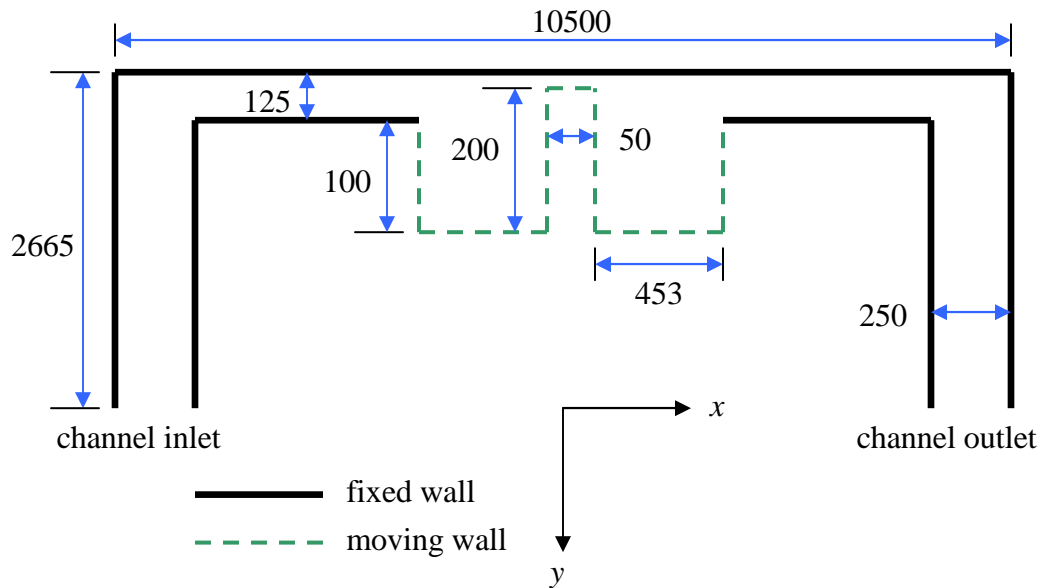
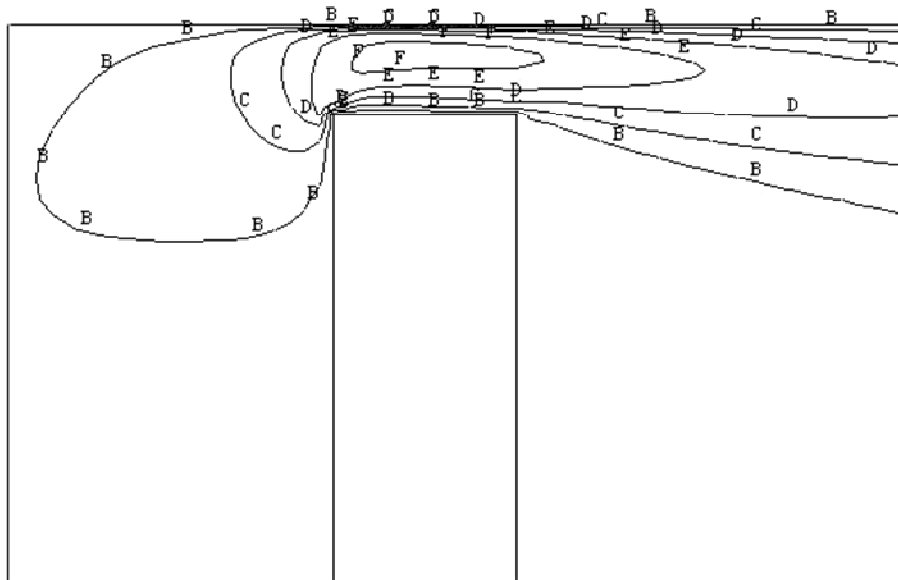
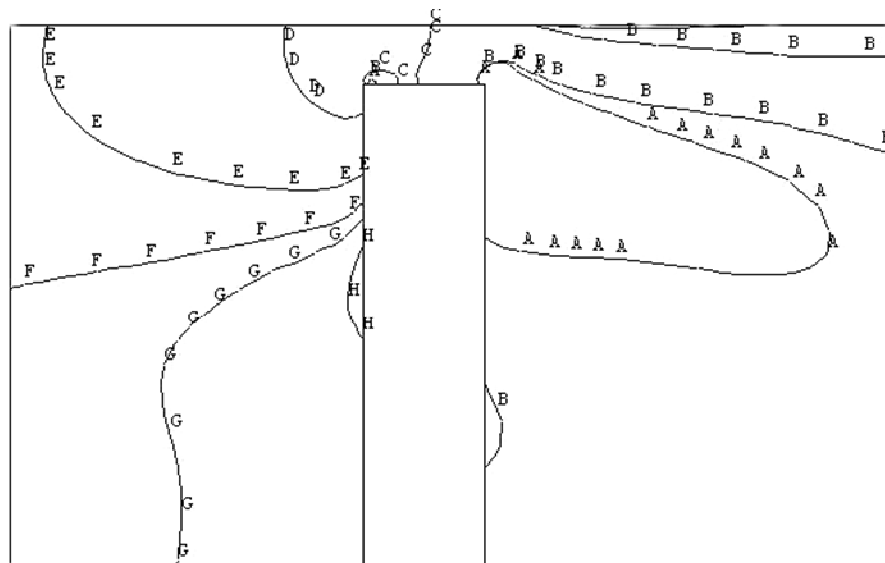


Figure 59: Phase 1 CFD model geometry (not to scale, dimensions in micrometers).

Figure 60 shows pressure and velocity fields corresponding to Phase1 test case C3 with 7981 RPM rotor speed and 13.76 kPa supply pressure [47]. A peak velocity magnitude of 107 m/s is observed in the region between the fin tip and the wall. Not shown are parabolic cross-channel velocity distributions obtained in the inlet and outlet channel regions far from the fin which agree with that obtained from classical laminar flow theory. Pressure distributions on leading and trailing fin faces are observed to be essentially uniform, except near the fin tip. Average leading and trailing face pressure values of 11400 and 1270 N/m², respectively, when integrated over the respective fin faces yield a resultant fin load of 334 μ N which is transmitted to the hub surface. Table 8 indicates that the fin load is essentially independent of rotor speed (as expected due to the relatively low fin linear velocity) and is nearly proportional to supply pressure for the case studies herein.



(a) velocity magnitude distribution (m/s)
(A=0, B=20, C=40, D=60, E=80, F=100)



(b) pressure distribution (N/m²)
(A=1340, B=1355, C=3000, D=11000, E=11650, F=11720, G=11740, H=11760)

Figure 60: Velocity magnitude and pressure distributions: Phase 1 test case C3 with 7981 RPM rotor speed and 13.76 kPa supply pressure.

Table 8: Phase 1 CFD model parameters.

Gas dynamic viscosity	$\eta = 17.5 \times 10^{-6}$	Pa-s
Gas density	$\rho = 1.185$	kg/m ³

Test case	Rotor speed (RPM)	Channel inlet pressure (kPa)	Rotor velocity V_x (m/s)	Resultant fin load F_x (μ N)
C3	7981	13.76	0.71	334
C3	16132	27.52	1.44	713
NC3	5421	13.76	0.48	341
NC3	11992	27.52	1.07	716

Substantial quantitative differences in the predicted peak velocity magnitude using a laminar flow model assumption are observed in the tip region (141 m/s) as well as possibly unrealistic sub-ambient pressures distributed on the trailing fin face. Pressure and velocity distributions (not shown) obtained in the inlet and outlet channel regions assuming laminar flow everywhere are quantitatively similar (as expected) to that obtained with a turbulent flow model. An average pressure value of 11570 N/m² on the leading fin face is obtained using laminar flow assumptions, and this value agrees reasonably well with that obtained with the turbulent flow model. Corresponding pressure and velocity distributions elsewhere in the fin region are also qualitatively

similar to those shown in Figure 60, and the resultant fin load of $398 \mu\text{N}$ does not differ much from that obtained using turbulent model assumptions. Evidently, turbulent flow effects as they pertain to the calculation of fin load can be ignored.

Employing the methodology described above, Phase 2 bearing load is calculated from a representative CFD model shown in Figure 61. The $125 \mu\text{m}$ channel width dimension remains the same as that of Phase 1, but the $7000 \mu\text{m}$ Phase 2 channel length is substantially shorter than that of Phase 1. In addition, only 12.5% ($25 \mu\text{m}$) of the Phase 2 rotor fin protrudes into the impinging gas channel flow, in contrast to the 50% ($100 \mu\text{m}$) Phase 1 rotor fin protrusion.

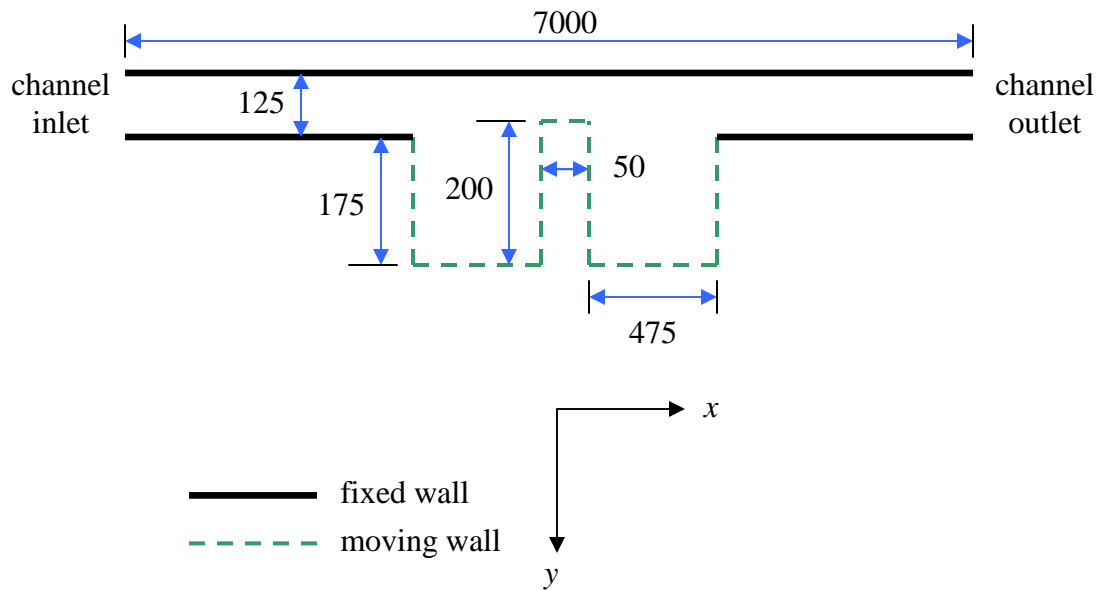
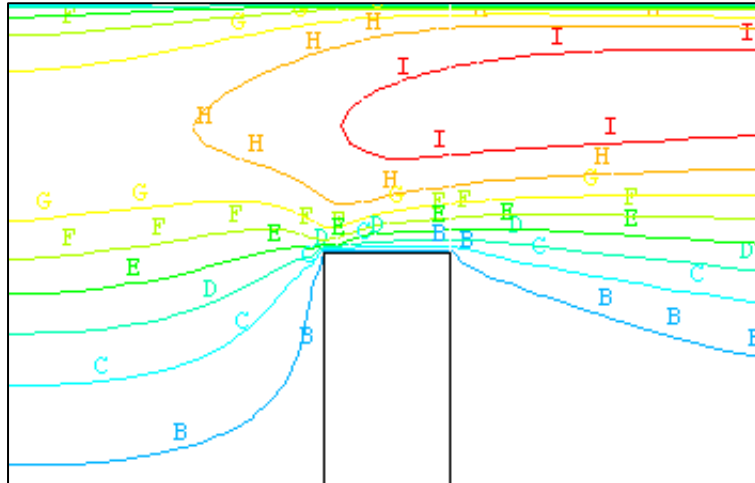
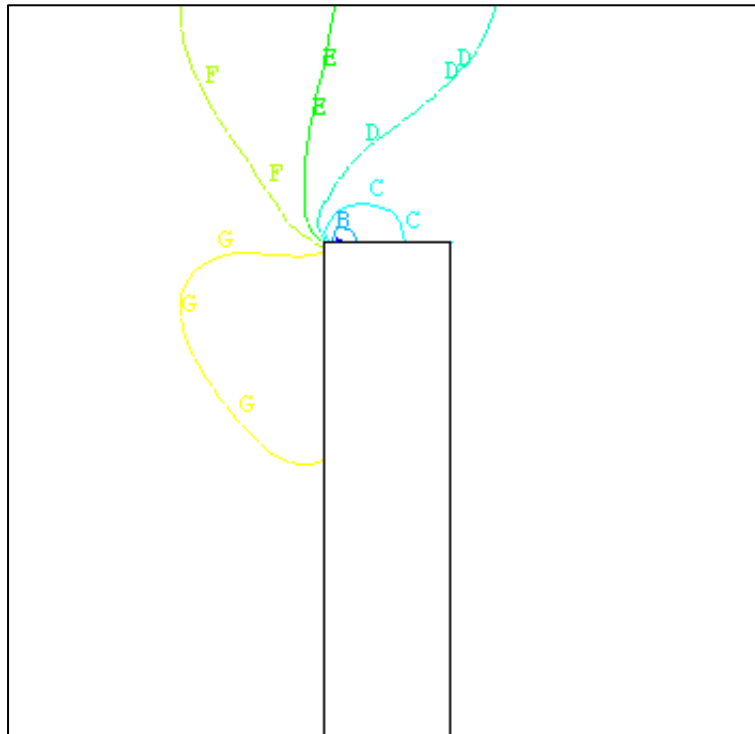


Figure 61: Phase 2 CFD model geometry (not to scale, dimensions in micrometers).

Figure 62 shows pressure and velocity fields corresponding to Phase 2 test case NC5 with 9882 RPM rotor speed and 68.80 kPa (10 lb/in²) gas supply (gage) pressure. A peak velocity magnitude of approximately 290 m/s is observed in the region between the fin tip and the wall. Pressure distributions on leading and trailing fin faces are observed to be essentially uniform, except near the fin tip. Average leading and trailing face pressure values of 51791 and 19692 N/m², respectively, when integrated over the respective fin faces yield a resultant fin load of 1159 μ N which is transmitted to the hub surface. As was the case in Phase 1, Table 9 confirms that the fin load is essentially independent of rotor speed (as expected due to the relatively low fin linear velocity).



(a) velocity magnitude distribution (m/s)
 (B=10, C=50, D=90, E=130, F=170, G=210, H=250, I=290)



(b) pressure distribution (N/m²)
 (B=7211, C=15423, D=23635, E=31347, F=40059, G=48270)

Figure 62: Velocity magnitude and pressure distributions: Phase 2 test case NC4 with 9882 RPM rotor speed and 68.80 kPa supply pressure.

Table 9: Phase 2 CFD model parameters.

Gas dynamic viscosity $\eta = 17.5 \times 10^{-6}$ Pa-s

Gas density $\rho = 1.185$ kg/m³

Test case	Rotor speed (RPM)	Channel inlet pressure (kPa)	Rotor velocity V_x (m/s)	Resultant fin load F_x (μ N)
C5	15757	68.80	1.40	1156
C4	14481	68.80	1.29	1156
NC5	9882	68.80	0.88	1159
NC4	8162	68.80	0.73	1142

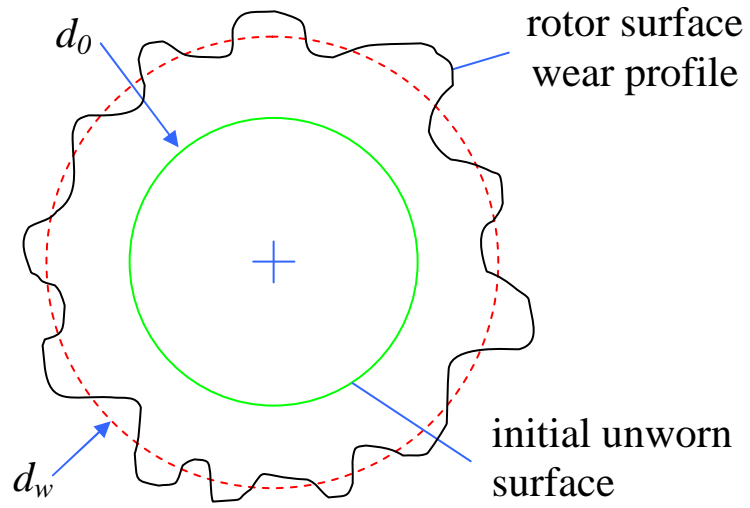
The resultant fin loads (bearing loads) are used in the following section to compare measured rotor wear to that predicted by an adhesion wear model. These bearing loads are also used subsequently in Section 4.3 in order to simulate rotor rotational speeds.

4.2 Wear Rate Determination

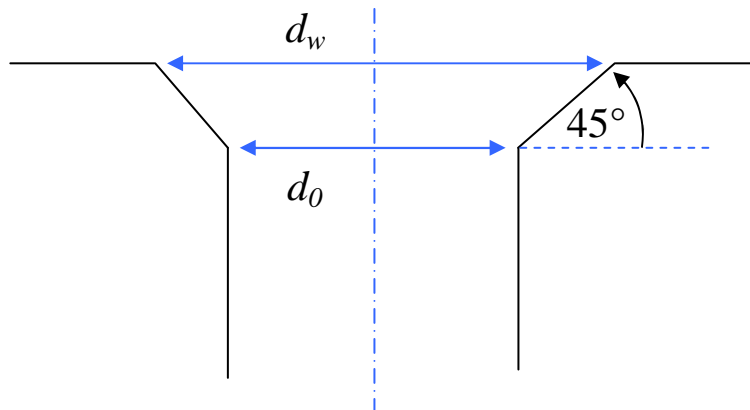
The Phase 1 rotor edge wear progression images shown in Figure 44 and Figure 45 take on a conically-shaped wear profile with a wear depth approximately equal to the change in rotor radius at the contact interface, as illustrated in Figure 63. The change in rotor diameter due to wear is calculated by constructing a circle of diameter d_w that captures in a least-squared sense the rotor surface wear damage pattern such as those shown in Figure 42. The rotor wear volume V accumulated after a specified number of rotor cycles is then estimated from the equation

$$V \approx \frac{\pi(d_w + d_o)(d_w - d_o)^2}{16} \quad (6)$$

where d_o is the initial unworn rotor diameter at the contact interface. The centers of the unworn and fitted circles do not necessarily coincide, but the difference is small and can be neglected.



(a) Regression fit of wear circle with diameter d_w .



(b) Conical edge wear geometry.

Figure 63: Phase 1 volumetric rotor wear assessment method: (a) regression fit of wear circle with diameter d_w ; (b) conical edge wear geometry.

Assuming an adhesion wear model, the predicted volumetric rotor wear V_{adh} can be estimated by the equation [48]

$$V_{adh} = \frac{KF_x L_s}{9\sigma_y} \quad (7)$$

where F_x is the bearing load, L_s is the length of the wear path, $\sigma_y = 7$ GPa is the yield stress of silicon [3], and $K = 4 \times 10^{-7}$ is the adhesion wear coefficient for ceramic-on-ceramic material due to the lack of published data for silicon [49]. The adhesion wear coefficient for polysilicon is also unavailable, but predicted wear using this adhesion wear model agreed well with wear trends obtained on the polysilicon-based Sandia microactuator systems for K values ranging between 1.1×10^{-7} to 5×10^{-7} [12, 25, and 46].

Figure 64 compares Phase 1 predicted and measured cumulative volumetric rotor wear for conformal and non-conformal configurations. Measured wear results at a given number of cycles are averaged over the representative data sets. The measured wear for the conformal configuration is consistently over an order of magnitude greater than that obtained with the non-conformal configuration, with the wear difference between the two configurations decreasing as both load and speed are increased.

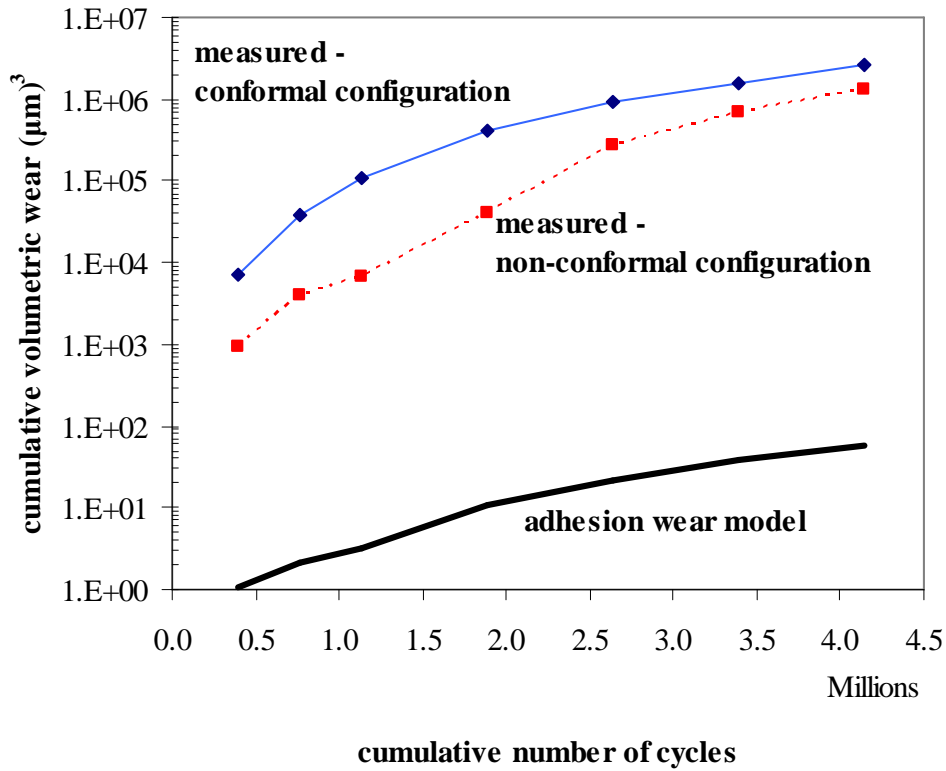


Figure 64: Phase 1 Comparison of measured and predicted volumetric wear due to adhesion.

As the Phase 2 rotor edges shown in Figure 55 and Figure 56 have not yet taken on conically-shaped wear profiles similar in magnitude to those in Phase 1, a new methodology, illustrated in Figure 65, is developed in order to quantify volumetric wear. The optical microscope images shown in Figure 53 and Figure 54 are processed into binary (black and white pixels) images similar to the schematic shown in the top of Figure 65. The rotor surface area covered by wear debris A_w is then calculated by counting the black pixels at each specified interval and subtracting the pixels

corresponding to zero rotations. The rotor wear volume V accumulated after a specified number of rotor cycles is then estimated from the equation

$$V \approx A_w t_w \quad (8)$$

where t_w is an assumed silicon wear particle size as depicted in Figure 65. Variably sized wear particles are generally stacked randomly and in multiple layers on a rotor surface.

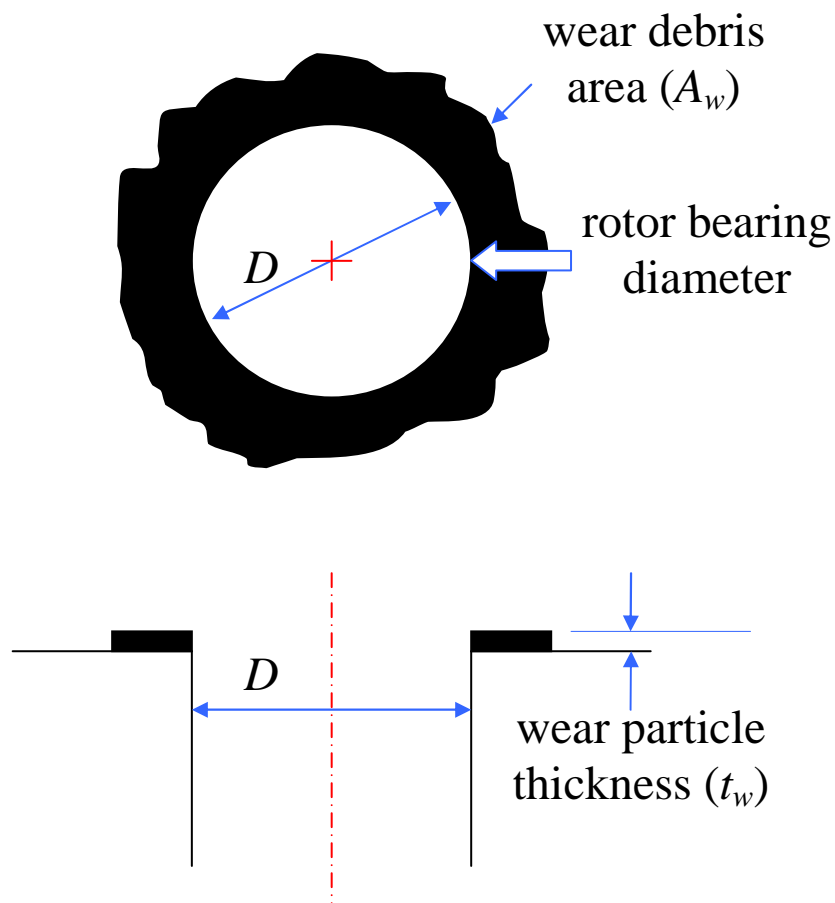


Figure 65: Phase 2 volumetric rotor wear assessment method. Schematic depicts aerial (top) and cross-sectional (bottom) views of silicon wear debris accumulated on rotor's top surface.

Figure 66 compares Phase 2 predicted and measured cumulative volumetric rotor wear for conformal (C4 and C5) and non-conformal (NC4 and NC5) configurations. For Phase 2 microbearings, it is observed that wear increases with progressively larger radial clearance values C_o , independent of non-conformal or conformal configuration.

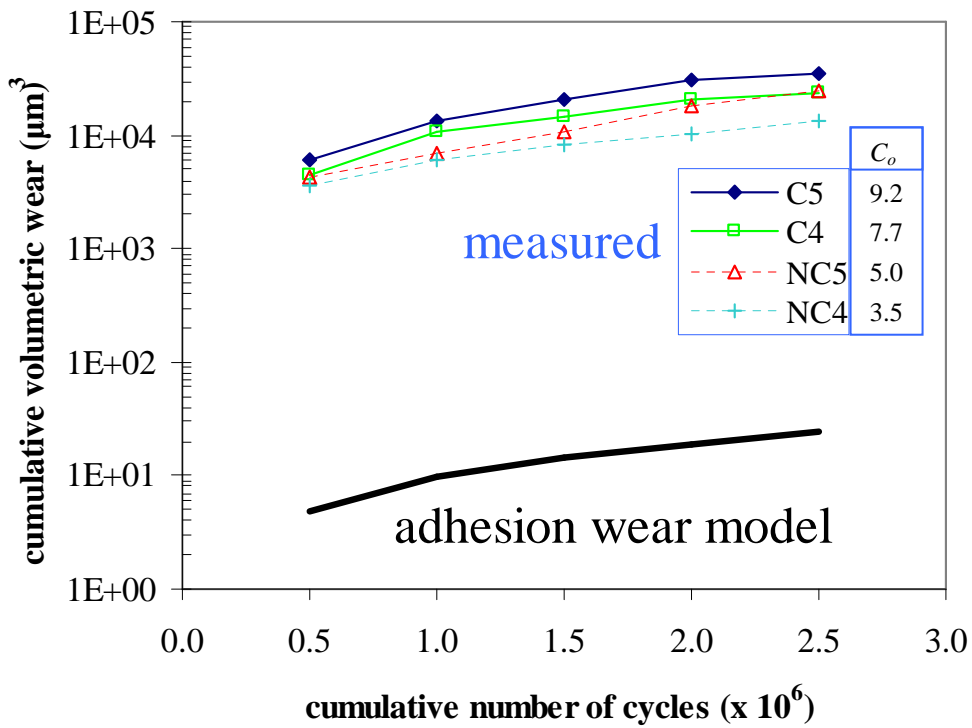


Figure 66: Phase 2 Comparison of measured and predicted volumetric wear due to adhesion.

A list of assumptions that are made in the calculation of Phase 2 measured volumetric follows

- first, although the silicon wear particles depicted in Figure 58 are observed to be up to tens of micrometers in size, a $1\ \mu\text{m}$ wear particle size t_w is assumed
- second, it is assumed that the wear debris area A_w shown in Figure 65 is composed of a single layer of wear particles
- third, some wear particles have fallen to the bottom of the hub as is evident from Figure 55 and Figure 56 and are thus missing from the wear progression images (Figure 53 and Figure 54) used for calculating the measured wear
- finally, it is plausible to assume that other wear particles have been transported out of view due to a combination of centripetal force and gas supply stream

Combined with the wear observations discussed previously, these assumptions ensure that the quantification of measured volumetric wear is conservative. While the Phase 2 calculated volumetric wear is up to two orders of magnitude smaller than that of Phase 1, the Phase 2 calculated wear is still over two orders of magnitude greater than that predicted by the adhesion wear model.

For all test cases (Phase1 and Phase 2), the predicted cumulative volumetric wear using an adhesion wear model is observed to be several orders of magnitude smaller than the measured results. Only one predicted curve for each phase is shown since both conformal and non-conformal configurations have very similar loads and very similar wear path lengths at a given supply pressure. The volumetric wear predicted by the adhesion wear model should be thus essentially independent of bearing geometrical configuration, which is obviously not the case. Although the adhesion wear coefficient for silicon-on-silicon is unavailable and adhesion wear coefficients for a given published material can vary widely, it would require that the K value for silicon-on-silicon have the unlikely characteristic of being several orders of magnitude larger than published representative materials. Combined with wear observations discussed previously, these calculations reinforce the suggested wear mechanism as impact. Impact wear was also considered the primary mode of failure for large-aspect ratio nickel microsleeve bearings of similar dimensional specifications to those reported here [32].

4.3 Bearing Speed Simulation

A dynamically-equivalent impact computational model of the bearing system is formulated and implemented in order to assess the effect of clearance on rotor speed and thereby wear of the microbearing. The bearing is modeled as an in-plane, 3 degree-of-freedom system in which the rotor can translate in the system x - y plane and rotate about axes parallel to the z axis while the sleeve is fixed. Impact between the rotor and sleeve is incorporated into the model by employing classical impact theory as described in reference [50].

Figure 67 depicts the representative geometry of the bearing system during momentary impact at point p , including relevant kinematic and dynamic parameters used to formulate the impact model. For illustrative purposes, the fixed hub is depicted by the large circle within which the rotor (small circle) rotates with an angular velocity of ω . A fixed rectilinear x - y computational coordinate frame originates at the center o of the hub. As the rotor translates, its center position or eccentricity e is calculated from

$$e = \sqrt{(e_x)^2 + (e_y)^2} \quad (9)$$

where e_x and e_y , represent eccentricity components in the computational frame.

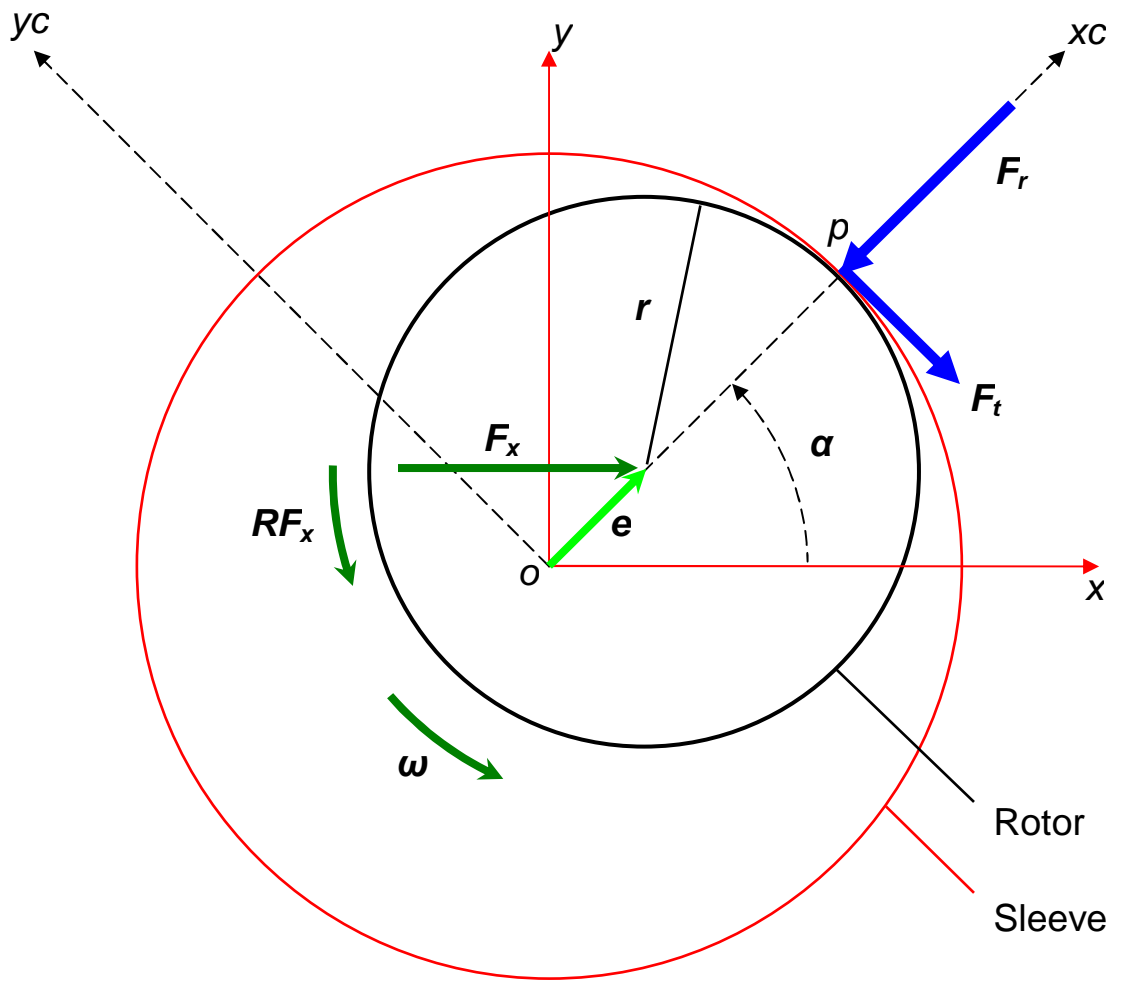


Figure 67: Schematic of impact model geometry (not to scale) depicts relative kinematic parameters during impact at point p .

Assuming the loading condition described in Section 4.1, i.e., a constant pressure-induced driving force F_x and given the initial state of the rotor (i.e., initial eccentricity components e_{xin} and e_{yin} ; velocity components v_{xin} and v_{yin} ; and angular velocity ω_{in}), subsequent states at any time t between intermittent rotor-hub impacts can be determined by calculating the following equations of motion:

$$e_x(t) = \frac{F_x}{2m} t^2 + v_{xin} t + e_{xin} \quad (10)$$

$$e_y(t) = v_{yin} t + e_{yin} \quad (11)$$

$$v_x(t) = \frac{F_x}{m} t + v_{xin} \quad (12)$$

$$v_y(t) = v_{yin} \quad (13)$$

$$\omega(t) = \frac{RF_x}{J} t + \omega_{in} \quad (14)$$

where m , r , and J represent the rotor's mass, radius, and mass moment of inertia, respectively. The moment arm R is the distance from the point of application of F_x (on the fin) to the rotor center. Equations (10) and (11) give the rotors eccentricity while equations (12) and (13) give its center's linear velocity components. Equation (14) gives the rotor angular velocity due to an applied torque RF_x about the z-axis.

Upon rotor-hub contact at point p , a rectilinear xc - yc contact coordinate frame, rotated by angle α , is instantaneously defined. In order to incorporate the radial F_r and tangential F_t components of the impact force into the model, equations

$$\cos \alpha = \frac{e_x}{e} \quad (15)$$

and

$$\sin \alpha = \frac{e_y}{e} \quad (16)$$

are used to transform the rotor center position and velocity components into the contact reference frame, yielding the following set of equations:

$$e_{xc} = e_x \cos \alpha + e_y \sin \alpha \quad (17)$$

$$e_{yc} = -e_x \sin \alpha + e_y \cos \alpha \quad (18)$$

$$v_{xc} = v_x \cos \alpha + v_y \sin \alpha \quad (19)$$

$$v_{yc} = -v_x \sin \alpha + v_y \cos \alpha \quad (20)$$

According to classical impact theory, the brief period of impact consists of two phases, deformation and restitution, separated by an instant in time when the normal relative velocity component of the colliding bodies at their point of contact becomes zero. The deformation phase starts at the time of initial contact t_0 and ends at the instant of maximum deformation t_1 while that of restitution starts from the maximum deformation condition and ends at the instant of separation t_2 . Employing this theory, the post-impact velocity components and angular velocity are determined with the aid of the following set of relations:

$$m[v_{xc}(t_1) - v_{xc}(t_0)] = -\int_{t_0}^{t_1} F_r(t) dt \quad (21)$$

$$m[v_{xc}(t_2) - v_{xc}(t_1)] = -\int_{t_1}^{t_2} F_r(t) dt \quad (22)$$

$$m[v_{yc}(t_2) - v_{yc}(t_0)] = -\int_{t_0}^{t_2} F_t(t) dt \quad (23)$$

$$J(\omega_2 - \omega_0) = -r \int_{t_0}^{t_2} F_t(t) dt \quad (24)$$

$$\beta = \frac{\int_{t_1}^{t_2} F_r(t) dt}{\int_{t_0}^{t_1} F_r(t) dt} \quad (25)$$

$$F_t = \mu F_r \quad (26)$$

Equations (21) and (22) express the rotor's change of linear momentum in the radial direction (x_c) while equation (23) expresses its change of linear momentum in the tangential direction (y_c). Equation (24) gives the change in angular momentum of the rotor. The coefficient of restitution β , expressed as the ratio of the impulse during restitution to the impulse during deformation, is defined by Equation (25). Equation (26) relates the impact force components via the kinetic coefficient of friction μ .

Using the relationships defined by Equations (21) - (26), post-impact velocities in the contact reference frame are determined in terms of μ and β using the following formulae:

$$v_{x_c}(t_2) = -\beta v_{x_c}(t_0) \quad (27)$$

$$v_{y_c}(t_2) = v_{y_c}(t_0) - \mu(1 + \beta)v_{x_c}(t_0) \quad (28)$$

$$\omega(t_2) = \omega(t_0) - \frac{m}{J} r \mu(1 + \beta)v_{x_c}(t_0) \quad (29)$$

For the simulation to progress until a steady state angular frequency is attained, the post-impact position is assumed be the same as that of pre-impact. In addition, the linear post-impact velocities, v_{xc} and v_{yc} must be transformed back into the computing reference frame using:

$$v_x = v_{xc} \cos \alpha - v_{yc} \sin \alpha \quad (30)$$

and

$$v_y = v_{xc} \sin \alpha + v_{yc} \cos \alpha \quad (31)$$

Table 10 lists the average rotor rotational speed model parameters for Phase 1 test cases NC3 and C3. The model assumes a constant dynamic coefficient of friction of 0.3, representative of silicon surfaces [26], constant radial load (in the x - y plane), constant torque (about the z axis), and an adjustable β value. The radial load and torque were determined from the CFD models in Section 4.1.

Table 10: Model parameters for Phase 1 test cases NC3 and C3.

Bearing Parameter	NC3	C3
C_0 (m)	4.0×10^{-6}	7.6×10^{-6}
μ	0.3	0.3
# of impacts	150	150
r (m)	200×10^{-6}	200×10^{-6}
R (m)	850×10^{-6}	850×10^{-6}
m (kg)	7.0×10^{-7}	7.0×10^{-7}
F_x (N)	341×10^{-6}	334×10^{-6}
e_{xin} (m)	0	0
e_{yin} (m)	0	0
v_{xin} (m/s)	0	0
v_{yin} (m/s)	0	0
ω_{in} (rad/s)	0	0

Each simulation assumed a β value, an initially concentric rotor and hub, and zero initial rotor angular velocity. Each simulation was run until the rotor reached a steady-state angular velocity. Table 11 contains the Phase 1 simulated average rotor rotational speeds after 150 impacts which is when steady-state speeds were reached.

Table 11: Simulated average rotor rotational speeds (RPM) for Phase 1 cases NC3 and C3.

Bearing \ β	0.25	0.30	0.35	0.40	0.45	0.50	0.55	0.60	0.65
C3	2883	3141	3450	3846	4408	5156	5880	6574	7788
NC3	2113	2303	2529	2819	3231	3780	4310	4819	5709

Figure 68 and Figure 69 illustrate the variation of simulated rotor rotational speeds with β for conformal and non-conformal configurations, respectively. Fixing bearing load, torque, and geometry, simulation trends indicate that an increase of β results in a corresponding increase in the steady-state rotor rotational speed. A larger β implies more elastically-induced impact separation of the rotor from the hub, thereby allowing more time for the rotor to accelerate between subsequent impacts. For a given β , an increase of C_0 also results in a predicted increase in steady-state rotor rotational speed. A larger clearance allows the rotor to accelerate for a longer period of time between ensuing impacts.

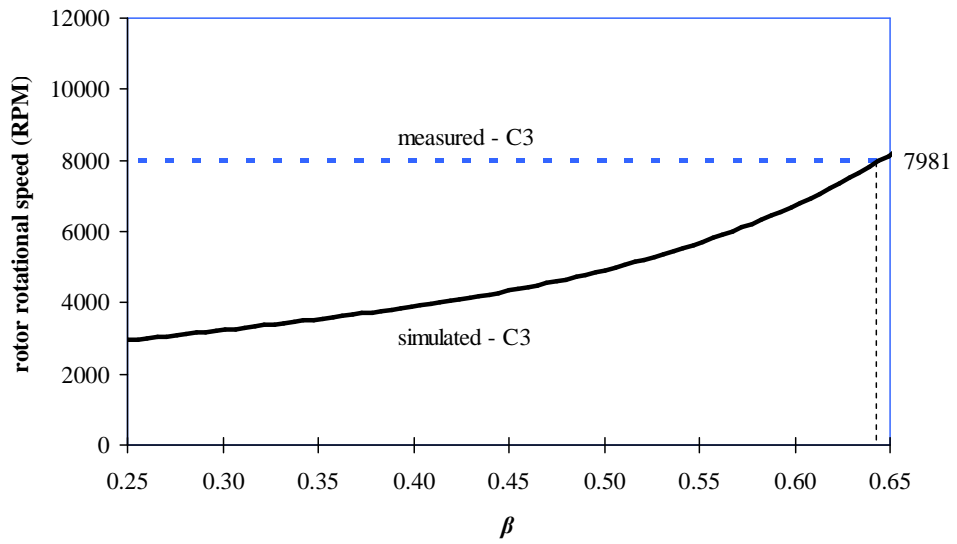


Figure 68: Variation of simulated average rotor rotational speed with β for Phase 1 case C3.

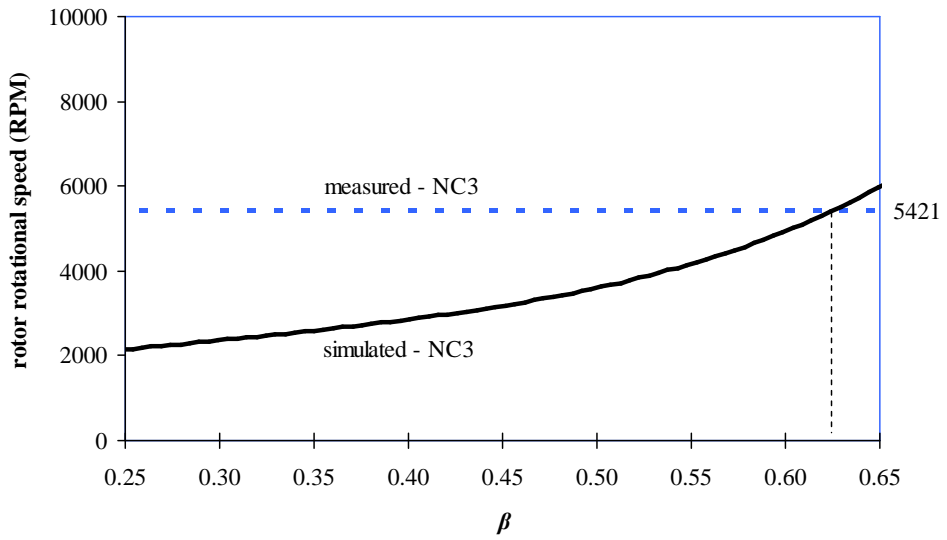


Figure 69: Variation of simulated average rotor rotational speed with β for Phase 1 case NC3.

The modeling methodology used in Phase 1 is replicated for Phase 2. Table 12 lists the Phase 2 bearing rotational speed model simulation input parameters. The radial clearances and bearing loads are changed appropriately for each of these four test cases.

Table 12: Model parameters for Phase 2 test cases NC4, NC5, C4, and C5.

Bearing Parameter	NC4	NC5	C4	C5
C_o (m)	3.5×10^{-6}	5.0×10^{-6}	7.7×10^{-6}	9.2×10^{-6}
μ	0.3	0.3	0.3	0.3
<i># of impacts</i>	150	150	150	150
r (m)	200×10^{-6}	200×10^{-6}	200×10^{-6}	200×10^{-6}
R (m)	850×10^{-6}	850×10^{-6}	850×10^{-6}	850×10^{-6}
m (kg)	7.0×10^{-7}	7.0×10^{-7}	7.0×10^{-7}	7.0×10^{-7}
F_x (N)	1142×10^{-6}	1159×10^{-6}	1156×10^{-6}	1156×10^{-6}
e_{xin} (m)	0	0	0	0
e_{yin} (m)	0	0	0	0
v_{xin} (m/s)	0	0	0	0
v_{yin} (m/s)	0	0	0	0
ω_{in} (rad/s)	0	0	0	0

Table 13 contains the Phase 2 simulated rotor rotational speeds after 150 impacts which is when steady-state speeds were reached.

Table 13: Simulated average rotor rotational speeds (RPM) for Phase 2 cases NC4, NC5, C4, and C5.

Bearing \ β	0.25	0.30	0.35	0.40	0.45	0.50	0.55	0.60	0.65
C5	5900	6430	7061	7872	9022	10555	12035	13457	15940
C4	5398	5883	6460	7202	8254	9656	11011	12311	14583
NC5	4355	4746	5212	5811	6660	7791	8884	9934	11767
NC4	3617	3942	4329	4826	5531	6471	7378	8250	9772

Figure 70 and Figure 71 illustrate the simulated average rotor rotational speeds for Phase 2 conformal and non-conformal cases, respectively. The observations that were evidenced in Phase 1 are repeated here. In addition, for a fixed load and β , it is observed that the rotational speed dependency on the clearance parameter C_0 holds even when the configuration (non-conformal or conformal) is fixed.

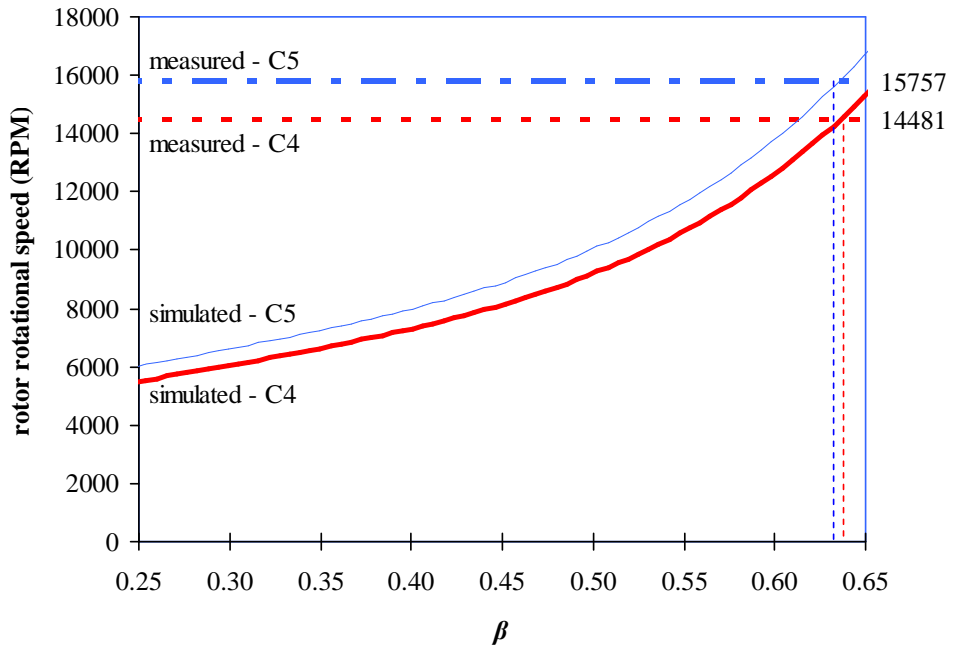


Figure 70: Variation of simulated average rotor rotational speed with β for Phase 2 cases C4 and C5.

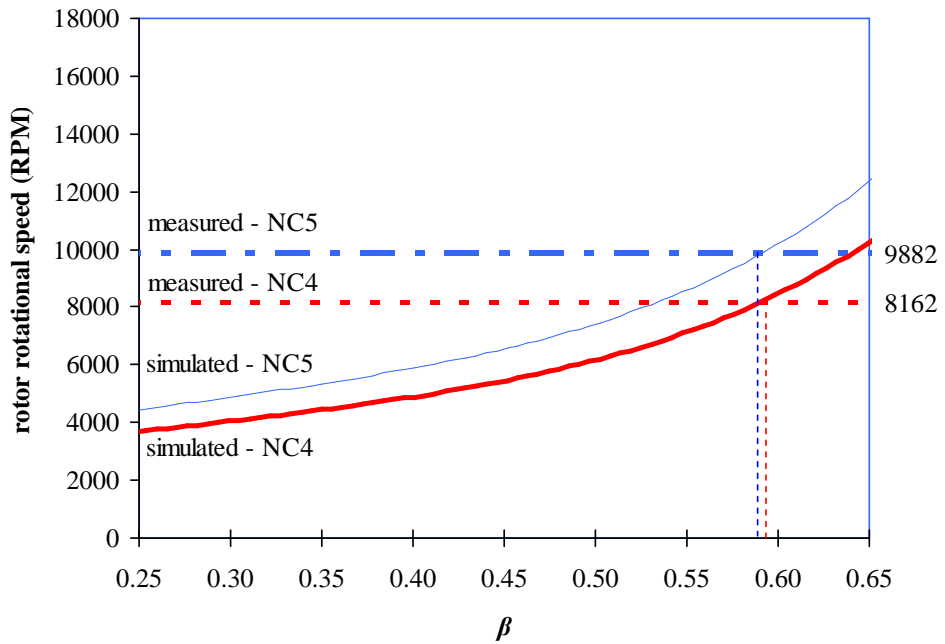


Figure 71: Variation of simulated average rotor rotational speed with β for Phase 2 cases NC4 and NC5.

The β value was adjusted until the steady-state rotor angular velocity obtained from the simulation was equal to the corresponding measured value. Figure 72 shows the values of β obtained for each of the Phase 1 (NC3 and C3) and Phase 2 (NC4, NC5, C4, and C5) test cases. These values agree reasonably well with a β of 0.56 obtained from impact of polysilicon microstructures [51].

The β values for silicon-on-silicon surfaces determined in this dissertation are apparently the first one documented.

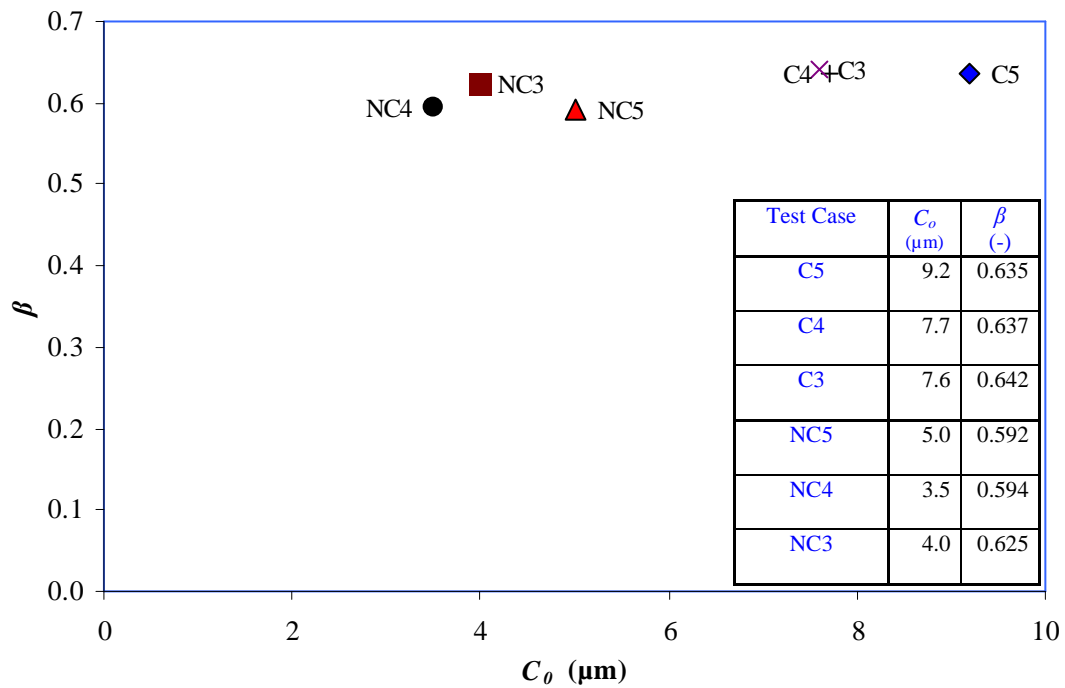


Figure 72: Plot of β vs. C_0 obtained for Phase 1 (NC3 and C3) and Phase 2 test cases (NC4, NC5, C4, and C5).

5 CONCLUSIONS

5.1 Summary

This dissertation presented an investigation of geometric effects on the wear of large aspect ratio silicon journal microbearings. The consideration of geometric conformality of rotor and hub as a critical design parameter manifested from the inherent properties of deep reactive ion etching as part of the current MEMS fabrication process employed in this dissertation. The investigation was conducted in two phases, each characterized by novel microbearing designs, fabrication processes, experimental test methodologies, and characterization techniques. The intent of Phase 1 was to focus on the effects of conformality on wear, while the intent of Phase 2 was to focus on the effects of clearance on wear. The design, fabrication, and characterization of these microbearings with conventional surface lithography techniques along with the experimental apparatus development and procedures have been detailed.

Manual assembly of rotors and hubs allowed a broader range of custom bearing clearances than would otherwise have been available from lithographic, pattern transfer, and etching capabilities of current *in situ* MEMS fabrication technologies. The stepped thrust pads developed in Phase 2 of this dissertation are apparently the first microsystems-based passive thrust bearings to be documented.

Novel *in situ* wear indicators, intended to facilitate the rapid quantitative and qualitative determination of wear, were incorporated in the Phase 2 rotor designs. The incorporation of these built-in metrology features could eliminate the need for expensive metrology hardware, software, and associated repetitive calibrations. In order to minimize their effect on wear, circular wear indicators should be small relative to the dimensions of the hub and rotor. A minimal laser spot size can be used for mask writing in order to generate such circular wear indicators.

Two particular enabling features of the novel fabrication processes, namely the sprue and float etching methods, were developed in this dissertation. The sprues, patterned using the DRIE mask, held the rotors in place during the KOH etching process. The sprues were then fully oxidized during the oxide growth step and finally dissolved away during the rotor release etch step. The float etching technique entailed floating the device wafer on top of the KOH etchant bath. The rotors were oriented upward (away from the KOH bath) during etching in order to prevent the rotor top and critical vertical bearing surfaces from being etched.

The fabrication methodology undertaken for Phase 2 fabrication offered many advantages when compared to that of Phase 1, including

- the elimination of the silicon access hole drilling procedure and thereby minimization of hub cleavage possibility
- the elimination of the hub wafer dicing process step as rotors were assembled and tested on hub wafers
- simplified logistics involving rotor tracking due to clearly distinguishable geometric design variations

- a reduction in intra-wafer rotor thickness variation as the entire wafer was submersed and agitated during etching, thereby mitigating the effects of micro-masking
- an increased device yield per wafer enabled robust performance comparisons along with increased statistical significance via increased sample sizes

The results obtained from using the first apparatus indicated that microbearing performance was substantially dependent on conformality. Microbearings in a conformal configuration, pneumatically driven to approximately 1.9 million revolutions, exhibited substantial wear. In contrast, microbearings in a non-conformal configuration, pneumatically driven using the same pressure differential, exhibited no discernable wear.

The results obtained using the second apparatus indicated that microbearing rotor rotational velocity was substantially dependent on radial clearance parameter C_o . Microbearings with larger radial clearance values, pneumatically driven to approximately 5 million revolutions, rotated faster than did those with smaller radial clearance values. This was true for bearings in non-conformal and conformal configurations.

The observed wear trends in the conformal and non-conformal bearing systems could not be attributed to an adhesion wear mechanism. Observed wear morphology was strongly suggestive of impact or surface fatigue wear. Repeatability of experimental results with similar clearance and rotor dimensions reinforced this observation.

A dynamic impact model of the bearing system based on classical impulse-momentum relations was formulated in order to assess the effect of clearance on rotor rotational speed. Coefficient of restitution values were obtained for silicon-on-silicon surfaces over the range of kinematically allowable radial clearance specifications. These values were apparently the first obtained for silicon-on-silicon surfaces, and are similar to previously published results for polysilicon microstructures.

5.2 Recommendations

The observed wear trends should not detract the use of high-aspect ratio bearings for relatively low speed applications. Satisfactory performance of the non-conformal bearing configurations was observed up to 2×10^6 cycles which should be adequate, for example, for single-use pumping applications in lab-on-chip microsystems. Surface coatings, tighter assembly clearances, tighter surface finishes, and a tighter control on the DRIE process to minimize bearing taper angles will also help improve bearing performance.

The experimental methodologies developed in this work can serve as a benchmark for tribological testing of microturbomachinery components made from a variety of different materials. The knowledge gained will help enhance bearing performance and will serve as an enabler to a host of applications including

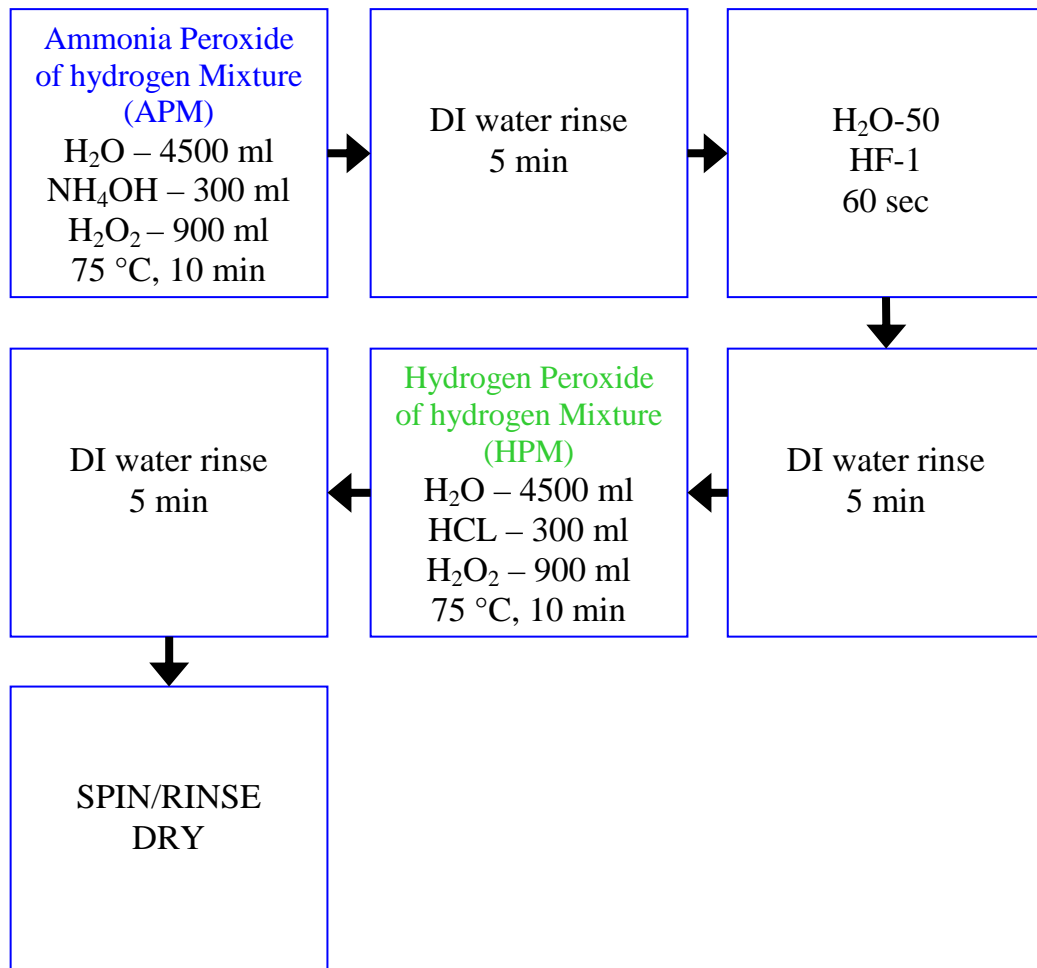
- MEMS - microengines, distributed and portable power generation, actuators (linear, angular), gears, cutters, drills, and polishers
- Bioengineering - lab-on-chip, micropumps, cardiovascular/respiratory (blood/air) circulation and experimental visualization
- Metrology - flow meters (micro/nano) and internal/external flow (boundary layer characterization)
- Materials science - coating characterization
- Mechanical/Aerospace - micro air vehicles (MAV) and satellites
- Microelectronic Engineering - heating and cooling
- Optics/Security - discriminators (high security locks) and high speed actuators (camera, strobe)

It should be noted that manual assembly of the rotor-hub system is a delicate labor intensive procedure. Given the tight clearances considered in this dissertation, a more efficient mass assembly methodology is desirable. Alternative rotor-hub axial alignment and vibratory methods merit further investigation.

APPENDICES

A FABRICATION PROCESSES

A.1 RCA Clean



A.2 BRUCE Furnace Oxidation Recipe #168

\\GMINGR\c-drive\735Host\Recipes\#01P0168.RCP

Page 1

Step	Time	Fl	F2	F3	Temp row	Gas row	Temp row	Gas row	Tctrl Mode	Abort Mask	Co eff
0	BOAT OUT	0:00:00	---	---	1	7	D	A	0	0	0
1	Start	0:00:01	---	---	2	2	D	A	0	0	0
2	PUSH IN	0:12:00	---	---	2	2	D	A	0	0	0
3	STABILIZE	0:10:00	---	---	2	2	D	A	0	0	0
4	RAMP TO 1100	0:30:00	---	---	6	1	D	A	0	0	0
5	STABILIZE	0:10:00	---	---	6	1	D	A	8	0	0
6	O2 FLOOD	0:05:00	---	---	6	4	D	A	8	0	0
7	SOAK	2:15:00	---	---	6	6	D	A	8	0	0
8	N2 PURGE	0:05:00	---	---	6	3	D	A	0	0	0
9	RAMP DOWN	0:55:00	---	---	1	2	D	A	0	0	0
10		0:00:00	---	---	0	0	0	0	0	0	0
11		0:00:00	---	---	0	0	0	0	0	0	0
12		0:00:00	---	---	0	0	0	0	0	0	0
13		0:00:00	---	---	0	0	0	0	0	0	0
14		0:00:00	---	---	0	0	0	0	0	0	0
15		0:00:00	---	---	0	0	0	0	0	0	0
16		0:00:00	---	---	0	0	0	0	0	0	0
17		0:00:00	---	---	0	0	0	0	0	0	0
18		0:00:00	---	---	0	0	0	0	0	0	0
19		0:00:00	---	---	0	0	0	0	0	0	0
20		0:00:00	---	---	0	0	0	0	0	0	0
21		0:00:00	---	---	0	0	0	0	0	0	0
22		0:00:00	---	---	0	0	0	0	0	0	0
23		0:00:00	---	---	0	0	0	0	0	0	0
24		0:00:00	---	---	0	0	0	0	0	0	0
25		0:00:00	---	---	0	0	0	0	0	0	0
26		0:00:00	---	---	0	0	0	0	0	0	0
27		0:00:00	---	---	0	0	0	0	0	0	0
28		0:00:00	---	---	0	0	0	0	0	0	0
29		0:00:00	---	---	0	0	0	0	0	0	0
30		0:00:00	---	---	0	0	0	0	0	0	0

range	O2	H2	O2	TPANIC FL	Co eff
1	5.00	0.00	0.00	0.00	0.00
2	10.00	0.00	0.00	0.00	0.00
3	15.00	0.00	0.00	0.00	0.00
4	0.00	5.00	0.00	0.00	0.00
5	0.00	10.00	0.00	0.00	0.00
6	0.00	2.00	3.60	0.00	0.00
7	0.00	0.00	0.00	0.00	0.00
8	0.00	0.00	0.00	0.00	0.00

Temperature Table

	Load	Cntr	Src	P Load	P Cntr	P Src
1	25.00	25.00	25.00	25.00	25.00	25.00
2	800.00	800.00	800.00	800.00	800.00	800.00
3	0.00	0.00	0.00	0.00	0.00	0.00
4	1100.00	1100.00	1100.00	1100.00	1100.00	1100.00
5	1100.00	1099.80	1100.00	1100.00	1099.80	1100.00
6	1100.00	1099.90	1100.00	1100.00	1099.90	1100.00
7	0.00	0.00	0.00	0.00	0.00	0.00
8	0.00	0.00	0.00	0.00	0.00	0.00

Alarm Mask/Abort Destination Table

Row	Binary	Temp	Gas	Scanner	DestStep
A	-----	-----	-----	-----	0
B	-----	-----	-----	-----	0
C	-----	-----	-----	-----	0
D	-----	-----	-----	-----	0

Alert/Alarm Multiplier Table

Row	Temp	Gas
A	0.0	0.0
B	0.0	0.0
C	0.0	0.0

Boat Speed and Distance Table

	Speed1	Dist1	Speed2	Dist2	Speed3	Dist3
Boat in Initial	15	99	0	0	0	0
Boat in Subsequent	0	0	0	0	0	0
Boat out Initial	15	4	0	0	0	0
Boat out Subsequent	0	0	0	0	0	0

Tube Access Table

Tube 12345678

Access I-----

Variable Times Table

Step	Min	Max
0	00:00:00	00:00:00
0	00:00:00	00:00:00
0	00:00:00	00:00:00

Coefficient Table

	Load				Center				Source			
	A	B	C	D	A	B	C	D	A	B	C	D
Proportional	16.00	0.00	0.00	0.00	16.00	0.00	0.00	0.00	16.00	0.00	0.00	0.00
Reset	0.45	0.00	0.00	0.00	0.45	0.00	0.00	0.00	0.45	0.00	0.00	0.00
Rate	0.10	0.00	0.00	0.00	0.10	0.00	0.00	0.00	0.10	0.00	0.00	0.00
Out Loop Rate	16.00	0.00	0.00	0.00	16.00	0.00	0.00	0.00	16.00	0.00	0.00	0.00
Latency	0.40	0.00	0.00	0.00	0.40	0.00	0.00	0.00	0.40	0.00	0.00	0.00
Calibration	5.00	0.00	0.00	0.00	-0.10	0.00	0.00	0.00	-0.50	0.00	0.00	0.00

Coefficient Table row F

Parameter	Load	Center	Source
Data store constant	0.00	0.00	0.00
Notch prop band multiplier	0.00	0.00	0.00
Spare	0.00	0.00	0.00
Spare	0.00	0.00	0.00
Setpoint update & initial target update	0.37	2.00	0.00
Counts/profile & limits for profile	0.04	0.05	10.00

Custom Temperature Alert Table

Alert Limits	Load	Center	Source
Temperature	1000.00	1000.00	1000.00
Profile	1000.00	1000.00	1000.00

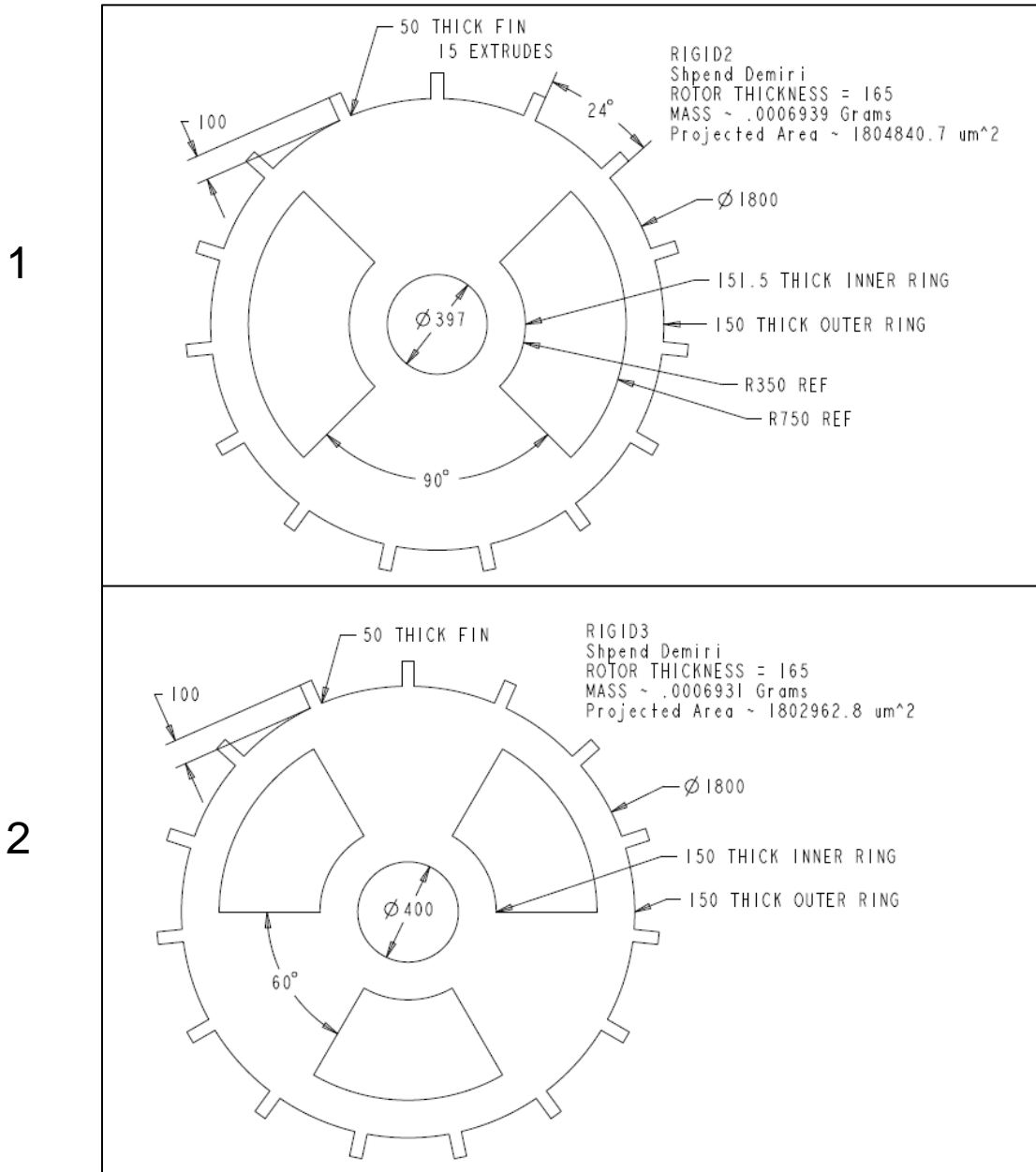
Gas Alert Limits

N2	20.00
O2	20.00
H2	20.00
O2	20.00
TRANLC FL	20.00
	0.00
	0.00

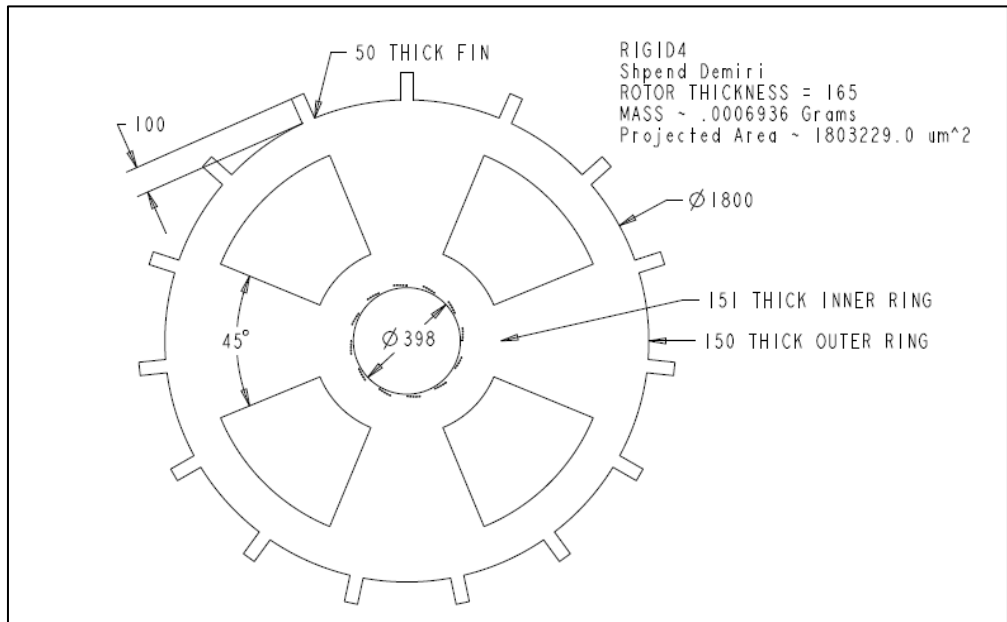
End of Recipe: < SMFL 10,000A Wet Ox>

B CAD DRAWINGS

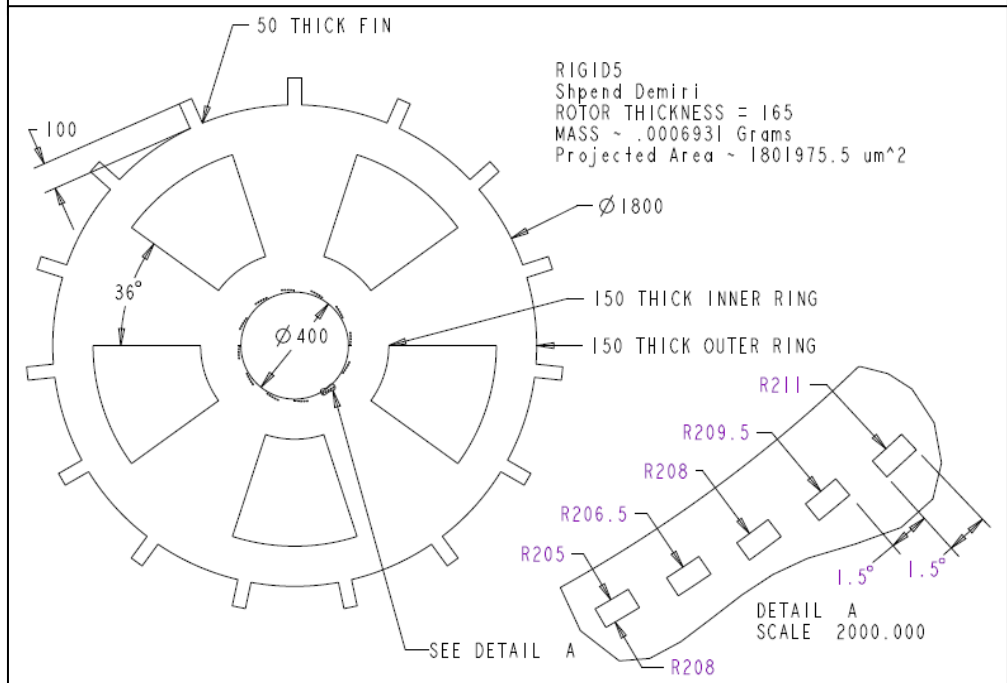
B.1 Phase 2 Rotor CAD Drawings



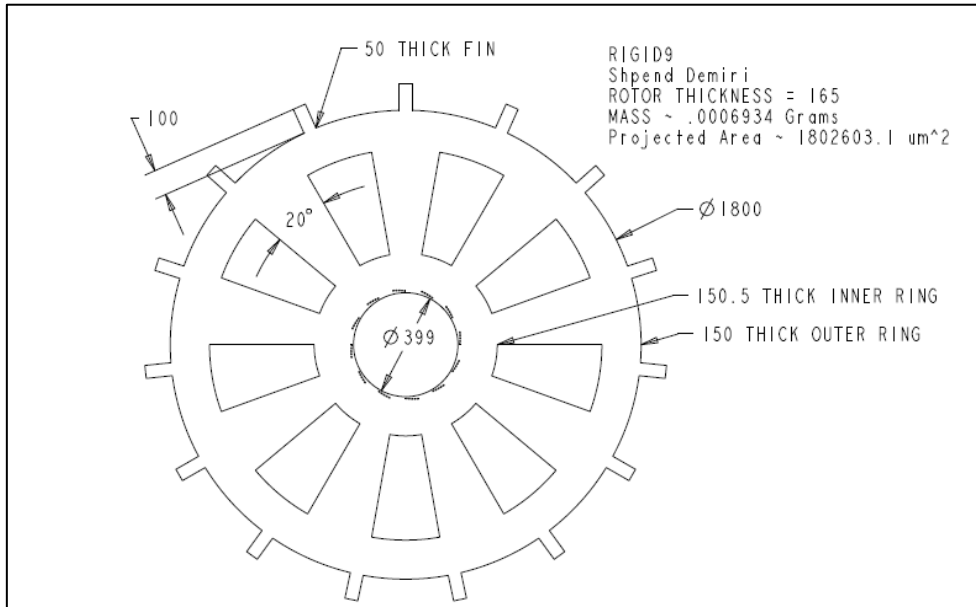
3



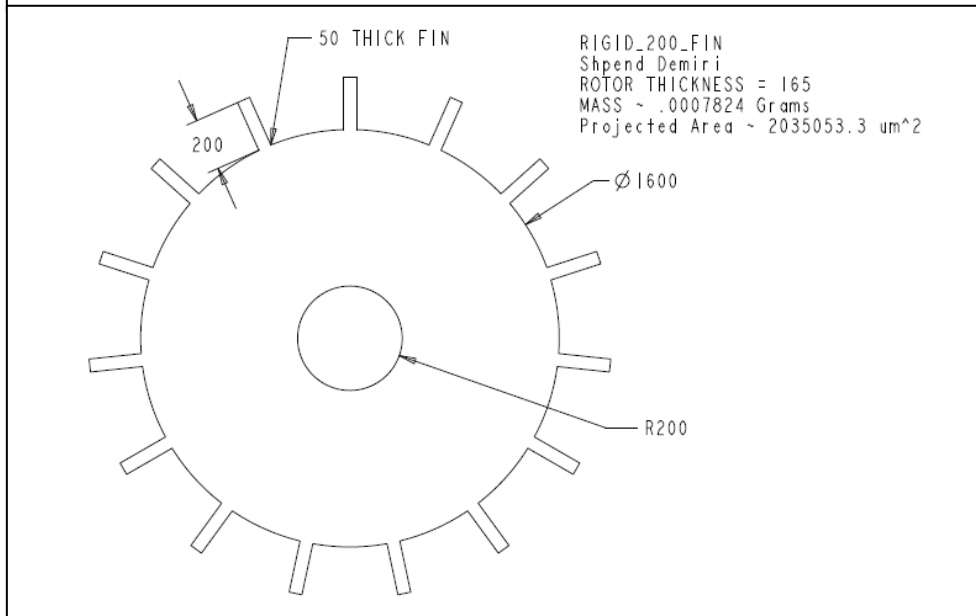
4



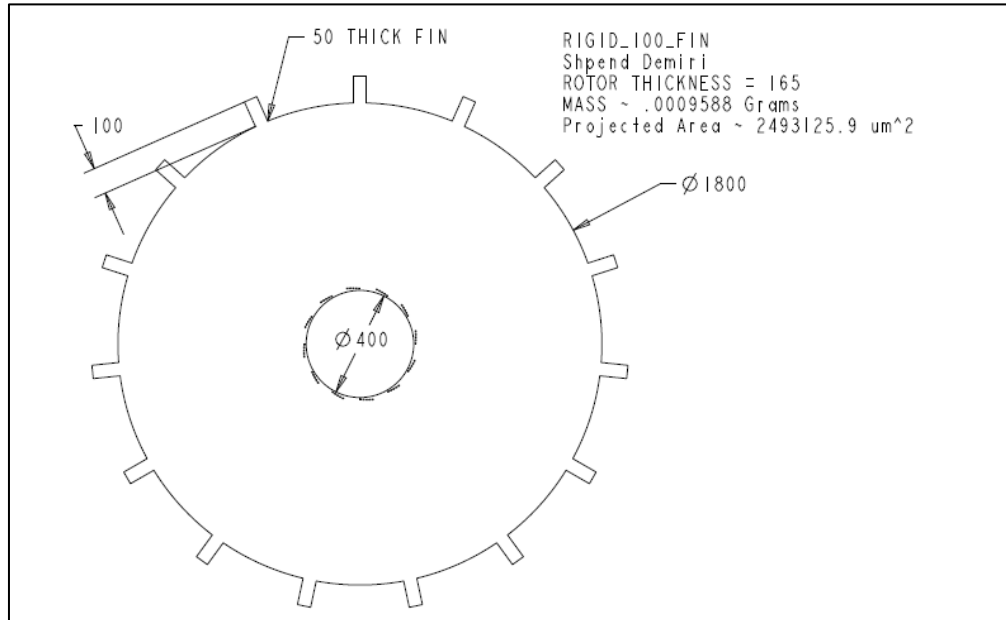
5



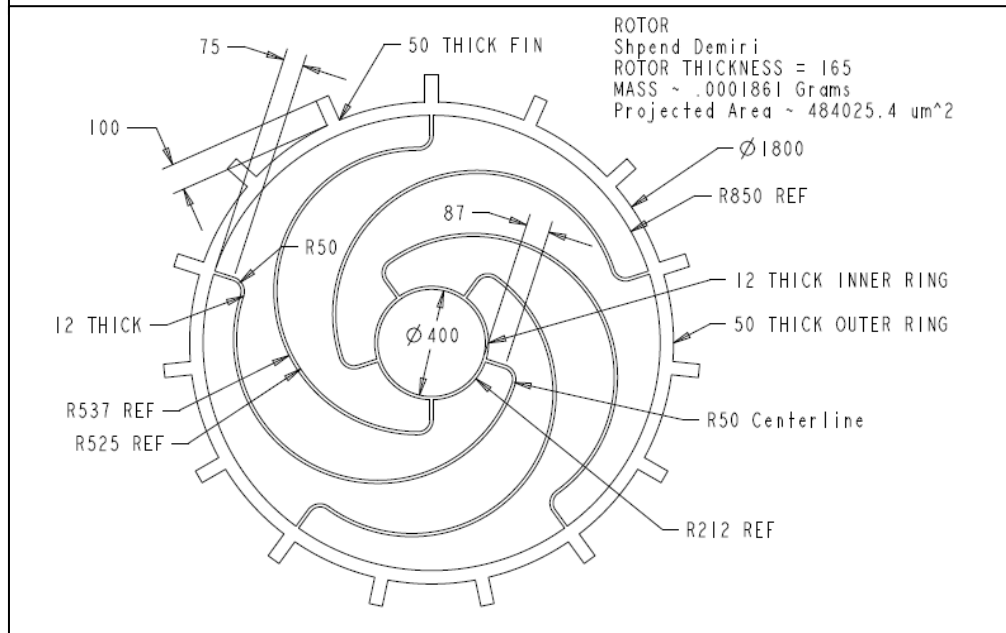
6



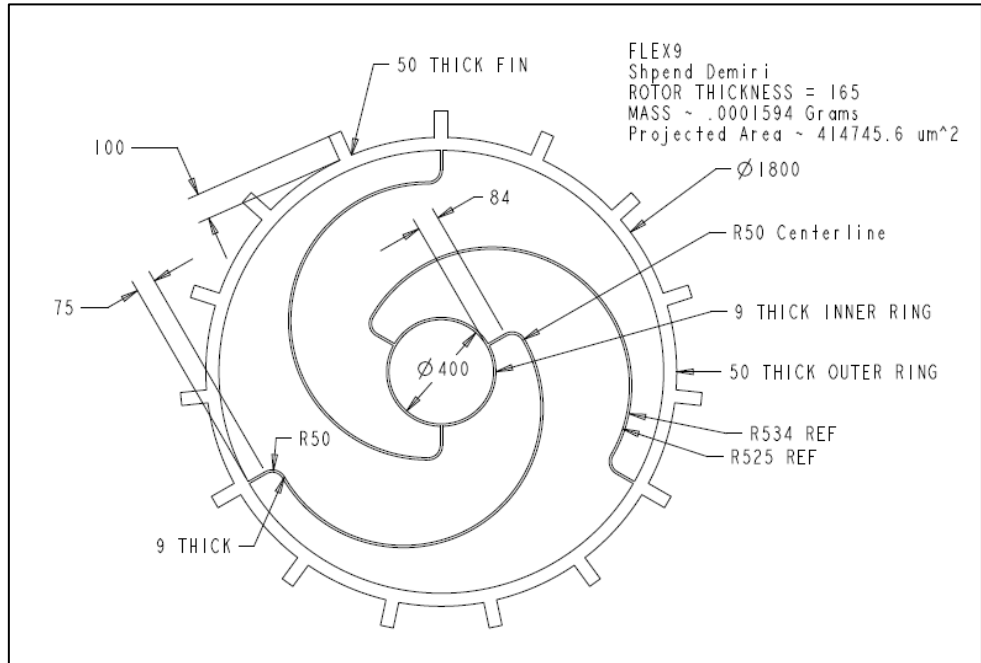
7



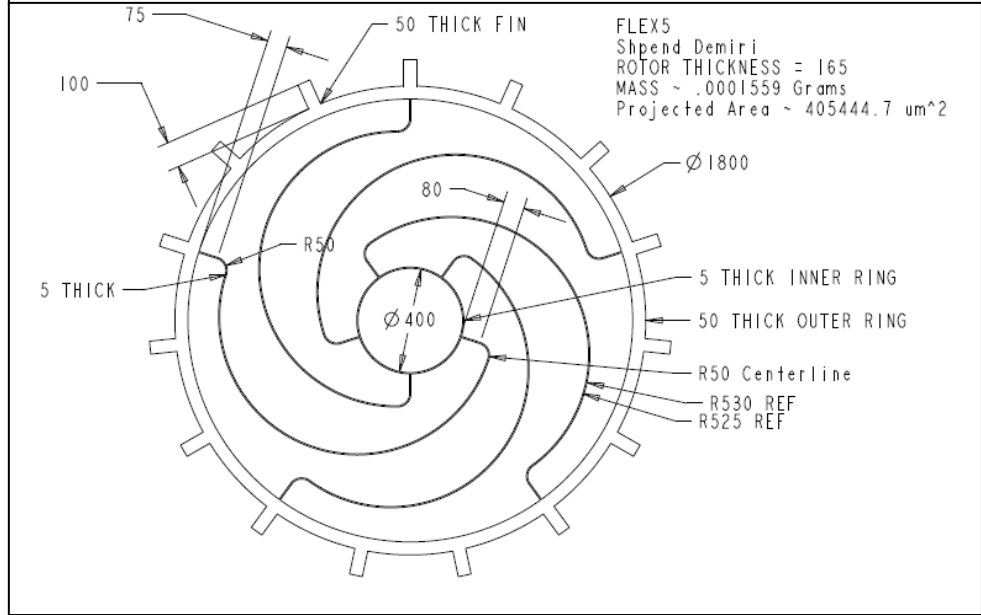
8



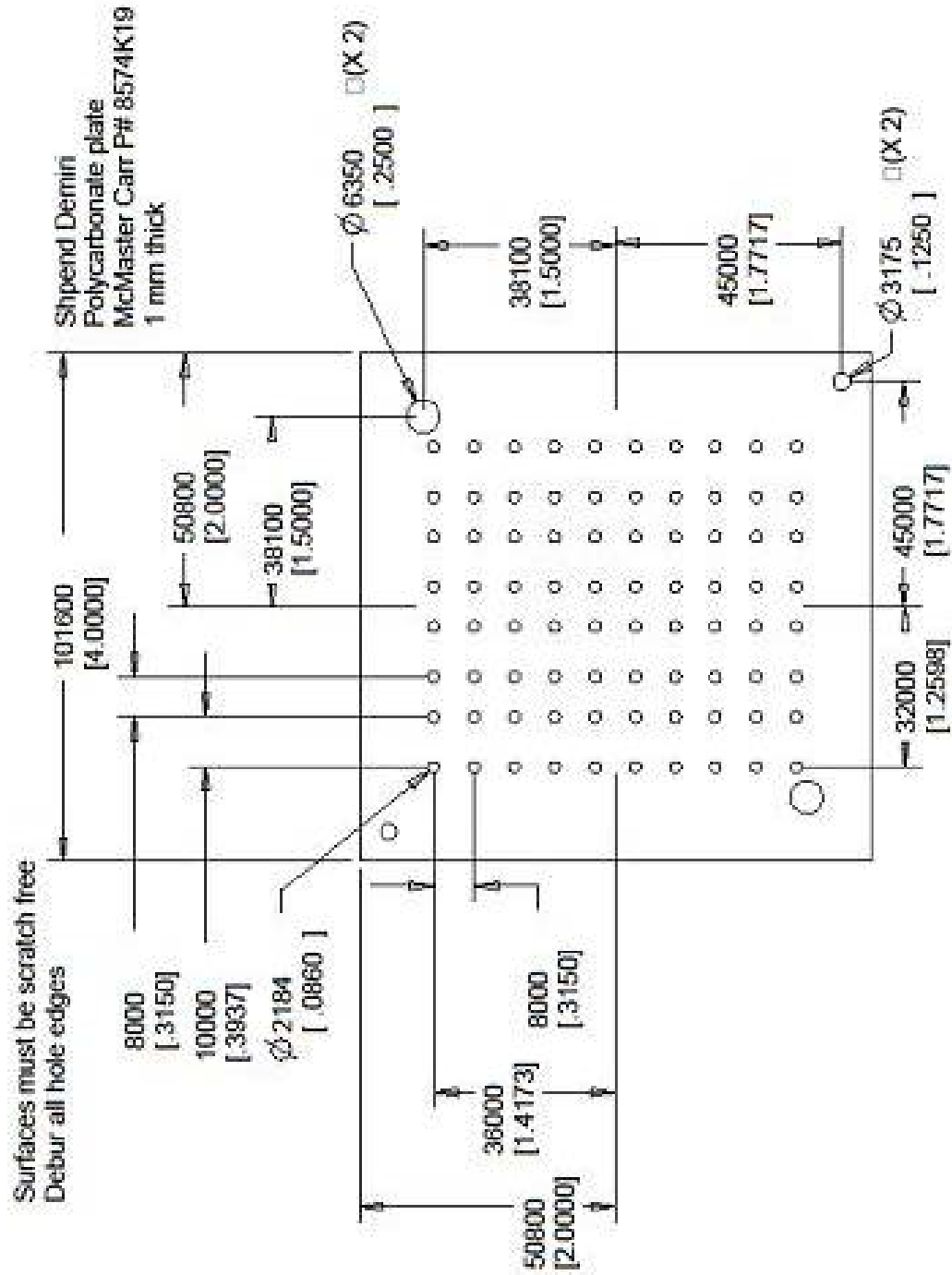
9



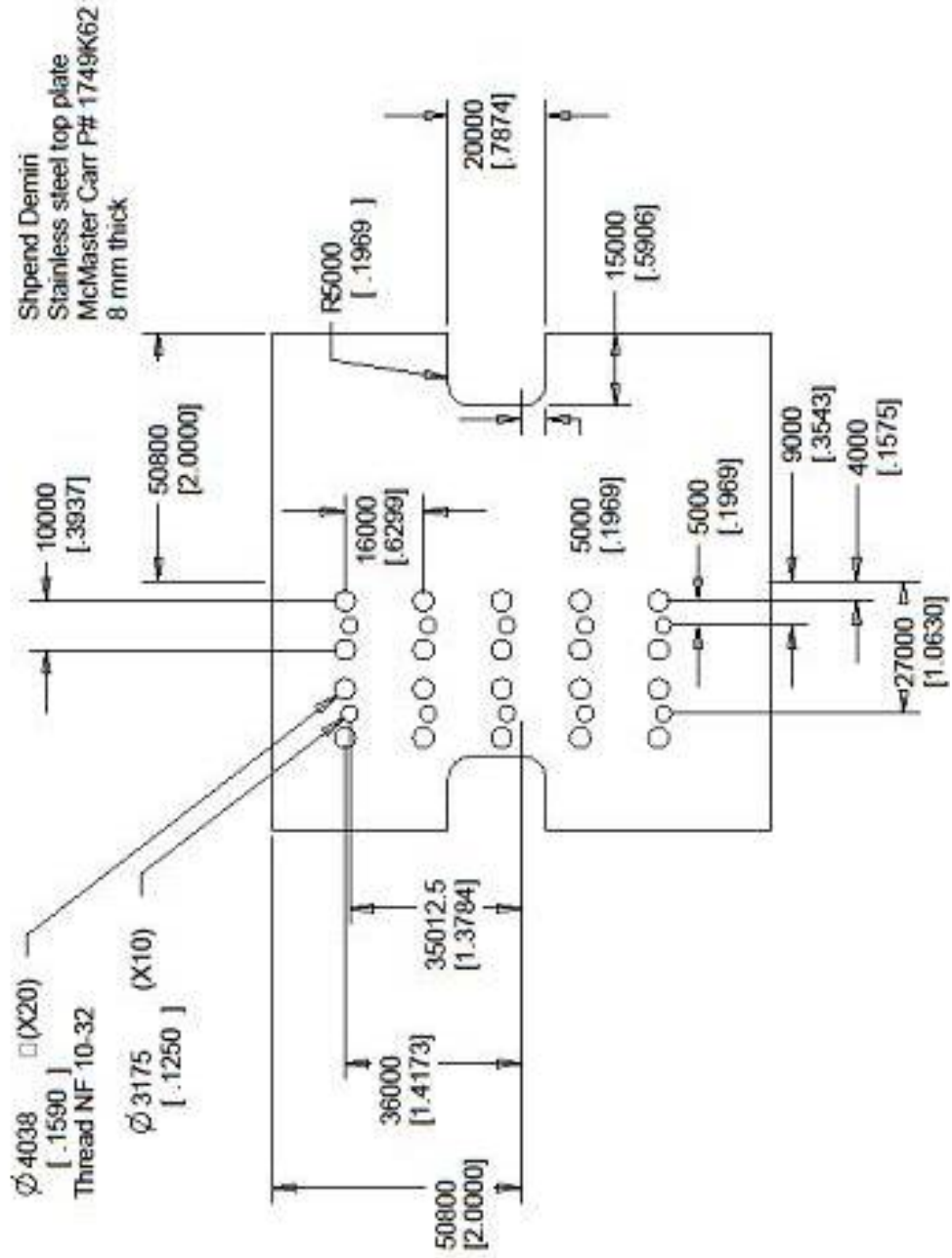
10



B.2 Phase 2 Polycarbonate Plate CAD Drawing



B.3 Phase 2 Steel Top Plate CAD Drawing



REFERENCES

1. Peterson, K. E., Silicon as a Mechanical Material, *Proc. IEEE*, Vol. 70, No. 5, (1982), pp. 420-457.
2. Feynman, R. P., There's Plenty of Room at the Bottom, *Journal of Microelectromechanical Systems*, Vol. 1, No. 1 (March 1992), pp. 60-66. (This reference is a transcript of a talk given by Richard P. Feynman on December 26, 1959, at the annual meeting of the American Physical Society at the California Institute of Technology, and was published as a chapter in the Reinhold Publishing Corporation book, *Miniaturization*.)
3. Kovacs, G. T. A., *Micromachined Transducers Sourcebook*, WCB/McGraw-hill, New York, USA, (1998).
4. Madou, M., *Fundamentals of Microfabrication*, CRC Press, Boca Raton, USA, (1997).
5. Epstein, A., Senturia, S., Anathasuresh, G., Ayon, A., Breuer, K., Chen, K.-S., Ehrich, F., Gauba, G., Ghodessi, R., Groshenry, C., Jacobson, S., Lang, J., Lin, C.-C., Mehra, A., Miranda, J. M., Nagle, S., Orr, D., Piekos, E., Schmidt, M., Shirley, G., Spearing, S., Tan, C., Tzeng, Y.-S., and Waitz, I., Power MEMs and Microengines, *International Conference on Solid-State Sensors and Actuators. Transducers 97*, Chicago, IL, (1997).
6. Nguyen, N. T., Huang, X., and Chuan, T. K., MEMS-Micropumps: A Review, *ASME J. Fluids Eng.*, Vol. 124, (2002), pp. 384-392.
7. Sniegowski, J. J., and Garcia, E. J., Microfabricated Actuators and Their Applications in Optics, *Proc. SPIE*, Vol. 2383, (1995), pp. 46-64.
8. Sniegowski, J. J., Miller, S. L., LaVigne, G. F., Rodgers, M. S., and McWhorter, P. J., Monolithic Geared-Mechanisms Driven by a Polysilicon Surface-Micromachined On-Chip Electrostatic Microengine, *Proc. Solid-State Sens. Actuators Workshop*, Hilton Head Island, SC, (1996), pp. 178-182.
9. Miller, S. L., La Vigne G., Rodgers M. S., Sneigowski J.J., Waters J. P., and McWhorter P. J., Routes To Failure in Rotating MEMS Devices Experiencing Sliding Friction, *Proc. SPIE Micromachined Devices and Components III*, Vol. 3224, (1997), pp. 24-30.
10. Epstein, A. H. *et al.*, Micro-Heat Engines, Gas Turbines, and Rocket Engines-The MIT Microengine Project, AIAA 97-1773, *28th AIAA Fluid Dynamics Conference*, Snowmass Village, CO, (1997).

-
11. Epstein, A. H., Jacobson, S. A., Protz, J., and Fréchette, L. G., Shirtbutton-Sized Gas Turbines: The Engineering Challenges of Micro High-Speed Rotating Machinery, *Proc. 8th Int. Symposium on Transport Phenomena and Dynamics of Rotating Machinery*, Honolulu, HI, (2000).
 12. Tanner, D. M. *et al.*, The Effect of Humidity on the Reliability of a Surface Micromachined Microengine, *Proc. IEEE International Reliability Physics Symposium*, (1999), pp. 189-197.
 13. Breuer, K., Ehrich, F., Fréchette, L., Jacobson, S., Lin, C.-C., Orr, D. J., Piekos, E., Savoulides, N., and Wong, C.-W., Challenges for Lubrication in High Speed MEMS, *Nanotribology*, Hsu and Ying, eds., Kluwer Academic Press, Dordrecht, The Netherlands, (2003).
 14. Trimmer, W., Microrobots and Micromechanical Systems, *Sensors and Actuators*, Vol. 19, No. 3, (1989), pp. 267-287.
 15. Isomura, K. *et al.*, Development of Micromachine Gas Turbine for Portable Power Generation, *JSME International Journal, Series B: Fluids and Thermal Engineering*, Vol. 47, No. 3, (2004), pp. 32–35.
 16. Peirs, J., Reynaerts, D., and Verplaetsen, F., Development of an Axial Microturbine for a portable gas turbine generator, *Journal of Micromech. Microeng.*, Vol. 13, (2003), pp. S1900–S195.
 17. Ghalichechian, N., Modafe, A., Beyez, M., and Ghodssi, R., Design, Fabrication, and Characterization of a Rotary Micromotor Supported on Microball Bearings, *Journal of Microelectromechanical Systems*, Vol. 17, (2008), pp. 632–642.
 18. Fan, L. S., Tai, Y. C., and Muller, R.S. Pin Joints, Gears, Springs, Cranks, and Other Novel Micromechanical Structures, *Tech. Dig. 4th Int. Conf Solid-State Sensors and Actuators*, (1987), pp. 849-852.
 19. Fan, L. S., Tai, Y. C., and Muller, R. S., IC-Processed Electrostatic Micromotors, *Tech. Dig. IEDM*, (1988), pp. 666-669.
 20. Gabriel, K. J., Trimmer, W. S. N., and Mehregany, M., Microgears and Turbines Etched From Silicon, *Tech. Dig. 4th Int. Conf Solid-State Sensors and Actuators* (1987), pp. 853-856.
 21. Tai, Y. C., and Muller, R. S., IC-Processed Electrostatic Synchronous Micromotor, *Sensors and Actuators*, Vol. 20, (1989), pp. 49-55.

-
22. Mehregany, M., and Senturia, S. D., Micromotor Fabrication, *IEEE Transactions on Electron Devices*, Vol. 39, No. 9, (1992), pp. 2060-2069.
 23. Tsai, C.-L., and Henning, A. K., Surface Micromachined Turbines, *International Conference on Solid-State Sensors and Actuators*, Chicago (1997), pp. 829-832.
 24. Bustillo, J. M., Howe, R. T., and Muller, R. S., Surface Micromachining for Micromechanical Systems, *Proc. IEEE*, Vol. 86, No. 8, (1998), pp. 1552-1574.
 25. Tanner, D. M. *et al.*, The Effect of Frequency on the Lifetime of a Surface Micromachined Microengine Driving a Load, *Proc. IEEE International Reliability Physics Symposium*, (1998), pp. 26–35.
 26. Williams, J. A., Le, H. R., Tribology and MEMS, *Journal of Physics D: Applied Physics*, No. 39, (2006), pp. 201-214.
 27. Beerswinger, U., *et al.* Wear at Microscopic Scales and Light Loads for MEMS Applications, *Wear* 181-183, (1995), pp. 426-435.
 28. Beerswinger, U., Reune, R. L., and Yang, S. J., Frictional Study of Micromotor Bearings, *Sensors and Actuators A*, Vol. 63, (1997), pp. 229-241.
 29. French, P. J., and Sarro P. M., Surface Versus Bulk Micromachining: The Contest for Suitable Applications, *J. Micromech. Microeng.* Vol. 8, (1998), pp. 45-53.
 30. Mehra, A., Ayon, A. A., Waitz, I. A., and Schmidt, M. A., Microfabrication of High Temperature Silicon Devices Using Wafer Bonding and Deep Reactive Ion Etching, *Journal of Microelectromechanical Systems*, Vol. 8, (1999), pp. 152–160.
 31. Kim, D., Lee, S., Bryant, M. D., and Ling, F. F., Hydrodynamic Performance of Gas Microbearings, *Journal of Tribology*, Vol. 126, (2004), pp. 711-718.
 32. Kim, D., Cao, D., Bryant, M. D., Meng, M., and Ling, F. F., Tribological Study of Microbearings for MEMS Applications, *Journal of Tribology*, Vol. 127, (2005) 537-547.
 33. Dimofte, F., Wave Journal Bearing with Compressible Lubricant- Part 1: The Wave Bearing Concept and a Comparison to the Plain Circular Bearing, *Tribology Transactions*, Vol. 38 (1995), pp. 153-160.
 34. Hara, M., *et al.*, Rotational Infrared Polarization Modulator using a MEMS-based Air Turbine With Different Types of Journal Bearing, *Journal of Micromech. Microeng.* Vol. 13 (2003), pp. 223-228.

-
35. Piekos, E. S., and Breuer, K. S., Pseudospectral Orbit Simulation of Nonideal Gas-Lubricated Journal Bearings for Microfabricated Turbomachines, *Journal of Tribology*, Vol. 121, No. 3 (1999), pp. 604–609.
 36. Heshmat C. A., and Heshmat, H., An Analysis of Gas-Lubricated, Multi-leaf Foil Journal Bearings With Backing Springs, *Journal of Tribology*, Vol. 117, (1995), pp. 437-443.
 37. Boedo, S., and Booker, J. F., Modal and Nodal EHD Analysis for Gas Journal Bearings, *Journal of Tribology*, Vol. 127, No. 2, (2005), pp. 60-66.
 38. Wilson, D. S., The Effect of Geometry Variations on Hydrodynamic Bearing Performance, *ASLE Trans.*, Vol. 9, (1966) pp. 411–419.
 39. Piekos, E. S., and Breuer, K. S., Manufacturing Effects in Microfabricated Gas Bearings: Axially Varying Clearance, *Journal of Tribology*, Vol. 124, (2002), pp. 815–821.
 40. Brown, D. W., Design and Fabrication of a Micro-bearing Assembly to study Rotor Friction, *21st Annual Microelectronic Engineering Conference*, Rochester, New York, (2003), pp 111-115.
 41. Boedo, S., and Grande, W. J., Structurally Compliant Microbearing Sleeve Arrangements and Methods Thereof, Provisional Patent 60\621521 Filed Oct. 22, 2004, Full Patent Application Filed Aug. 9, (2005), Published July 13, (2006), Publication # US2006\0153480.
 42. Laermer, F., and Schilp, A., German Pat., DE 4 241 045 granted on 26 May 1994 (US Pat. 5 501 893 granted on 26 March 1996).
 43. Menz, W., Mohr, J., and Paul, O., *Microsystem Technology*, Wiley-VCH, Weinheim, Federal Republic of Germany, (2001), pp. 290.
 44. Lee, C. H., Jiang K. C., Jin P., and Prewett, P.D., Design and Fabrication of a Micro Wankel Engine Using MEMS Technology, *Microelectronic Engineering*, 73-74, (2004), pp. 529-534.
 45. Archibald, F. R., A Simple Hydrodynamic Thrust Bearing, *Trans. Am. Soc. Mech. Engrs.*, Vol. 72, (1950), pp. 394-400.
 46. Tanner, D. M. *et al.*, Linkage Design Effect on the Reliability of Surface Micromachined Microengines Driving a Load, *SPIE*, Vol. 3512, (1998), pp. 215-226.

-
47. Demiri, S., Boedo, S., and Grande W. J., Conformality Effects on the Wear of Low-Speed Large Aspect Ratio Silicon Journal Microbearings, *Wear*, Vol. 268, (2010), pp. 361-372.
 48. Collins, J.A., *Failure of Materials in Mechanical Design*, Wiley, New York, (1981).
 49. Rabinowicz, E., *Friction and Wear of Materials*, Wiley, New York, (1995).
 50. Zapomel, J., Fox, C. H. J., and Malenovsky, E., Numerical Investigation of a Rotor System With Disc-Housing Impact, *Journal of Sound and Vibration*, Vol. 243, No. 2, (2001), pp. 215-240.
 51. Lee, A. P., and Pisano, A. P., Repetitive Impact Testing of Micromechanical Structures, *Sensors and Actuators A*, Vol. 39, pp. 73-83.